Studies on Morphology, Structure and Optical Response of Ion Beam Sputter Deposited Single and Bilayer Thin Films Based on Silver and Gold

Thesis submitted for the degree of

DOCTOR OF PHILOSOPHY

In

PHYSICS

By

Rajeeb Brahma

School of Physics
University of Hyderabad,
Hyderabad-500 046,
India

May 2011

DEDICATED TO MY FAMILY AND TEACHER

Declaration

I hereby declare that the matter embodied in this thesis entitled *"Studies on Morphology, Structure and Optical Response of Ion Beam Sputter Deposited Single and Bilayer Thin Films Based on Silver and Gold*", submitted to **University of Hyderabad** for the award of **Doctor of Philosophy** in **Physics** is a record of original work carried out by me under the supervision of ***Dr. M. Ghanashyam Krishna***, School of Physics, University of Hyderabad, Hyderabad. This work has not been submitted partially or fully for any degree or diploma in any other University.

Date: *Rajeeb Brahma*

Place : Hyderabad

CERTIFICATE

This is to certify that the research work presented in this thesis entitled ***"Studies on Morphology, Structure and Optical Response of Ion Beam Sputter Deposited Single and Bilayer Thin Films Based on Silver and Gold"***, for the award of **DOCTOR OF PHILOSOPHY** is original work carried out by **Mr. Rajeeb Brahma**, under my supervision at School of Physics, University of Hyderabad, Hyderabad. This thesis work has not been submitted to this or any other university partially or fully for the award of any degree or diploma.

Date:
Place: Hyderabad

Dr. M. Ghanashyam Krishna
(Supervisor)

Dean
School of Physics

Acknowledgements

It is my pleasure to write this part of the thesis and express my gratitude to all those who have helped me in a long run. Many people have directly or indirectly contributed to the successfully completion of this thesis and I thank all of them.

First of all, I would like to express my deepest gratitude and admiration to my supervisor, Dr. M. Ghanashyam Krishna for his guidance and support throughout my research. I am deeply indebted to him for his excellent guidance, patience and his encouragement. The way he has guided me has improved my ability of understanding the concepts of the problems. Without his valuable discussions and objective criticism I would not have been able to complete this task. The facilities, freedom he has given me to work is ultimate and unlimited and I hope that it was utilized in a proper way.

I sincerely thank my Doctoral committee member Prof. C. S. Sunandana for his valuable suggestions, discussions, encouragement and support throughout my Ph. D.

I greatly appreciate and thank Dr. K. C. James Raju for his constant support and the facilities he has offered during my research work.

My sincere thanks to Prof. Anil K Bhatnagar for his encouragement and suggestions.

I would like to extent my sincere thanks to Dr. P. Anantha lakhsmi and Dr. Suneel Singh for the simulation work and encouragement.

I specially thank the Dean, School of Physics Prof. C. Bansal for the support and providing me ion source power supply. Without his help my work would have been taken much longer time.

I thank former Deans Prof. Vipin Srivastava, Prof. S. N. Kaul and Prof. V. S. S. Sastry for providing me facilities for the successful completion of my work. I also thank all the faculty members who have helped me throughout my stay here at University of Hyderabad. Also I gratefully remember all my other teachers who taught me in schools as well as the faculty members of Pondicherry Central University.

My sincere thanks to the staff of the CIL, Mr. C. S. Murthy, Mr. Suresh, Dr. S. Manjunath, Mr. Nageshwar Rao, Mr. Sudhakar for the technical support they provided. I thank Ravishankar and Durgaprasad for XRD and TEM characterization.

I am thankful to Mr. Abraham, Office Assistant, School of Physics for his timely help and guidance in official works. Mr. Anantha Rao, Mrs. Sarama, Mr. Purnachandra Rao of School of Physics are also acknowledged for their help.

I would like to acknowledge UGC for providing me fellowship and DST-ITPAR, UGC-CAS, DST funded Center for Nanotechnology for the facilities I have used during my Ph. D.

It is my enormous pleasure to thank my labmates right from I have joint to the lab. I thank Dr. Mahendra kumar, Dr. Madhurima, Dr. Pamu, Dr. Venkat, Dr. Prashant, Dr. Kiran, Dr. Sudheendran, Lakhsminarayan, Dr. Srinivas, Dr. Sachin, Dr. Ahmed, Dr. Vachhani, Dr. Ramesh, Polshetty, Vasu, Lakshun, Rambabu, Ramakanth, Ramaobulesu, Anil, Bashaiah, Umar, Sandeep, Arathi for helping me in various ways both academically and personally. It is really wonderful working with you all.

I would like to thank my classmates, batch mates and colleagues, Dr. Gnanavel, Dr. Bari, Dr. Saipreeti, Dr. Venkatram, Dr. Sivaji, Dr. Juby, Ravi Kumar, Sandhya, Rejeswari, Sudha, Shinto for their encouragement and support and also I thank research scholar colleagues of School of Physics for their support. I thank all my M. Sc. classmates of Pondicherry Central University for being with me all the time.

It is my pleasure to thank Dr. Ajith, Dr. Bharatimohan, Dr. Damudharan, Dr. Manimaran, Dr. Satish, Dr. Sudheendran, Dr. Joji, Dr. Venkat for helping me in every way.

I would like to thank RK, Chaya, Alezo, Nometo, Asim, Thuire, Hongre, Rangku Sudharshan, Prabhuda, Daniel, Nichet, Renbe, Awor, Ching, Asho, my best friends (Lily and Vitso), my cousin Minaxi, Deepali, Devo, who made my stay at UoH memorable for life. And also it is my pleasure to thank all the members of my football team DSP, Uncle Kill Me Quick, Kairali and Misfits for providing sportive living atmosphere during my stay at UoH. I thank all of them too whom I missed out to mention here.

I would like to thank our Bodo students group of UoH for their encouragement and moral support.

My sincere THANKS to my parents and brother for the support and for their patience.

CONTENTS

Synopsis of the thesis

The development of non-lithographic techniques for the growth of ordered and patterned nanostructures has been the subject of much interest in the recent past. Non-lithographic techniques such as vapour-liquid-solid technique, template assisted growth, laser and electric field induced nanostructuring have emerged as viable techniques for many applications. On the other hand, self organize/ordered nanostructures have been realized in recent years by a variety of chemical routes. One of the major applications of the nanostructures, self ordered or those produced by non-lithographic techniques, is in the area of tunable surface plasmon resonance (SPR) based applications. The applications of SPR devices include sensors, interconnects and waveguides and require tunable plasmon resonances to expand the wavelength regime of their applicability. Tunability is typically achieved by varying the shape, size and spacing of the nanocomponents comprising the metal nanostructures. There is, however, very little work on exploring the possibility of growing self ordered structures using industrially compatible physical vapour deposition techniques such as evaporation and sputtering and their variants. Some efforts have been made in this direction using ion beam sputtering. Much of this work relates to the formation of ripple like structures in either already deposited films or bulk surfaces. Nanostructures, to be functional, have to be grown in the form of nanoparticle arrays or nanowires and there are very few PVD techniques that have been applied successfully to realize these nano-forms. Ion beam sputter deposition (IBSD), using Ar ions of energy $\geq$ 500 eV, is a technique that has been used for many years to deposit high quality metal and metal oxide thin films. However, IBSD at energies < 500 eV has not been investigated. It is known that island like structures form in the early stages of thin film growth. The shape and size of these structures are then dependent on deposition parameters such as rate of deposition, substrate temperature and the energy of impact of condensing vapour atoms. Therefore, if the growth of films can be controlled at the early stages, then it should be possible to realize discontinuous thin films with a variety of nanostructures. This, in essence, forms the basis of the current thesis.

The main objective of the current work is to study the microstructure, crystal structure and optical response of IBSD discontinuous and nanostructured metallic thin films on different substrates. The material systems studied are (1) single layers of Ag and Au (2) metal-metal bilayers of Ag/Au, Au/Ag and In/Ag and (3) metal-dielectric bilayers consisting of Ag or

Au on SiO_2, TiO_2 or ZrO_2 surfaces. The motivation in all these cases is to understand the effect of morphology on the optical response of nanostructured metal films in the UV-Vis-NIR wavelength region from 190 to 2500 nm. Another theme is to demonstrate the versatility of low energy IBSD as technique for the realization of a variety of nanostructures in thin film form.

The thesis is presented in the following manner: Introduction in chapter I; Experimental techniques and characterization are presented in chapter II; Results and discussion on morphology and structure of metal thin films deposited by IBSD are presented in chapter III. Investigations on optical response of single layer (Ag and Au) metal thin films are presented in chapter IV. In chapter V, studies on metal/metal bilayer thin films and metal/dielectric bilayer thin films are presented. Chapter VI consists of summary of the thesis and the future prospects.

Chapter I: Introduction

In this chapter, the state of art in deposition and optical properties of Ag and Au films is reviewed. From the literature review it is concluded that there is very limited work on ion beam sputter deposition of Ag and Au films. As a consequence there is very little information on the optical behaviour of these films. There is also, no work on the use of ion beam sputter deposition for controlled nanostructuring of thin films. The above mentioned points, therefore, form the main objectives of the present thesis.

Chapter II: Experimental and Characterization techniques

In this chapter, different fabrication and characterization techniques used in the present study are described. Ion beam sputter deposition technique was used to deposit the Ag and Au thin films. Quartz, borosilicate glass and carbon coated Cu grids were used as substrates to deposit the films. Ag and Au thin films were also grown on sol-gel deposited TiO_2 and ZrO_2 thin film surfaces to understand the effect of dielectric environment on the optical behaviour. The details of the experimental conditions are presented here. Different characterization techniques such as thickness measurement by surface profilometer, structure determination and crystallite size estimation by X-ray diffraction, optical properties by UV-Vis-NIR spectrophotometry, grain size analysis, surface roughness, and surface topography by Atomic Force Microscopy (AFM), microstructures by Scanning

Electron Microscope (SEM) and structure analysis by Transmission Electron Microscope (TEM) are described.

Chapter III: Morphology and structure of Ion Beam sputter deposited metal thin films

This chapter presents the study of microstructure and structure of single layer Ag and Au thin films. The Ag and Au films were ion beam sputter deposited onto the dielectric layers. Ag (99.99% purity) and Au (99.9% purity) targets were sputtered using a Kaufman type ion source (DC25 of Oxford Applied Research, UK) with Argon ions of energy in the range of 150 to 450 eV and beam currents of 4-6 mA. The target substrate distance was about 14 cm. The combination of low energy, low flux and large substrate distances resulted in extremely good control over the microstructural evolution of the Ag and Au films. Two types of interfaces were investigated in this study. The first set of film-substrate interfaces consisted of Ag and Au films grown on borosilicate glass and carbon coated Cu grids used as substrates. A rich variety of nanostructures including self organized arrays of nanoparticles, nanoclusters and nanoneedles have been achieved. The role of the film-substrate interface is discussed within the framework of existing theories of thin film nucleation and growth. Interfacial nanostructuring of thin films is demonstrated to be a viable technique to realize a variety of nanostructures. The coalescence behaviour in discontinuous silver and gold thin films deposited on to carbon coated Cu grids and borosilicate glass substrate is also investigated. Discontinuous Ag and Au films were deposited for durations of 5-15 min and substrate temperatures from ambient to 300^{o}C. Abnormal coalescence behaviour is observed on carbon coated Cu grids. This is manifested as decrease in the island sizes both as a function of increasing deposition time (or thickness of the films) and substrate temperature from ambient to 300^{o}C. The observed behaviour is abnormal on two counts; decrease in particle diameters with increase in deposition time and decrease in particle size with increase in temperature. The abnormal nature of the behaviour is established by depositing Ag and Au films under the exact same conditions on to borosilicate glass substrates. In this case the expected coarsening of particles with increase in deposition time and temperature is observed. The abnormal behaviour is transient and explained using models of thin film growth on rough substrates. It is proposed that growth of metal films on rough substrates is a novel method to achieve a variety of nanostructures such as nanoparticle arrays.

Chapter IV: Optical response of single layer metal thin films

This chapter presents the optical response of single layer Ag and Au thin films. The possibility of tuning Surface Plasmon Resonance (SPR) by controlling the particle size and shape by the deposition process is investigated. Ag and Au films were deposited onto Borosilicate Glass (BSG) substrates by varying the beam energy from 150 eV to 600 eV, keeping other parameters constant at a pressure of 4×10^{-4} Torr and room temperature. It is observed that the absorption peak attributable to the SPR from Ag shifts towards the longer wavelength depending on the particle shape and size. The SPR shifted from 432 nm to 600 nm with the increase in particle size. The SPR was observed at a wavelength of 432 nm for 35 nm particle size and at 600 nm for approximately 100 nm particle size Ag film. Significantly, the particles were in spherical shape for most of the films and also rates of deposition as low as 0.01 nm/s are achieved at an Ar ion energy of 150 eV. This leads to the formation of a random array of nearly spherical Ag particles with a mean size of ~100 nm, separated by distances of similar order of magnitude. The particles organize themselves into arrays over lengths of at least 10 μm. As the thickness is increased from 3 to 18 nm there is a transition in morphology from an array to linear chains and finally a dense continuous film. It is observed that as the thickness of the films increase, the main plasmon peaks can be tuned from 380 to 680 nm. The spheroidal shape of the particles induces additional peaks (localized surface plasmons) centered around 430 ±10 nm. Similar behaviour of optical response is observed in the case of Au thin films. The plasmon resonance shifts towards red with the increase of thickness of the film. However, optical behaviour is different in the case of deposition at different temperature. As in the case of the Ag films, there is a blue shift in the plasmon resonance with increase in substrate temperature. At room temperature the plasmon resonance is observed at 628 nm, which shifts to 610 nm at 200^{o}C and finally to 600 nm at 300^{o}C. The observed blue-shift is a consequence of the decreasing particle size with increase in substrate temperature, as discussed later. The optical behavior of the films deposited at a fixed substrate temperature of 300^{o}C but varying durations of deposition is very different. It is observed that, for deposition duration of 5 min, resonance occurs at 534 nm. When the deposition time is increased to 10 min., resonance is red shifted to 554 nm. As the deposition time is increased to 15 min., there is a further red shift of resonance to 566 nm. Detailed simulations have been carried out based on Maxwell Garnett theory to distinguish the effects of shape and size on plasmon resonances. It is demonstrated that shape rather than the size of the particles has a stronger

influence on the shift in plasmon resonances. This study shows the ability to tune the surface plasmon resonance by controlling the particle size and shape during deposition by IBS technique with its wide range of control parameters.

Chapter V: Optical response of metal-metal and metal-dielectric bilayer thin films

In this chapter the morphology and optical response of metal-metal and metal-dielectric bilayer is discussed. The systems studied are (1) Ag/Au (Ag as top layer), (2) Au/Ag (Au as top layer), (3) In/Ag (In top layer), (4) Ag/TiO_2 and Ag/ZrO_2 (Ag as top layer) and (5) Au/TiO_2 and Au/ZrO_2 (Au as top layer) bilayer thin films.

The motivation of this work is two fold. One is to investigate the effect of the metal-metal interface on SPR behaviour. It has been shown in core-shell metal nanostructures that there is large tunability of SPR accompanied by spectral splitting of the SPR peak due to plasmon hybridization. The possibility of demonstrating a similar effect in metal bilayer is investigated. The second objective is to study the effect of dielectrics environment on the optical response on metal-dielectric bilayers. There are many studies on core-shell metal-dielectric nanostructures. In this study, however, it is shown that similar effects can also be realized in metal-dielectric bilayer systems in a much simpler fashion.

Bilayer metal thin films of Ag/Au and Au/Ag were deposited by ion beam sputter deposition techniques at very low ion energy (150 eV- 250eV). The thickness of bottom metal layer was kept constant where as the thickness of top metal layer were varied in both the cases Ag/Au and Au/Ag bilayer. It was observed that the optical absorption spectra exhibit features from both metals. In general, at a fixed thickness of the lower metal layer, there is a red shift in the SPR peak with increase in top metal layer thickness.

In/Ag bilayer thin films were fabricated by maintaining the Ag layer thickness constant at 5 nm while varying the In layer thickness between 3 to 30 nm. It is observed that the grain size in the films increased with increase in thickness. In the case of the single layer In films the grain size increased from 60 to 350 nm as the thickness increased from 3 to 30 nm while the grain size increased from 80 to 280 nm in as the bilayer thickness increased from 8 to 35 nm. There is a red shift in the plasmon resonance from 372 to 522 nm in the case of the pure In layers whereas it was from 492 nm to 618 nm for the bilayer system. On coupling the In and Ag layers in the bilayers, additional resonances appear in

the spectrum. These shifts are shown to be attributable to the phenomenon of Plasmon hybridization.

In the metal-dielectric case, the metal layer Ag or Au is deposited on top of the dielectric layer, which is either TiO_2 or ZrO_2. The dielectric films were prepared by the sol-gel method whereas the metal films (5-50 nm thick) were deposited on to the dielectrics by ion beam sputter deposition. The bilayer thin films show enhanced light absorption in the ultraviolet region and refractive index controlled optical absorption at near infrared wavelengths. In addition, they display the tunability in surface plasmon resonances exhibited normally by core-shell and bimetal nanostructures. In the presence of the metal layer, the absorption coefficient of the bilayer is enhanced, by almost 7 times, in the region of the band gap. The surface plasmon resonance of the metal exhibits a red-shift with increase in refractive index of the dielectric underlayer. The plasmon resonance for Ag is observed at a wavelength of 424 nm on ZrO_2, which shifts to 434 nm on TiO_2. Similarly in the case of Au films, the shift is from 630 nm on ZrO_2 to 640 nm on TiO_2. Interestingly, the optical absorption in the near IR region increases with increase in refractive index of the dielectric underlayer. A detailed comparison of the optical response of metal-metal and metal-dielectric systems is presented.

Chapter VI: Overview of the Present Work and Future Prospects

In this chapter, the results of the current work are summarized and the scope for the future work is reviewed.

Publications relevant to this thesis:

1. **Rajeeb Brahma** and M. Ghanashyam Krishna, Ion beam sputtered ultra-thin and nanostructured Ag films for surface plasmon applications, Nucl. Instr. and Meth. in Phys. Res. B, **266** (2008) 1493-1497.
2. **Rajeeb Brahma** and M. Ghanashyam Krishna, Optical response and surface morphology of In/Ag bilayer thin films, Materials Chemistry and Physics, **124** (2010) 150-154.
3. **Rajeeb Brahma** and M. Ghanashyam Krishna, Optical behavior of Ag/dielectric and Au/dielectric bilayer thin films, Physica E, **43** (2011) 1192-1198.
4. **R. Brahma**, G. Mahipal Reddy, P. Anantha Lakshmi, Suneel Singh and M. Ghanashyam Krishna, Controlled nanostructuring of Ag films by low energy ion beam sputter deposition and its impact on surface plasmon resonance behaviour, J. Nanosci. and Nanotechnol., Vol. **11** (2011) 1-9.
5. **Rajeeb Brahma** and M. Ghanashyam Krishna, Optical response of Ag/Au and Au/Ag bilayer thin films deposited by ion beam sputtering, AIP Conf. Proceed. Vol **55** (2010) 1349.
6. **Rajeeb Brahma** and M. Ghanashyam Krishna, Interface controlled growth of nanostructures in discontinuous Ag and Au thin films fabricated by ion beam sputter deposition (communicated).
7. **R.ajeeb Brahma**, K. Subba Rao and M. Ghanashyam Krishna, Abonormal coalescence behavior of ion beam sputter deposited discontinuous silver and gold thin films (communicated).

Other publications:

1. **Rajeeb Brahma** and M. Ghanashyam Krishna, Optical, structural and electrical properties of Mn doped tin oxide thin films, Bull. Mater. Sci. Vol. **29**, No. 3 2006), pp. 317-322.
2. Koppolu Uma Mahendra Kumar, **Rajeeb Brahma**, M Ghanashayam Krishna, Anil K Bhatnagar and G Dalba, An optical study of Ni induced crystallization of a-Si thin films, J. Phys: Condens. Matter **19** (2007) 496208.

Conferences (International / National):

1. A seminar has been attended on **Optics of Photonic Band-gap Materials** held at the Department of Physics and Meteorology, Indian Institute of Technology, Kharagpur from 28th to 30th October 2005.
2. **Rajeeb Brahma**, Anil K Bhatnagar and M. Ghanashaym Krishna, Studies on pure SnO_2 and Al doped SnO_2 transparent conducting thin films, 50th (golden jubilee) DAE solid state physics symposium at Bhabha Atomic Research Centre, Mumbai and Tata Institute of Fundamental Research, Mumbai during December 5 – 9, 2005.
3. **Rajeeb Brahma** and M. Ghanashyam Krishna, Self organized nanostructured Semi-conducting thin films, ICONSAT 2006, organized by Nano Science and Technology initiative Department of Science and Technology Govt. of India. And Indian Institute of Technology Delhi, New Delhi, India.
4. **Rajeeb Brahma** and M. Ghanashyam Krishna, Particle size dependent surface plasmon resonance in ion beam sputtered Ag films, IBA 2007, 18th International Conference on Ion Beam Analysis, 23rd – 28th Sept 2007, Hyderabad.
5. Koppolu Uma Mahendra Kumar, **Rajeeb Brahma** and M. Ghanashyam Krishna, Optical properties of ion beam sputtered wide band gap a-Si thin films, IBA 2007, 18th International Conference on Ion Beam Analysis, 23rd – 28th Sept 2007, Hyderabad.
6. M S R N Kiran, **R Brahma** and M. Ghanashyam Krishna, Nanoindentaion studies on nanocrystalline indium films, 53rd DAE solid state physics symposium (2008).
7. Prashanth kumar, **Rajeeb Brahma** and M. Ghanashyam Krishna, Processing controlled surface plasmon resonance behaviour for nanostructured metallic films, International conference on transport and optical properties of nanomaterials (ICTOPON-2009).
8. **R Brahma** and M. Ghanashyam Krishna, Ag nanostructures fabricated by ultra-low energy ion beam sputtering leading to tunable Plasmon resonance, Nanomaterial's, Applications and Nanotechnology Developments (NAND 2009), Hyderabad.
9. **Rajeeb Brahma** and M. Ghanashyam Krishna, Optical response of Ag/Au and Au/Ag bilayer thin films deposited by ion beam sputtering, 55th DAE-Solid State Physics Symposium, December 2010, Manipal University, Manipal.

Chapter I: Introduction

Abstract

This chapter presents the state-of-literature on the optical properties of Ag and Au metal nanostructures and their applications.

Chapter I: Introduction

1.1. Introduction

Finite size effects in metals have been the focus of interest of researchers for over a century. Today metal nanostructures are attracting increasing attention due to their unique optical and electrical properties compared to the bulk metals. These metal nanostructures have great potential for applications in several fields of science such as medicine, optics, and electronics. It is known that below a particular size, the band structure of metals consists of discrete energy levels and quantum mechanical rules replace those of classical physics. Size provides an important control over the physical and chemical properties of nanoscale materials. The structural anisotropy of metal nanostructures show substantially different optical properties. The remarkable size, surface and shape dependence of the physical and chemical properties of metal nanostructures make them excellent candidates in modern technology. Specially, the optical properties can be tuned by controlling the shape and sizes of particles that constitute these nanostructures. Interest and the importance of metal nanostructures continues to grow for the following reasons.

1. The ease of fabrication has motivated experimental progress in understanding the intrinsic size and shape dependent properties.
2. Some of these structures feature optical and electrical properties that make them desirable for emerging applications including biolabels, photovoltaic behavior, chemical sensing, surface enhanced Raman spectroscopy (SERS), plasmonic wave guide etc.
3. The growth mechanism of nanoparticles is amenable to theoretical study, which in turn makes possible the prediction and systematic manipulation of the final nanocrystal structure.
4. These nanoparticles provide new template materials for the generation of different nanostructures [1, 2].

One of the main reasons that great attention is given to metal nanostructures originates from the strong absorption they possess in the visible region of the electromagnetic (EM) spectrum. The most commonly studied metals are Ag, Au and Cu but among these, Ag

and Au have attracted more attention in a number of disciplines because their surface plasmon resonance peaks occur at visible wavelengths that are particularly suitable for applications.

Gold and silver are among the most widely used metals in the world. Their metallic properties make them good conductors. The anti-microbial properties of Ag are also being exploited in several applications. Reducing Ag and Au to nano-sized particles helps to make the element highly effective, increasing their demand for use in medicine and electronics. One of the most fascinating characteristics of nano sized Ag and Au particles is their optical properties. In the nanoscale range, silver and gold exhibit strong absorption in the visible region of the spectrum with rich colors, e.g., yellowish for silver and burgundy for gold spherical particles [3-8]. The origin of this absorption is attributed to collective conduction band electron oscillations in response to the electric field of the electromagnetic radiation of light. This optical absorption is termed surface plasmon resonance (SPR). Surface plasmon resonance (SPR) is coherent oscillation of conduction electrons on the metal surface excited by electromagnetic radiation at a metal dielectric interface. The SPR depends on dielectric constant of metal nanoparticles and the surrounding dielectric matrix [9-25]. Surface plasmon resonance of these metal nanoparticles is responsible for their ability to strongly absorb and scatter light at some specific wavelengths. Plasmon resonance properties can be exploited for surface enhanced Raman scattering (SERS) application, which uses the evanescent field at the surface of nanostructured materials to greatly amplify the weak, but molecule specific Raman signal [26, 27]. SERS has been used for a wide range of applications in physics, chemistry and recently biology as well as biochemistry [28-33]. However, SERS is not the only application that has found major applications among those from metal nanoparticles. Surface enhanced fluorescence [34, 35], surface plasmon resonance imaging [36, 37], surface plasmon resonance spectroscopy [38, 39] and surface enhanced second harmonic generation [40,41] are other examples that have demonstrated the advantages and promised of metal nanostructure for other applications. Metal nanostructures in the form of thin films are very important in optoelectronics, solar cells, sensors, magneto-optics, photonics and in many other applications [42-45].

Experimental and theoretical work on metal thin films has been conducted by many researchers. The growth of metal thin films and study of their microstructure, structure

and optical properties forms the focus of the current thesis. The state of art in this field is reviewed in the following section. Xu *et al.* have reported on influence of substrate on tunability of the localized surface plasmon resonance wavelength, λ_{spr}, of silver island films deposited by magnetron sputtering on different substrate. They have shown that it leads to red shift and also extendable to large tunable range in λ_{spr}. Such kind of effect can be greatly enhanced by increasing the mass thickness of the metallic islands. The resonance wavelength of an island film can be readily adjusted from the visible to the near infrared region of the electromagnetic spectrum. The capability of tuning the resonance wavelength can be effectively enhanced by increasing the refractive index of the substrate and the mass thickness of the metallic islands. In this way, the SPR wavelength of a standard silver island film was readily adjusted from around 450 nm to 948 nm in the near infrared region and also, the sensitivity of the SPR wavelength to the interisland dielectric constant was found to be dependent on the silver mass thickness [46]. Sonnichsen *et al.* have investigated the optical properties of spherical gold and silver clusters with diameters of 20 nm and larger. The light scattering spectra of individual clusters were measured using dark-field microscopy avoiding the inhomogeneous broadening effects. The dipolar plasmon resonance of the cluster were found to have nearly Lorentzian line shapes. Polaritonic red shifts of the plasmon line and increased radiation damping for both gold and silver clusters were observed with the increase of size. They concluded that apart from cluster to cluster variations of the plasmon lines, agreement with Mie theory is reasonably good for the gold clusters but it is less satisfactory for the silver clusters, possibly due to cluster faceting or chemical effects [47]. Aussenegg *et al.* have reported that in metal-island kind of films with nanometre particle size on a transparent substrate, the irradiated light field can be locally enhanced by electron-plasma resonances. Therefore, nonlinear optical processes should be enhanced dramatically. However, second-order nonlinear processes as second-harmonic generation occurring in the surface are strongly reduced by the centrosymmetric shape of the metal particles. Thus observed that this surface-specific contribution to second-harmonic generation is less enhanced as is expected from the field enhancement [48]. Gonzalez *et al.* have theoretically studied the influence of morphology on the optical properties of metal nanoparticles using the discrete dipole approximation and established a general relationship between the surface plasmon resonances and the morphology of each nanoparticle. It is found that as the size truncation of the cubic nanoprticle becomes larger, the main resonance is blue shifted, overlapping secondary resonances, and

therefore, increasing the full width at half maximum of the main resonance. For decahedral particles, the truncation to marks and rounded decahedra shows the same blue shift effect but the full width at half maximum of the main resonance decreases, maybe because the secondary resonances no longer exist. It is also observed that nanoparticles with fewer faces, like the star decahedron, show resonances in a wider range of wavelengths, perhaps because these geometrical shapes have sharper vertices as compared to the others [49]. Hao *et al.* synthesized Au nanoshells via wet-chemical methods and TEM results showed the indication of non continuous pinhole (several nm) structures. By using the discrete dipole approximation and Mie theory, it was observed that the optical properties of metal nanoshells depend strongly on their size and shell thickness. The calculation showed that the 2-5 nm pinholes have only a small effect on the extinction spectra; however, they lead to local electric fields that are enhanced by a factor of 3-4 close to the plasmon maximum which means metal nanoshells (with holes) is attractive material for surface enhanced Raman spectroscopy applications [50]. Oates *et al.* have reported on evolution of plasmon resonances during plasma deposition of silver nanoparticles. In situ real-time spectroscopic ellipsometry was used to monitor the growth of magnetron sputtered silver nanoparticles on SiO_2 substrates, through the percolation threshold and into the bulk film regime. In this work, they have modelled the plasmon polariton resonances in the nanoparticulate regime by a Lorentz oscillator. The resonance energy of the oscillator is observed to reduce to zero shortly after the percolation threshold, where the oscillation is described by Drude free electron theory. The use of a generalized Lorentz oscillator to model the data, in which the plasmon oscillation is assumed to evolve into the Drude free electron oscillation soon after percolation, allows the Drude theory to be applied qualitatively to the nanoparticulate regime. This provides insights into the evolution of the electron mean free path during the deposition. The appearance of a second Lorentz oscillator before the percolation threshold is attributed to coupling of the plasmon polaritons, and determined to occur at a surface area coverage of Q=0.52 [51]. Mertens *et al.* have presented a study of two-dimensional arrays of silver nanoparticles embedded in amorphous silicon, fabricated by a sequential Si/Ag/Si electron-beam evaporation process. These particle arrays exhibit surface plasmon resonance spectra in the near-infrared (0.9 eV), with tails extending below 0.5 eV. They have described a model for the ensemble averaged plasmon absorption, with experimentally determined Ag nanoparticle size and shape as input, taking into account the refractive index of the matrix, shape anisotropy, and interparticle coupling. It is

observed that the large red shift is mainly due to the high refractive index of the matrix, with shape anisotropy and interparticle coupling contributing several tenths of an electron volt. Their data indicates that an increased Ag deposition thickness leads to larger shape anisotropy and thus larger plasmon redshifts. By further increasing the Ag layer thickness even larger plasmon redshifts may thus be observed. This achievement of infrared surface plasmons in silicon enables the use of electromagnetic field enhancements, surface-enhanced Raman scattering, spontaneous emission enhancement, nanoscale energy transfer, and several other plasmon-related applications at the important telecommunication wavelength of 1.5 μm [52]. Sosa *et al.* have carried out a theoretical calculation using discrete dipole approximation (DDA) to study the main optical features of the extinction, absorption, and scattering efficiencies of nanoparticles of different sizes and shapes of silver and gold. The different geometries considered here are spheres, ellipsoids, cubes, terahedra, cylinders, and pyramids and in most of the cases, it is clearly identified the main optical signature associated to each geometry. It is observed that the spectra are more complex as the particle has less symmetry and/ or has more vertexes. It is found that in the spectra the main surface plasmon resonance associated to a dipolar excitation, as well as other resonances due to high-multipolar excitations. The physical origin of these high-multipolar excitations might have two different sources, one due to the shape and the other due to the size of the particle. In the case of silver particles, specific features in the optical spectra can be associated to either geometry, size, or material properties, making optical spectrocopies a very helpful tool for the characterization of nano particles during and after growth [53]. Zhang *et al.* provided an overview of recent research activities in the study of plasmonic optical properties of metal nanostructures with emphasis on understanding the relation between surface plasmon absorption and structure. They have done both experiment and theoretical calculation and the results have indicated that the plasmonic absorption strongly depends on the detailed structure of the nanomaterials. Here, examples discussed include spherical nanoparticles, nanorods, nanowires, hollow nanospheres, aggregates, and nanocages and also plasmon-phonon coupling measured from dynamic studies as a function of particle size, shape and aggregation state is also reviewed. These kind of fascinating optical properties of metal nanostructures find important applications in a number of technological areas including surface plasmon resonance, surface-enhanced Raman scattering, and photo thermal imaging and therapy. Their novel optical properties and emerging applications are illustrated using specific examples from recent literature. The case of hollow nanosphere

structures is highlighted to illustrate their unique feature and advantages for some of these applications [54]. Choi *et al.* have investigated the optical properties of silver nanoparticles films prepared by the chemical synthesis of well-controlled silver nanoparticles to control the particle size, spacing and ordering. They have found that the extinction spectrum of the film shows three apparent peaks which are different from those of colloidal nanoparticles. They also showed that one peak at 390 nm comes from isolated nanoparticles and the other two peaks at 360 nm and 580 nm come from neighbouring nanoparticles due to interparticle dipole-dipole coupling by obtaining extinction spectra of the silver nanoparticle film for different in-plane and out of plane contributions of linearly polarized components. They also carried out thermal treatment and the thermal treatment causes neighbouring nanoparticles to be fuse and the extinction peaks due to the dipole-dipole couplings disappear. Dielectric surroundings such as SiO_2 and TiO_2 layers cause the extinction peaks of the silver nanoparticles to red-shift [55]. Evanoff *et al.* reviewed systematically the optical properties of silver nanoparticles as a function of size, extinction, scattering, and absorption cross-sections and distance dependence of the local electromagnetic field, as well as the quadrupolar coupling of 2D assemblies of such particles for a wide range of particle sizes. Such measurements were possible because of the development of a novel synthetic method for the size controlled synthesis of chemically clean, highly crystalline silver nanoparticles of narrow size distribution. It was observed that for nanoparticles much smaller than the wavelength of light, the EM field is uniform across a particle such that all the conduction electrons move in-phase producing only dipole-type oscillations manifested by a single, narrow peak in the surface plasmon polariton spectrum. As the size increases, the field across the particle becomes nonuniform, and this phase retardation broadens the dipole resonance and excites higher multipole resonances, such as the quadrupole, octupole, etc. leading to several peaks in the spectra. The hydrogen reduction synthesis method fulfils the requirements of different shape, size for silver nanoparticles and perhaps other metals. Because of the chemical purity of the suspensions and the control that this method provides over particle size and distribution, the particles can be easily incorporated into a variety of nanocomposites and further assembled into higher order nanostructures that exhibit novel properties [56]. Gupta *et al.* have reported on the precise control of thermal evaporation deposition parameters which allow the reproducible production of silver and gold island films on glass substrates with tunable surface plasmon resonance wavelengths. It is shown that thermal evaporation is an effective technique for producing Ag and Au metal island films

with tunable surface plasmon resonance wavelengths. They have developed the process and analyzed using a 15-run 3-level Box_Behnken experimental design. Specific combinations of substrate temperature, deposition rate, and film thickness produce films exhibiting surface plasmon resonance wavelengths that can be adjusted from throughout the visible and into the near infrared regions of the electromagnetic spectrum. An empirical predictive equation, second order in the three deposition parameters, was shown to accurately model and predict surface plasmon resonance wavelength values. The process was found to be capable of reproducibly producing films exhibiting specific surface plasmon resonance wavelength values. The most influential morphological effect on surface plasmon resonance wavelength was determined to be the X-Y in-plane particle size [57]. Pile *et al.* have reported numerical analysis and the first experimental observation of a new type of strongly localized plasmon modes guided by a rectangular gap in a thin metal film/membrane. They claim that these plasmon modes may be one of the best options for the design of all-optical nanocircuits and devices, mainly because of their significant propagation distance, very strong localization, expected low bend losses, relatively simple fabrication of the required structures. Dispersion, dissipation, and field structure of these modes are analyzed using the finite-difference time-domain algorithm. The experimental observation is conducted by the end-fire excitation of the proposed gap plasmon waveguides and detection of the generated modes using their edge scattering and charge coupled device camera imaging [58]. Chaturvedi *et al.* reported a smooth and low loss silver optical superlens capable of resolving features at 1/12th of the illumination wavelength with high fidelity. They have demonstrated a unique approach to realize ultra smooth Ag superlenses with an unprecedented 1/12 resolution capability. Incorporating few monolayers of Ge drastically improves Ag film quality and minimizes the subwavelength information loss due to scattering. The theoretical and experimental results clearly indicate sub diffraction imaging down to 30 nm half-pitch resolution with 380 nm illumination. This ultrahigh image resolution capability can also be extended to far-field by incorporating a corrugated silver surface on top of Ag–Ge superlens. The development of such unique superlenses would enable real time dynamic imaging at the molecular level [59]. Oates *et al.* presented in situ spectroscopic ellipsometry investigations of the growth of ultra-thin silver films, from island growth through percolation and continuous film growth. Silver films were deposited using a pulsed filtered cathodic vacuum arc, which provides precise control and reproducibility of the film growth conditions. They have calculated the plasmon polariton resonances for the

growing islands below the percolation threshold. As the surface coverage increases a second oscillator, attributed to bulk plasma resonances, is required to accurately model the ellipsometric data. Post deposition optical and electronic changes are observed for island films and the origins of these changes are investigated using the ellipsometric data. The ellipsometric data suggests an increase in the island aspect ratio in the first few minutes after the deposition. It is observed that instabilities in the optical and electronic properties of island films were evident for in excess of 1 h after the end of the deposition process. [60]. Farcau *et al.* have demonstrated a noble metal nanostructured substrate for fluorescence enhancement that possesses tunable plasmonic properties. They have deposited regular arrays of interconnected silver half-shells on self-organized polystyrene microspheres as plasmonic substrates for metal-enhanced fluorescence. An emission enhancement of 28 times was demonstrated for Rose Bengal fluorophore placed at about 1 nm above HSs. The enhancement correlates with the spectral overlap between the fluorophore emission and the plasmonic resonance of the half-shells, indicating a surface plasmon-coupled emission mechanism for the amplification. As the overlap can be easily tuned by controlling the diameter of underlying microspheres, such plasmonic structures could be relevant for building fluorescence-based sensing devices with optimized efficiency for any given fluorophore. It is observed that by changing the diameter of the spheres template, the SP resonance of the noble-metal half-shell arrays can be controlled, which in turn allows the optimization of the enhancement efficiency for the desired fluorophore. The proposed MEF substrate is highly versatile, providing the ordering, robustness, reproducibility, and tunability of top-down lithographically fabricated structures, complemented by the ease of fabrication and low-cost of bottom-up approaches. Therefore they claimed that this kind of ordered noble metal nanostructure should straight forwardly find its way into practical fluorescence-based sensing or analytical applications [61]. Yang *et al.* have reported on “Silver nanocrystals modified microstructured polymer optical fibres for chemical and optical sensing”. In this report they have demonstrated fibre chemical and optical sensors based on silver nanocrystals modified microstructured polymer optical fibres (MPOFs). The silver nanocrystals modified MPOFs were formed by direct chemical reduction of silver ammonia complex ions on the templates of array holes in the microstructure polymer optical fibres. They have deposited silver nanocrystals in 18 holes in MPOF by using liquid-phase coating method. The nanotube-like and nanoisland-like Ag-modified MPOFs could be obtained by adjusting the conditions of Ag-formation in the air holes of MPOFs. It is found that

tubular Ag- MPOF composite fibre was conductive and could be directly used as array electrodes in electrochemical analyses. It displayed high electrochemical activity on sensing nitrate or nitrite ions. These new types of complex fibre materials are claimed to be important in the fields of electrochemical sensor and MEF-based fibre devices [62]. Politano *et al.* have reported the effects of the annealing procedure at 400–450 K on the electronic properties of nanoscale thin films of Ca, Au and Ag grown on Cu (1 1 1) at room temperature were probed by high-resolution electron energy loss spectroscopy measurements. Ca surface plasmon underwent to a significant red-shift upon annealing, due to the oxidation of the topmost Ca layer. A CaO layer (highly reactive towards hydrolysis at room temperature) was formed upon annealing, while for the Au film the formation of an Au– Cu alloy was observed by both HREELS and AES measurements. It is observed that Au surface plasmon disappeared upon annealing the gold film, as a consequence of the formation of an Au–Cu alloy whereas, Ag surface plasmon red-shifted both in the annealed adlayer and with increasing temperature compared with the frequency recorded for the as-deposited silver film [63]. Tominaga has reported that silver oxide thin films may be a very useful material for dealing with optical near-field and surface plasmons. Silver oxide decomposes into oxygen and small metallic silver particles, and this characteristic has been applied to ultrahigh-density optical data storage to create a strong light-scattering centre that resolves small pits or marks beyond the diffraction limit. He has described the unique characteristics of AgO*x* layers, and their application to photonic devices using surface plasmons and localized surface plasmon. The deposited layer can be transformed into Ag nanoparticles and nanowires in a gas mixture of H_2 and O_2. The diameter and space between each wire or particle can also be controlled over a limited range by feeding a seed gas before or during the reduction process. The author claims that in future this material will play an important role in near-field optics and surface plasmon engineering, as well as in advanced optical storage [64]. Choi *et al.* have investigated the characteristics of transmitted light from propagating surface plasmons based on rectangular silver gratings. The results calculated by rigorous coupled-wave analysis presented that silver diffraction gratings can produce significant transmittance and conversion efficiency, comparable to the case of dielectric gratings. From the calculations, it is found that when λ=633 nm and a fill factor is fixed at 0.5, rectangular silver gratings presented a notable performance in terms of transmittance and conversion efficiency (CE). As a practical sensing application, silver grating-mediated SPR structure in a water ambience showed a notable SPR signal amplification, which is

associated with strong excitation of LSP modes and an increased surface reaction area. This study shows the potential of using transmitted SP waves in a variety of optical applications, such as optical imaging system, optical biosensor, and light sources [65]. Vasilyuk *et al.* investigated the interdependencies between the optical, morphological and enhancing silver films (SFs) characteristics by using the methods of mathematical statistics. The study demonstrate correlating between the optical density maximum value with the distance between the islands and their shapes coefficient and the optical density maximum value ratio to halfwidth band of the optical density with the similar islands characteristics. The increase of both the optical density and SERS intensity values happens as a result of structurally dependent resonant increase of a local surface electromagnetic field of silver clusters (islands) in case of comparable sizes of islands and distances between them. [66]. Ye *et al.* have studied the coupling of surface plasmons between two silver films in a $Ag/SiO_2/Ag$ plasmonic thermal emitter with grating structure. In this article, they have experimentally investigated the reflection and emission spectra of Ag/SiO_2 /Ag trilayer plasmonic thermal emitters with different thicknesses of SiO_2. The top Ag film is perforated with periodic slits. The top and bottom surface plasmon (SPs) will couple together when SiO_2 layer is thin, which increases effective refractive index (n_{eff}) and results in the redshift in the thermal emission peak. As the thickness of SiO_2 continues to increase, the Ag/SiO_2 localized surface plasmon polariton (LSPP) modes become weaker and finally disappear. When the SiO_2 layer is thick enough, the Ag/SiO_2 grating-coupled SP modes become dominant and the dispersion relation of Ag/SiO_2 (±1) modes almost coincides with the theory [67]. Perea-Popez *et al.* have shown a simple experimental process to produce small holes in thin gold or silver films simply by applying voltage while doing insitu AFM measurement. The method is simple because it does not involve the usual sputtering process and complicated substrate preparation, nor does it require local probe manipulations. They have used the process to produce small holes in gold films of up to 135 nm in thickness. The process works for films as thin as 25 nm. For thinner films, the process forms particle-like structures instead of small holes and they believe that the produced films would find applications in optical studies on surface plasmon induced transmission as well as other related phenomena [68]. Zhao *et al.* presented an approach for simultaneously synthesizing and immobilizing silver nanoleaves (SNLs) on γ-mercaptopropyltrimethyoxysilane (MPTS)-modified chemical vapor deposited (CVD) diamond film surface. The thickness of SNL layer deposited onto the CVD diamond substrate increased with increasing the deposition time

and the formation mechanism of SNL films was also discussed. The method reported provides a versatile and facile pathway to fabricate anisotropic nanostructures onto the inert diamond film surfaces. Their performance as surface-enhanced Raman scattering (SERS) substrates was evaluated by using rhodamine 6G (R6G) as the probe molecule. It is observed that in comparison with self assembled silver nanoparticle film and silver film from the mirror reaction, the SERS signal of R6G was obviously improved on the SNL films. Therefore, they have claimed that the SNL-modified diamond film, as a SERS active substrate could open up tremendous possibilities for exploiting it in highly sensitive sensors for chemical and biological species analysis [69]. Godbole ***et al.*** deposited silver films on glass substrate by solid-liquid interface reaction technique (SLIRT) and then the solid film of silver nitrate is formed by spin coating method. These films were subsequently processed by dipping it in a reducing solution so as to initiate a reaction at the interface and ultimately transform in to totally silver film. The insitu transformation of silver nitrate to silver is studied with respect to time, spectrophotometrically. They have characterized the prepared silver film by XRD, DPS, TEM and UV visible spectroscopy. It is observed that the complete reduction reaction is reflected in the saturation of absorption peak in the region 375-425 nm [70]. Tsai ***et al.*** demonstrated extraordinary optical transmission through a two-dimensional Ag film in the far infrared region. Here, holes were rectangular and arranged in a square lattice. When either the width or the length size of the rectangular holes was close to the half of the lattice constant $a/2$, the degenerate (±1, 0) Ag/Si or (0, ±1) Ag/Si modes split into two peaks. Additionally, the surface plasmon dispersion relations of the square hole array with different aspect ratios of holes were measured. It is observed that as the aspect ratio increased, the surface plasmon tended to couple strongly with the local charge dipole oscillations in a direction perpendicular to the long edges. The charge dipole oscillation parallel to the long edges gradually disappeared. This was confirmed by experiments using the polarized light. The direction of the electric field oscillation and that of the light propagation both affected the SPP dispersion relation. The dynamic properties of the surface plasmon dispersion relations show the interaction among localized surface plasmons and its mechanism [71]. Benia ***et al.*** investigated the optical properties of silver nano-particle ensembles as a function of particle density by analyzing the light emission excited via electron injection from an scanning tunnelling microscope (STM) tip. The particles are prepared with distinct dome and disk-like shapes on a Al_2O_3/NiAl(110) support. The particle density is varied over one order of magnitude by changing the Ag

deposition temperature and the defect concentration in the oxide surface. The optical spectra of so-prepared ensembles are dominated by (1, 0) Mie plasmon excitations. For dome-shaped particles, the Mie mode shows a distinct blue shift with increasing particle density, attributed to destructive coupling of out-of-plane dipoles in the particle layer. For disk-like particles nearly constant plasmon energies are detected, manifesting the reduced influence of dipole–dipole interactions for extremely flat particles. The experiments demonstrate the possibility to tune the optical properties of Ag particle ensembles exclusively by changing the inter-particle separation. The observed evolution of plasmon energy as a function of particle density reflects the influence of electromagnetic interactions in the ensemble, as verified by model calculations [72]. Gryczynski *et al.* demonstrated coupling of excited fluorophores with thin silver or gold films resulting in directional surface plasmon-coupled emission (SPCE) through the silver film and into the glass substrate. They have further investigated the spectral and spatial properties of SPCE from sulforhomamine 101 in polyvinyl alcohol (PVA) films of various thicknesses on 50-nm silver films. Multiple rings of SPCE and unusual s-polarized emission were observed. These are consistent with the expected waveguide modes in the silver-PVA composite film. However, in contrast to their expectations, the average lifetimes of SPCE were not substantially changed from the PVA films. This observation of SPCE at multiple angles and with different polarization can open new opportunities for the use of SPCE to study anisotropic systems or to develop unique sensing devices [73]. Kuzik *et al.* studied the effect of a noble metal (silver or copper) island film on the vibrational spectrum of a natural aluminium oxide film using the reflection-absorption spectroscopy technique. It was found that the intensity of the absorption band of aluminium oxide near 950 cm^{-1} changes drastically after the deposition of the metal over layer. This band intensity increases rapidly with increasing of the silver film thickness more than twice, reaching the maximal value at the silver thickness 0.2 nm, then the band does not change up to the thickness 2 nm. It was observed that such behavior takes place only in the presence of aluminium under oxide film. Therefore, they have suggested that this increase of the absorption band intensity is due to the increase of the aluminium oxide film thickness, caused by an electrochemical reaction resulting in aluminium anodic oxidation. For thicker silver films the intensity of the aluminium oxide band falls down slowly due to a metal screening effect. It will be interesting to study the effect of the thin metal film on the band of the aluminium oxide created by aluminium oxidation in ultrahigh vacuum conditions and to investigate the role of water in the increase of the band intensity [74].

Maaroof *et al.* demonstrated two distinct electrically percolated types of nanostructured silver (n-Ag) films on glass substrates by optically and structurally characterizing and determining effective refractive indices. Sputtered silver films above the percolation threshold display, over a small range of thicknesses, a wide range of complex refractive indices across the visible and near infrared. It is found that even though these films are electrically continuous their nano-grain and nano-void structure contribute to a significant shift from bulk response. Electrically continuous films of different structure can thus have widely varying optical response. Grain boundary scattering of electrons is found to play a role but void content seems to dominate these changes. Extended surface plasmons on the film surface or local induced currents are observed when an oxide covers the surface and fills the voids. The latter causes a surprising shift back to ‘‘normal’’ like metal spectral behaviour, which may indicate a damping of surface plasmon polariton coupling across the film. The dielectric properties of the neighbouring medium are known to have a marked effect on SPP properties which are further complicated by the voids. It appears from the absorptance changes that with no overcoat much incident light is in effect being shunted through the voids and does not see the metal, while with the overcoat the reverse occurs and light passes mainly through the metal causing much more attenuation [75]. Altube *et al.* reported about the preparation and optical characterization of technologically relevant silver based nanostructures by metal infiltration of monolayered or opal-like templates of polystyrene (PS) latex spheres. They have demonstrated that low toxicity electrolytic baths present obvious advantages and facilitate the synthesis, and are therefore, desirable methods for this kind of processes. Optical reflectance spectroscopy analysis shows that high quality films may be obtained by this method [76]. Subrahmanyam *et al.* demonstrated growth of silver doped indium oxide ($In_{2\_x}\ Ag_x\ O_{3\_y}$) thin films on glass and silicon substrates at room temperature (300 K) by reactive DC magnetron sputtering technique using an alloy target of pure indium and silver (80: 20 at%). The magnetron power (and hence the metal atom sputter flux) is varied in the range 40–80 W. The energy dispersive analysis of X-ray (EDAX) results showed that the silver content in the film decreases with increasing magnetron power. The grain size of these films was found to be of the order of 100 nm. The resistivity of these films is in the range 10^{-2}–10^{-3} Ωcm. it is found that the work function of the silver-indium oxide films (by Kelvin Probe) are in the range: 4.64–4.55 eV. The refractive index of these films (at 632.8 nm) varies in the range: 1.141–1.195. The optical band gap of indium oxide (3.75 eV) shrinks with silver doping. Calculations of the partial ionic charge (by Sanderson’s

theory) show that silver doping in indium oxide thin films enhance the ionicity *i.e.* the silver may be present in more than one valence state, the partial ionic charge on the oxygen is observed to increase with decreasing silver [77]. de Vries *et al.* investigated the optical properties of a growing silver film starting from predeposited gold nanoparticles using spectroscopic ellipsometry in the visible and near-infrared spectral range. The effective pseudo dielectric functions, obtained by direct inversion of the ellipsometry spectra, reveal a surface plasmon resonance for the nanoparticulate films. Upon prolonged electroless silver deposition, the resonance shifts to lower energies. For longer deposition times, the optical spectra can be described in terms of a Drude-like free-electron metal. The development of the Drude–Lorentz parameters, *i.e.*, the relaxation time and electron density, are compared to values for bulk silver; the latter were obtained from an optical measurement on a thick bulk silver sample. The saturation values for the relaxation time and thus the conductivity amount to approximately 40% of the bulk value, in agreement with direct current conductivity measurements on these films [78]. Winter *et al.* have shown that the emission of light from a dye layer through an adjacent thin silver film is maximal for a silver thickness of approximately 50 nm. This effect is explained as the result of competition between enhancement of the electric field at the metal surface due to the excitation of a surface plasmon-polariton mode, the amount of power coupled to the surface plasmon-polariton mode, and the attenuation of the field transmitted through the silver, all three of which vary with metal thickness. These results have relevance for a variety of applications; including the development of fluorescence biosensors and top-emitting organic light-emitting diodes [79]. Bobb *et al.* have reported alloying a noble metal (gold) with another metal (cadmium), which can contribute two electrons per atom to a free electron gas, can significantly improve the metal's optical properties in certain wavelength ranges and make them worse in the other parts of the spectrum. In particular, in the gold-cadmium alloy it is demonstrated a significant expansion of the spectral range of metallic reflectance to shorter wavelengths. The experimental results and the predictions of the first principles theory demonstrate an opportunity for the improvement and optimization of metals for nanoplasmonic and metamaterials applications. [80]. Ghoshal *et al.* have investigated the excitation of propagating surface plasmons (SPs) on a silver-silica interface by an array of ellipsoidal silver nanoparticles using numerical simulations as a function of particle volume for three different nanoparticle aspect ratios with representative resonance frequencies. They observed that while the SP amplitude depends sensitively on particle volume for each

selected aspect ratio, the maximum SP amplitude obtained for the different particle shapes is remarkably similar. These observations are explained in terms of particle-mediated SP excitation, counteracted by a size dependent particle-induced damping. The results indicate that control over the NP resonance frequency does not strongly affect the SP excitation efficiency in large NP-enhanced grating couplers if the NP volume can be freely modified, but does affect the NP volume at which maximum SP excitation occurs. They have presented an analytical model that quantitatively describes the observed trends in SP damping [81]. Chang *et al.* prepared metallic circular slits onto a glass substrate coated with silver film by using a focused ion beam. They have investigated the influence of the number of slits and the focusing light phenomena by capturing the light transmitted through the circular slits. They demonstrated experimentally that the circular grating formed by a set of periodical slits can excite both stronger surface plasmon (SP) and localized surface plasmon (LSP) as the number of slits increases. They found that the SP tended to congregate at the centre of the circular grating, and that the reemitted light could be used to achieve a focusing phenomenon. The phase velocity in a circular slit is related to the sum of the inner and outer radii. The circular slit will allow the light to focus after propagating in free space even if every circular slit has the same opening width. Therefore, these parameters could be changed to alter the focusing phenomenon of the circular grating. This focusing optical head is similar to a traditional optical lens, and the transmitted light will focus after propagating some distance. The intensity of the transmitted light increases as the number of circular slits increases, and the SP modes will possess propagating behavior along the metal surface in addition to possessing a focusing phenomenon. Thus, they could adopt a SP mode to design a device for nanolithography applications such that it can reduce the required exposure time due to its high transmitted energy and can provide a single point light source to write various geometrical patterns [82].

It is clear from the representative literature review presented above that a study of the optical response of nanostructured metal films is extremely important both from basic research perspective as well as applications. It is evident from a detailed literature survey that there are many issues that still need to be addressed and some of these will form the objectives of the current work.

A list of some other contributions in this field is also presented [83 - 122].

References

1. Metallic Nanomaterials, Volume 1; Volume 3, edited by Challa S. S. R. Kumar.
2. M. M Alvarez, J. T. Khoury, T. G. Schaaff, M. N. Shafigullin, I. Vezmar and R. L. Whetten, J. Phys. Chem. B, **101** (1997) 3706-3712.
3. A. Henglein, Chem. Rev. **89** (1989) 1861.
4. M. P. Pileni, A. Taleb, C. Petit, J. Dispers Sci Technol, **19** (1998) 185.
5. S. R. Emory, S. Nie, J. Phys. Chem. B, **102** (1998) 493.
6. A. Heilmann, U. Kreibig, Eur. Phys. J. Appl. Phys. **10** (2000) 193.
7. A. A. Lazarides, K. L. Kelly, T. R. Jensen, G. C. Schatz, **529** (2000) 59.
8. J. Z. Zhang, Z. L. Wang, J. Liu, S. Chen, G. Y. Liu, Self assembled nanostructures, Kluwer Academic/Plenium, New York (2003).
9. A. Aubry, D. Y. Lei, S. A. Maier and J. B. Pendry, Phys. Rev. B **82** (2010) 205109.
10. T. W. Ebbesen, H. J. Lezec, H. F. Ghaemi, T. Thio and P. A. Wolff, Nature **391** (1998) 667.
11. A. Tsiatmas, A. R. Buckingham, V. A. Fedotov, S. Wang, Y. Chen, P. A. J. de Groot and N. I. Zheludev, Appl. Phys. Lett. **97** (2010) 111106.
12. F. Wang and Y. R. Shen, Phys. Rev. Lett. **97** (2006) 206806.
13. H. A. Atwater and A. Polman, Nature Mater. **9** (2010) 205.
14. W. Cai and M. L. Brongersma, Nature Nanotechnol. **5** (2010) 485.
15. M. Jablan, H. Buljan and M. Soljacic, Phys. Rev. B **80** (2009) 245435.
16. W. L. Barnes, A. Dereux and T. W. Ebbesen, Nature (London) **424** (2003) 824.
17. S. A. Maier and H. A. Atwater, J. Appl. Phys. **98** (2005) 011101.
18. A. M Schwartzberg and J. Z. Zhang, J. Phys. Chem. C, **112** (2008) No 28.
19. Y. Takeda, O. A. Plaksin, H. Wang, K. Kono, N. Umeda and N. Kishimoto, Optical Review, **13** No. 4 (2006) 231.
20. C. Noguez, Optical Materials **27** (2005) 1204.
21. M. E. Stewart, C. R. Anderton, L. B. Thompson, J. Maria, S. K. Gray, J. A. Rogers and R. G. Nuzzo, Chem. Rev. **108** (2008) 494.
22. H. A. Atwater, Sci. Am. **296** (2007) 56.
23. E. Ozbay, Science **311** (2006) 189.
24. H. Liao, W. Lu, H. Yu, W. Wen and G. K. L. Wong, J. Opt. Soc. Am. B, **22**, No. 9 (2005).

25. E. Verhagen, M. Spasenovic, A. Polman and L. Kuipers, Phys. Rev. Lett. **102** (2009) 203904.
26. M. Moskovits, Rev. Mod. Phys. **57** (1985) 783.
27. M. Moskovits, J. Raman spectrosc. **36** (2005) 485.
28. X. M, Qian, X. H. Peng, D. O. Ansari, Q. Yin_Goen, G. Z. Chen, D. M. Shin, L. Yang, A. N. Young, M. D. Wang, S. M. Nie, Nat. Biotechnol, **26** (2008) 83.
29. Y. Wang, H. Wei, B. Li, W. Ren, S. Guo, S. Dong, E. Wang, Chem. Commun. (2007) 5220.
30. J. H. Kim, S. M. Lee, B. H. Jun, H. J. Choi, J. S. Kim, M. H. Cho, Y. K. Kim, D. H. Jeong, Y. S. Lee, Nanomed.-Nanotechnol. Biol. Med. **3** (2007) 341.
31. A. J. Bonham, G. Braun, I. Pavel, M. Moskovits, N. O. Reich, J. Am. Chem. Soc. **129** (2007) 14572.
32. S. Bernad, N. Leygue, H. Korri-Youssoufi, S. Lecomte, Eur. Biophys. J. Biophys. Lett. **36** (2007) 1039.
33. K. Kneipp, H. Kneipp, I. Itzkan, R. R. Dasari, M. S. Feld, J. Physics-Condensed Matter, **14** (2002) R597.
34. Y. Fu, J. R. Lakowicz, J. Phys. Chem. B, **110** (2006) 22557.
35. K. Ray, H. Szmacinski, J. Enderlein, J. R. Lakowicz, Appl. Phys. Lett. **90** (2007) 25116.
36. L. Malic, B. Cui, T. Veres, M. Tabrizian, Opt. Lett. **32** (2007) 3092.
37. I. C. Stancu, A. Fernandez-Gonzalez, L. M. Butac, R. Salzer, J. Optoeleltron. Adv. Mater., **9** (2007) 2696.
38. A. J. Haes, C. L. Haynes, A. D. McFarland, G. C. Schatz, R. R. Van Duyne, S. L. Zou, MRS Bull. **30** (2005) 368.
39. K. A.Willets, R. P. Van Duyne, Ann. Rev. Phys. Chem. **58** (2007) 267.
40. A. G. Brolo, P. Germain, G. Hager, J. Phys. Chem. B, **106** (2002) 5982.
41. A. Lesuffleur, L. K. S. Kumar, R. Gordon, Phys. Rev. B, **75** (2007) 045423.
42. W.Gotschy, K. Vonmetz, A. Leitner and F. R. Aussenegg, Opt. Lett. **21** (1996) 1099.
43. H. G. Craighead and G. A. Niklasson, Appl. Phys. Lett. **44** (1984) 1134.
44. W. H. Yang, J. C. Hultenn, G. C. Schatz and R. P. Van Duyne, J. Chem. Phys. **104** (1996) 4313.
45. K. Baba, Y. Ohkuma, T. Yonezawa and M Miyagi, Appl. Opt. **40** (2001) 2796.
46. G.Xu, M. Tazawa, P. Jin and S. Nakao, Appl. Phys. A **80** (2005) 1535-1540.

47. C. sonnichsen, T. Franzl, R. Wilk, G. V. Plessen and J. Feldmann, New Journal of Phy. **4** (2002) 93.1-93.8.

48. F. R. Aussenegg, A. Leitner and H. Gold, Appl. Phys. A **60** (1995) 97-101.

49. A. L. Gonzalez and C. Noguez, J. Comput. Theor. Nanosci. **4** no 2 (2007).

50. E. Hao, S. Li, R. C. Bailey, S. Zou, G. C. Schatz and J. T. Hupp, J. Phys. Chem. B**108** (2004) 1224-1229.

51. T. W. H. Oates and A. Mucklich, Nanotechnology, **16** (2005) 2606-2611.

52. H. Mertens, J. Verhoeven and A. Polman, Appl. Phys. Lett., **85** no.8 (2004) 1317.

53. I.O.Sosa, C. Noguez and R. G. Barrera, J. Phys. Chem. B,**107** (2003) 6269-6275.

54. J. Z . Zhang and C. Noguez, Plasmonics **3** (2008) 127 – 150.

55. B. Choi, H. H. Lee, S. Jin, S. Chun and S. H. Kim, Nanotechnology, **18** (2007) 075706.

56. D. D. Evanoff Jr. and G. Chumanov, Chem. Phys. Chem. **6** (2005) 1221-1231.

57. R. Gupta, M. J. Dyer and W. A. Weimer, J. Appl. Phys. **92** No.9 (2002) 5264.

58. D.F.P.Pile, T. Ogawa, D. K. Gramotnev, Y. Matsuzaki, K. C. Vernon, K. Yamaguchi, T. Okamoto, M. Haraguchi and M. Fukui, Appl. Phys. Lett., **87** (2005) 261114.

59. P. Chaturvedi, W. Wu, V. J. Logeeswaran, Z. Yu, M. Saif Islam, S. Y .Wang, R. S. Williams and N. X. Fang, Appl. Phys. Lett., **96** (2010) 043102.

60. T.W.H. Oates, L. Ryves, M. M. M. Bilek and D. R. McKenzie, Sensors and Actuators B **109** (2005) 146-152.

61. C. Farcau and S. Astilean, Appl. Phys. Lett., **95** (2009) 193110.

62. X.Yang and L. Wang, Optics Communications, **280** (2007) 368-373.

63. A. Politano, V. Formose and G. Chiarello, Applied Surface Science, **255** (2009) 6038-6042.

64. J. Tominaga, J. Phys.: Condens. Matter, **15** (2003) R1101-R1122.

65. S. H. Choi, S. J. Kim and K. M. Byun, Optics Communications, **283** (2010) 2961-2966.

66. G.Vasilyuk, S. Maskevich and S. Podtynchenko, Journal of Molecular Structure, **565-566** (2001) 389-394.

67. Y. Ye, Y. Jiag, M. Tsai, Y. Chang, C. Chen, D. Tzuang, Y. Wu and S. Lee, Appl. Phys. Lett., **93** (2008) 263106.

68. N. Perea-Lopez, N. Rakov and M. Xiao, Rev. Sci. Instum., **73** (2002) 4399.

69. J. Zhao, R. Tian and J. Zhi, Thin Solid Films, **516** (2008) 4047-4052.

70. P.D. Codble, A. Mitra, R. Pasricha, A. B. Mandale and K. R. Patil, Materials Letters, **59** (2005) 1958-1961.
71. M. Tsai. T. Chuang, H. Chang and S. Lee, Appl. Phys. Lett., **89** (2006) 093102.
72. H. M . Benia, N. Nilius and H. J. Freund, Surface Science, **600** (2006) L128-L133.
73. I. Cryczynski, J. Malicka, K. Nowaczyk, Z. Gryczynski and J. R. Lakowicz, J. Phys. Chem. B, **108** (2004) 12073-12083.
74. L. A. Kuzik and V. A. Yakovlev, Thin Solid Films, **340** (1999) 288-2911.
75. A. I. Maaroof and G. B. Smith, Thin Solid Films, **485** (2005) 198-206.
76. A. Altube, Al Blanco and C. Lopez, Materials Letters, **62** (2008) 2677-2680.
77. A. Subrahmanyanm and U. K. Barik, Journal of Physics and Chemistry of Solids, **67** (2006) 1518-1523.
78. A. J. de Vries, E. S. Kooij, H. Wormeester, A. A. Mewe and B. Poelsema, J. Appl. Phys. **101** (2007) 053703.
79. G. Winter and W. L. Barnes, Appl. Phys. Lett., **88** (2006) 051109.
80. D.A. Bobb, G. Zhu, M. Mayy, A. V. Gavrilenko, P. Mead, V. I. Gavrilenko and M. A. Noginov, Appl. Phys. Lett.,**95** (2009) 151102.
81. A. Ghoshal and P. G. Kik, Appl. Phys. Lett., **94** (2009) 251102.
82. C. Chang, D. Lin, C. Yeh, C. Lee, Y. Chang, M. Lin, J. Yeh and J. Liu, Appl. Phys. Lett., **90** (2007) 061113.
83. R. Wannemacher, Optics Communications **195** (2001) 107.
84. M. Dragoman and D. Dragoman, Progress in Quantum Electronics, **32** (2008) 1-41.
85. M. G. Blaber, M. D. Arnold, N. Harris, M. J. Ford and M. B. Cortie, Physica B **394** (2007) 184.
86. A. Bouhelier, Th. Huser, H. Tamaru, H. J. Guntherodt, D. W. Pohl, F. I. Baida and D. V. Labeke, Phys. Rev. B **63** (2001) 155404.
87. Y. Suzuki, Y. Ojima, Y. Fukui, H. Fazyia and K. Sagisaka, Thin Solid Films **515** (2007) 3073.
88. H. Jia, J. Zeng, W. Song, J. An and B. Zhao, Thin Solid Films **496** (2006) 281.
89. M. Sukharev, P. R. Sievert, T. Seideman and J. B. Ketterson, J. Chem. Phys.**131** (2009) 034708.
90. K. Mallick, M. J. Witchomb, M. S. Scurrell, Materials Science and Engineering C **26** (2006) 87.
91. G. Webb-Wood and P. G. Kik, Appl. Phys. Lett. **92** (2008) 133101.
92. S. Owega, D. Poitras and K. Faid, Sensors and Actuators B **114** (2006) 212.

93. V. Vlasko-Vlasov, A. Rydh, J. Pearson and U. Welp, Appl. Phys. Lett. **88** (2006) 173112.

94. X. Yin, C Huang, Z. Shen, Q. Wang and Y. Zhu, Appl. Phys. Lett. **94** (2009) 1611904.

95. S. Wedge and W. L. Barnes, Optics Express, **12** No. 16 (2004) 3673.

96. S. K. Lim, K. J. Chung, C. K. Kim, D. W. Shin, Y. H. Kim and C. S. Yoon, J. Appl. Phys. **98** (2005) 084309.

97. I. Avrutsky, Y. Zhao and V. Kochergin, Optics Letters, **25** No. 9 (2000) 595.

98. A. E. Kryukov, Y. K. Kim and J. B. Ketterson, J. Appl. Phys. **82** (1997) 5411.

99. X. Sun, R. Hong, H. Hou, Z Fan and J. Shao, Thin Solid Films **515** (2007) 6962.

100. A. Giannattasio, I. R. Hooper and W. L. Barnes, Optics Express, **12** No. 24 (2004) 5881.

101. M. H. Chowdhury, K. Ray, C. D. Geddes, J. R. Lakowicz, Chemical Physics Letters **452** (2008) 162.

102. M. Csete, A. Kohazi-Kis, C. Vass, A. Sipos, G. Szekeres, M. Deli, K. Osvay and Z. Bor, Applied Surface Science **253** (2007) 7662.

103. A. Stefanie, P. J. Cameron, J. Liu, W. Knoll, J. Erlebacher and F. Yu, Plasmonics **3** (2008) 13.

104. F. Caruso, M. J. Jory, G. W. Bradberry, J. R. Sambles and D. N. Furlong, J. Appl. Phys. **83** (1998) 1023.

105. Y. Yang, M. Tanemura, Z. Huang, D. Jiang, Z. Li, Y. Huang, G. Kawamura, K. Yamaguchi and M. Nogami, Nanotechnology **21** (2010) 325701.

106. G. Bader, A. Hache and V. Truong, Thin Solid Films **375** (2000) 73.

107. I. M. Arabatzis, T. Stergiopoulos, D. Andreeva, S. Kitova, S. G. Neophytides and P. Falaras, Journal of Catalysis **220** (2003) 127.

108. B. A. Sexton, B. N. Feltis and T. J. Davis, Sensors and Actuators A 141 (2008) 471.

109. B. Steinberger, A. Hohenau, H. Ditlbacher, A. L. Stepanov, A. Drezet, F. R. Aussenegg, A. Leitner and J. R. Krenn, Appl. Phys. Lett. 88 (2006) 094104.

110. A. Hoffmann, Z. Lenkefi and Z. Szentirmay, J. Phys.: Condens. Matter **10** (1998) 5503.

111. M. M. Dvoynenko, A. V. Goncharenko, V. R. Romaniuk and E. F. Venger, Physica B **299** (2001) 88.

112. Y. Chang, Y. Wu, J. Lee, H. Chen, C. Hsueh, H. Huang, Y. Jiang, P. Chang and S. Lee, Appl. Phys. Lett. **95** (2009) 213102.

113. S. Szunerits, V. G. Praig, M. Manesse and R. Boukherroub, Nanotechnology **19** (2008) 195712.

114. M. Baia, L. Baia ands. Astilean, Chemical Physics Letters **404** (2005) 3.

115. K. Seal, M. A. Nelson, Z. C. Ying, D. A. Genov, A. K. Sarychev and V. M Shalaev, Phys. Rev. B **67** (2003) 035318.

116. S. Buil, J. Aubineau, J. Laverdant and X. Quelin, J. Appl. Phys. **100** (2006) 063530.

117. S. Cho, S. Lee, T. S. Lee, B. Cheong. W. M. Kim and K. Lee, J. Appl. Phys. **102**, (2007) 123501.

118. G. R. Yashan, A. M. Eremenko, N. P. Smirnova, S. Suzer, G Ertas and Ch. Tabor, Theoretical and Experimental Chemistry, **44** No. 6 (2008) 356.

119. X. Ren, X. Meng and F. Tang, Sensors and Actuators B **110** (2005) 358.

120. Y. B. Zheng, T. J. Huang, A. Y. Desai, S. J. Wang, L. K. Tan, H. Gao and A. C. H. Huan, Appl. Phys. Lett. **90** (2007) 183117.

121. P. C. Lansaker, J. Backholm, G. A. Niklasson and C. G. Granqvist, Thin Solid Films, **518** (2009) 1225.

122. M. Torrell, L. Cunha, A. Cavaleiro, E. Alves, N. P. Barradas and F. Vaz, Applied Surface Science **256** (2010) 6536.

Chapter II: Experimental and Characterization techniques

Abstract

This chapter describes the different fabrication and characterization techniques used in the present work. In the present work, IBSD was used to deposit Ag and Au thin films on Quartz, Borosilicate glass and carbon coated Cu grids substrate and also on sol-gel deposited TiO_2 and ZrO_2 thin films. The deposited films were characterized using atomic force, scanning electron and transmission electron microscopy, UV-Vis-NIR spectrophotometry and x-ray diffraction. The details of experimental conditions and characterization techniques are presented here.

Chapter II: Experimental Techniques

2.1. Ion Beam Sputter Deposition

The surface atoms of a solid can be sputtered by exposing them to a beam of energetic particles of energy between 0.1 to 5 KeV. If the sputtered atoms are deposited on a substrate, then the process is called Ion Beam Sputter Deposition (IBSD). The overall amount of deposited energy (and therefore the number of sputtered atoms) is sensitive to the surface. The use of ion beams for processing, as opposed to directly extracting ions from plasma to bombard a sample, has numerous advantages for the controlled processing of materials with ion bombardment. The parameters of ion beam, the flux, the energy, the species and charge state and the direction (and divergence) are all easily quantified and controlled. IBSD typically operates in the pressure range of 1 x 10^{-5} Torr to 1 x 10^{-3} Torr, which makes it compatible with a number of other physical and chemical processes used in thin film material processing. This is not possible in other plasma based sputtering techniques which work at much higher pressures. One other significant advantage to operation in this relatively low pressure region is that the mean free paths of both the incident ions and also of the sputtered atoms are long. There is little scattering due to gas phase collisions and as such the complication of charge exchange modification of the ion flux is minor.

Many researchers have worked on ion beam deposition techniques for many different applications. A brief review of literature on IBSD is presented. Todorov *et al.* have deposited monolayer thick silver films on an Ni(100) surface using direct ion beam deposition of ^{107}Ag+ ions with 20 eV kinetic energy and the substrate at 25°C. The film deposition was performed by means of a mass-selected, low energy, ultra-high vacuum ion beam system with a well-defined ion energy. The films were analyzed in situ by time of- flight scattering and recoiling spectrometry (TOF-SARS) and by low energy electron diffraction (LEED). They have used classical ion trajectory simulations to model the TOF-SARS spectra. It is found that the results of the TOF-SARS spectra and azimuthal scans are consistent with the growth of a monolayer Ag film with a fcc (111) structure on the Ni(100) surface. The deposited films exhibited a faint hexagonal c(2×8) LEED pattern. It is observed that molecular dynamic simulations of the deposition process are in

agreement with the experimental observations. The growth of such isotopically pure metal monolayers at room temperature with controlled orientations provides the opportunity for exploring a variety of unique physical properties [1]. Nguyen *et al.* have developed high-reflection (HR) and multilayer antireflection (AR) coatings using ion-beam sputtering deposition (IBSD) for long-wave infrared (LWIR) ($\lambda \sim 9.4$ μm) quantum cascade lasers (QCL). The high quality, high-density material achieved by IBSD allows for flexible and robust optical coatings especially compared to electron beam evaporation (EBE). It was observed that similar to the engineering of the QCL emission wavelength, both AR and HR coating structures can be customized, by slight adjustment of the layer thicknesses, for other lasers emitting at any wavelength in the LWIR. The metallic HR coating achieved a measured reflectance of 96.70%, and the multilayer AR coating achieved a measured reflectance of 1.64%, within 3% of theoretical simulation. They have provided a solution to the processing sequence due to problems that arise from the high-temperature deposition process. Finally, the coatings were applied to a $\lambda \sim 9.4$ μm QCL [2]. Liu *et al.* have used Time–power monitoring technique for monitoring the thickness of optical films during ion beam sputter deposition with the routine parameters of the main ion source are 1200 V/ 300 mA for Ta_2O_5 and 1000 V/500 mA for SiO_2 respectively. They baked the vacuum chamber at 80^0C for 2 h and the baking is stopped during the coating process. In the beginning stage of sputtering, it was observed that the change of composition and microstructure in the top layer of targets results in the change of the sputter rate. For different materials, their sputter characteristics are different. With the increase of the layer number, the deposition rate for Ta_2O_5 increases, while the deposition rate for SiO_2 decreases, and both deposition rates eventually stabilize. It has been shown that the results of a single layer coating were in fairly good agreement with those of multilayer coatings. The results show that the film thickness can be controlled accurately by adjusting the deposition time at the beginning of deposition. This paper has also provided a simple and effective way to optimize the thickness match of the high- and the low-index layers for a multilayer stack [3]. Balu *et al.* have deposited chromium films by IBSD technique with varied process parameters. The ion energy in this case was 1 KeV with an incident angle of 45^0 at different fluxes. The energetics involved in the process has been observed as the important criteria that influence the structural evolution. Deposition rate has been found to play a major role in the initial structure formation indicating the necessity of a critical deposition rate. It has been observed that (1 1 0) orientation sustains even at higher substrate temperatures as high as 700^0C. The structural

transformation of (1 1 0) to (2 0 0) orientation occurs when the process parameters favor the formation of island growth, which was carried out using oblique incidence technique. With higher angle of incidence, the film shows (2 0 0) preferential orientation, which is considered to be the plane of better lattice match to Co-based alloys. The surface morphology shows a ripple nature with comparatively lower surface roughness. From the above investigations, it is clear that the energetics of the process controlled by various factors, such as deposition rate, substrate temperature and film thickness associated with oblique incidence, plays the major role in the structural transformation from (1 1 0) to (2 0 0) orientation in Cr thin films [4]. Huang *et al.* have deposited Silicon nitride films on Al/glass, NaCl, KBr, and silicon substrates by single ion beam sputter deposition. They prepared the films at various N_2^+ ion beam voltages over the range from 500 to 1200 V. The resulting films were characterized by using secondary ion mass spectrometry, Fourier transform infrared spectroscopy, transmission electron microscopy, and transmission electron diffraction. The stoichiometry of these silicon nitride films was controlled by adjusting the ion beam voltage. It was observed that the films deposited under conditions of ion beam voltage below about 700 V were nitrogen rich while films made with beam voltages in excess of 900 V were silicon rich. The film structure changed with the substrate temperature from amorphous at room temperature to nanocrystalline/amorphous at 300^0C. The lowest occupied (LO) phonon band for stoichiometric Si_3N_4 was approximately 1124 cm^{-1} and the stoichiometry of thin silicon nitride films could be assessed with the LO phonon position [5]. Lim *et al.* have reported on Cu films deposited by ion beam deposition with or without a negative substrate bias voltage were found to have different states of dependence of electrical resistivity on film thickness. Here, a/Cu-enriched plasma was generated by an application of a negative bias voltage of -300 V to the Cu target. In this report, they have attempted to evaluate the effects of the film thickness, average grain size, impurities, and morphological defect on the resistivity increase of Cu films in addition to the surface scattering of the Fuch-Sondheimer model and the grain boundary scattering of the Mayadas-Shatzkes model. When the theoretical model was fit to the experimental data, the Cu films deposited at a substrate bias voltage of −50 V showed that the electrical resistivity was in good agreement with the theoretical curve under the condition that the film thickness was 2.3 times larger than the average grain size and when p=0 and R=0.24. For the Cu films deposited without a substrate bias voltage, however, there was a slight deviation between the theoretical curve and the measured resistivity below a 100 nm thickness, even at the condition of the film thickness

that was six times larger than the average grain size, which is considered to result from the effect of solute impurities in the Cu films. Therefore, it was found that the impurity effect on the electrical resistivity could not be neglected. It was also confirmed that the morphological defect, such as a columnar structure with noticeable gaps in the Cu films deposited without the substrate bias voltage, caused a great increase in resistivity even above the 100 nm thickness [6]. Sasase *et al.* have deposited 'Environmentally friendly' semiconductor β-$FeSi_2$ thin films by the ion beam sputter deposition (IBSD) method on Si(100) substrate. The authors used Ar^+ ion energy of 35 KeV and Ar^+ ion current density of 250 μA/cm^2. The difference in crystallinity of the $FeSi_2$ obtained has been investigated using Fe and Fe–Si targets at various substrate temperatures. When the Fe target was used, highly (100)-oriented β-FeSi2 films with relatively smooth surfaces were formed at 700^{o}C. On the other hand, such films were scarcely observed when the Fe–Si target was used. Sharp edge grains were observed, which consisted of a mixture of α and β phases or α single phase. In the latter case, it is found that α-FeSi2 is formed at T_s above 600^{0}C, which is lower than the conventional transformation temperature for the β → α phase [7]. Nitti *et al.* have used the ion-sputtering technique with Ar ions of energies 350 and 700 eV, with a fixed ion current of 50 mA to deposit CsI thin films having a target stoichiometry not affected by the ion energy of the sputtering gas. It was observed that the film composition and growth rate were tunable with the experimental conditions. In particular, the analytical results of the morphological and structural properties of the films, in comparison to those of evaporated films confirmed the capacity of the ion beam technique to control and improve these properties. The comparative analysis of all film properties suggests that the different surface morphology of sputtered films with respect to evaporated films can be assumed as the main cause of the lower QE of sputtered CsI films. The more compact surface texture of sputtered films can determine a lower illuminated and photoemissive effective surface area [8]. Gallasch *et al.* have deposited V_2O_5 thin films by means of dc-ion beam sputtering deposition technique. The films were grown by means of accelerating the ions at acceleration voltage of 600 V towards the target. The samples were characterized by X-ray diffractometry and transmission electron microscopy to determine the influence of various deposition parameters. Using electron energy loss spectroscopy, the oxidation state of vanadium was quantified based on the chemical shift of absorption edges. It is observed that measurement of in-plane direct current showed the electronic conductivity varies over several orders of magnitude depending on the preparation conditions. The desired structure suitable for battery

applications was achieved by sputtering under partial pressure of oxygen and suitable post-annealing under ambient atmosphere and they also demonstrated the reversible intercalation of Li into the produced thin films [9]. Ronning *et al.* have grown boron carbide (B_xC) thin films via direct ion beam deposition using mass selected $^{11}B^+$ and $^{12}C^+$ ions. The films were deposited on silicon and ITO-coated quartz glass substrates with an ion energy of 100 eV at room temperature. The B^+:C^+ ion ratio during deposition was varied between 0:1 (pure carbon) and 1:0 (pure boron), and the resulting composition of the films matched this ratio, as observed by X-ray photoelectron spectroscopy (XPS). A detailed analysis of the XPS-spectra revealed that the deposited films undergo a transition from sp^3-bonded diamond-like carbon to a boron carbide phase with a lower density with increasing B concentration. The formation of carbide bonds has been observed by means of XPS, and the valence band spectra showed a strong transition from the amorphous semiconductor ta-C to metallic boron. This transition was also observed by optical and electrical measurements [10]. Shimura *et al.* have reported photoluminescence (PL) from β-FeSi2 thin film grown by ion beam sputter deposition (IBSD) method. For the first time, they observed several small PL peaks in the as-grown IBSD films at around 0.77 and 0.83 eV below 100 K. By thermal annealing at 1153 K for more than 24 h, these films showed a strong peak at around 0.81 eV with increased intensity by more than an order of magnitude at 6 K. These annealed samples showed luminescence up to room temperature, while no PL was observed above 100 K for the as-grown films [11]. Ichinohe *et al.* have fabricated a light emitting Si-doped glass (Si-DG) film using ion beam sputter-deposition (IBSD) technique. They have used Ar ions of energy 1 KeV, and the ion current density was adjusted to 0.5 mA cm^2. It is observed that the photoluminescence (PL) intensity increased with increasing annealing temperature up to approximately 900^{o}C but it often decreased above the critical temperature. According to the high-resolution transmission electron microscope (TEM) observations, Si crystallites with a diameter of approximately 3 nm were found in the film after the heat treatment, indicating that the formation of Si crystallites is closely related to the luminescence intensity. The luminescent Si-DG film showed extremely broad PL spectra and the full width at half-maximum (FWHM) typically being approximately 1 eV. To obtain a much sharper bandwidth for light emission, the Si-DG film was sandwiched by a metal (Ag) film and a dielectric multilayered reflector. The FWHM value of the PL spectrum was reduced to approximately 0.1 eV after fabricating the resonator using a 20-paired CeO_2/Si-DG multilayered reflector [12]. Tam *et al.* have fabricated binary component Ni–

Si films of different compositions on AISI 304L stainless steels by means of ion-beam sputter (IBS) deposition. In this study, they have co-sputtered commercial purity nickel (Ni) (>99.9%) metal disc and silicon (Si) (100) wafer targets by means of low energy argon ion beams (≤500 eV) generated simultaneously from two Kaufman type ion source. They have analyzed the compositions of the thin films and the chemical states by means of X-ray photoelectron spectroscopy (XPS) and the phase formation is studied and discussed in view of Pretorius' effective heat of formation (EHF) model. The chemical state analyses were carried out by fitting the core level spectra of Ni $2p_{3/2}$ and Si 2p peaks with an asymmetry Gaussian–Lorentzian sum function. They observed that chemical state analyses from the XPS curve-fittings agree well with the compound predictions using the Pretorius's EHF model. The valence band spectra from the Ni–Si film series samples show that the bonding changes from predominantly metallic to covalent bonding as the Si content increases. This could also be concluded from the corresponding Ni $2p_{3/2}$ and Si 2p core level spectra through the assessment and study of FWHM values and peak symmetry parameters. For the very short-range ordered structure in the Ni–Si thin films, the line broadening effect and limited film thickness (~100 nm) make it impossible to ascertain the structure of the Ni–Si films by means of GIXRD [13]. Ensinger *et al.* have deposited alumina and tungsten carbide powder with gold and platinum by ion beam sputter deposition (IBSD). For the uniform deposition, the powder grains were agitated in a rotating conical vessel. It contained a sputter target which was irradiated by a beam of rare gas ions of energy 60 keV maintaining the ion currents onto the sputter target ranged from 30 to 100 μA. Metal atoms sputtered from the target were deposited onto the powders. The amount of deposited noble metals was determined by means of atomic absorption spectrometry. It increased monotonically with the sputter ion fluenc. Under the given conditions, up to 0.3 wt.% gold were deposited onto alumina, while tungsten carbide received up to 0.016 wt.% platinum. While alumina remained non-conductive, the electrical conductivity of tungsten carbide was found to increase up to a factor 4 by platinum deposition. Electrochemical measurements showed that the electrochemical activity of tungsten carbide was considerably enhanced by platinum deposition and they claim that this material may be used as an electrocatalyst [14]. Kojima *et al.* deposited SiO_2/Ta_2O_5 multilayers on Si(100) by ion-beam sputter deposition. In this case, the used ion energy was from 50-1200 eV. They have characterized the layer thickness and interfacial roughness of the multilayers by using a grazing incidence x-ray reflectivity technique. In particular, the differences in structural features between the Ta_2O_5 on SiO_2

interface and the SiO_2 on Ta_2O_5 interface, as well as the possible inhomogeneity of the SiO_2 layers, were successfully revealed. It is observed that the x-ray reflectivity results are consistent with the high-resolution electron microscopy observations [15]. Mahendra Kumar *et al.* have reported on the pure amorphous silicon thin films deposited by ion beam sputter deposition onto borosilicate glass substrates at ambient temperature by using Ar ion energy of 600 eV. They derived the optical constants from spectral transmittance measurements in the range of 350-2500 nm. It is observed that all the samples, regardless of thickness, show a Raman peak centered between 460 and 480 cm^{-1}. The root-mean-square variation in the bond angles, $\Delta\theta$, obtained from Raman spectra, indicates the presence of relatively good short range order in amorphous silicon thin films. It if found that the refractive index at 1.4 eV decreases from 4.35 to 3.52 with an increase in thickness from 30 to 130 nm. The band gap varies with thickness and at a thickness of 130 nm the band gap is found to be 1.3 eV, which increases to 1.8 eV at 30 nm. The narrow band gap values of ion beam sputtered a-Si thin films indicate that they can be explored for photovoltaic applications [16].

It is evident from the review of literature that IBSD is a very effective technique to provide a large variety of thin films with enhanced properties. Majority of the work focuses on the use of Ar ions of energies >500 eV. There is very limited work on investigations of growth of films at energies <500 eV. The focus of current work is, therefore, to investigate growth of films at Ar ion energies << 500 eV.

2.2. Parameters used for IBSD in this study

Ion beam sputter deposition is an effective approach for creating or enhancing strong, stable, uniform and direct adhesion of thin films deposited on substrates which is very useful for applications. The ion beam sputter deposition system used in this work is home built and consists of a Kaufman type DC ion source (of Oxford Applied Research, Model DC25, 100 – 1500 eV model). This ion beam is capable of producing ion beams of 2.5 cm in diameter. The main reason of using such a low energy ion beam sputtering is to obtain self ordered nanostructured thin films. Figure 2.1(a) shows the schematic diagram of ion beam sputter deposition system used in the current work.

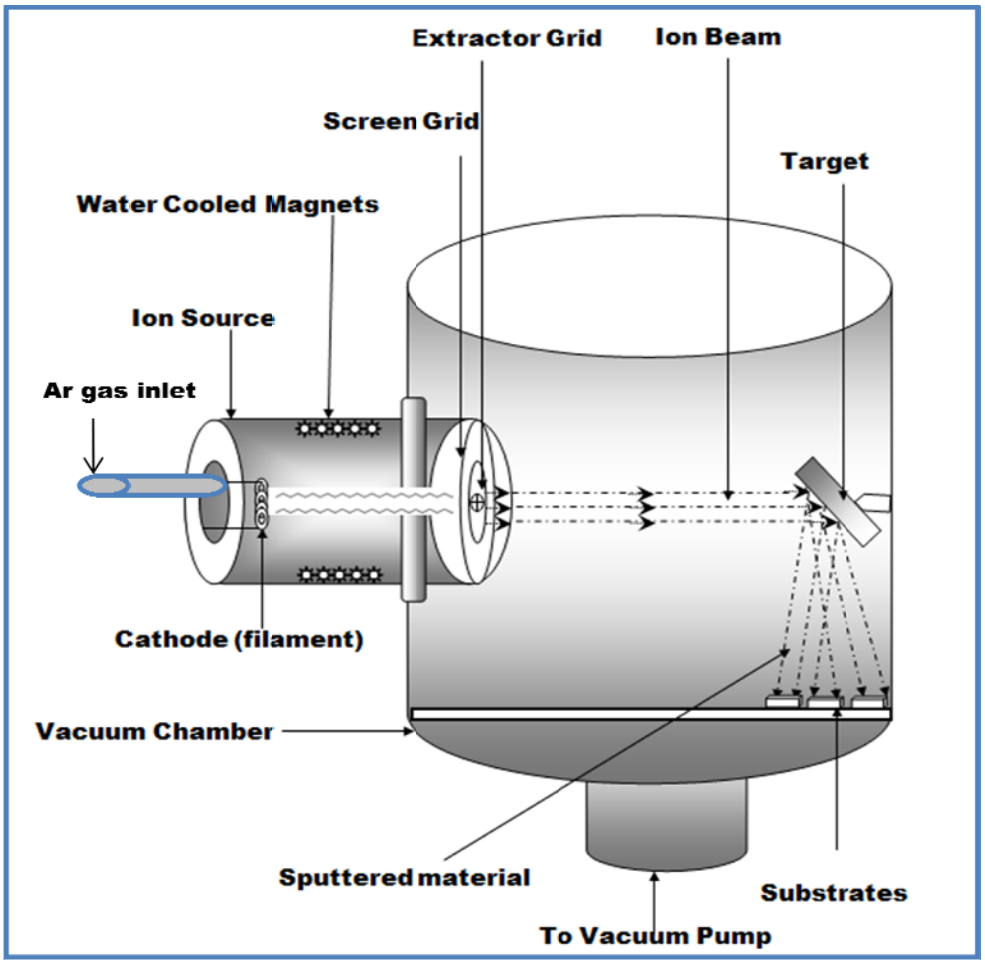

Figure 2.1(a). Schematic diagram of ion beam sputter deposition system.

The ion source consists of cylindrical type chamber (anode) where cathode (tungsten filament) is mounted and surrounded by magnet and water cooled chamber which is attached to two grids (called screen grid and extractor grid). Ar gas is passed through the ion source itself. When current is applied to the filament, it emits electron and the emitted electron collide with the Ar gas which is ionized. The direction of magnetic field causes the emitted electrons to move in helical path so that they collide with more Ar gas increasing the ionization process. Ions are then extracted by the extractor grid and accelerated towards the target. They bombard the target and sputter the material. The screen grid screens the electron from coming out of the ion source. Photographic images of the system are shown in figs. 2.1 (b) to (e).

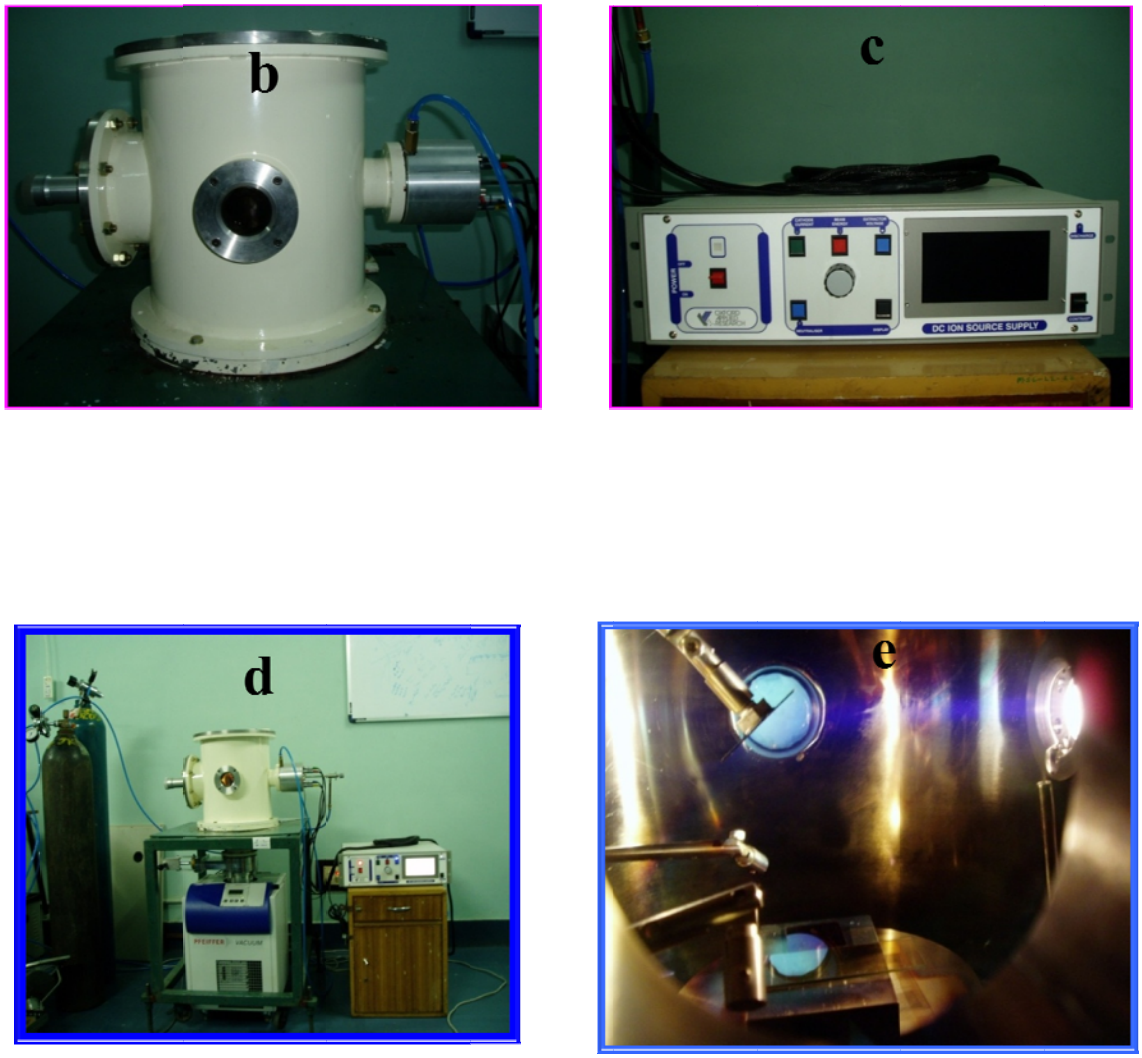

Fig.2.1. (b) View of the 16 inch dia UHV chamber with capability to sputter 3 targets without breaking vacuum (c) Kaufman type ion source (DC25 of Oxford Applied Research, UK) (d) Full view of ion beam sputter deposition coating unit and (e) the inner view of the chamber during sputter deposition.

Ion beam sputter deposition has many advantages over other physical vapor deposition techniques like thermal evaporation and normal glow discharge sputtering. Some of the advantages are listed below:

Ion beam sputter deposition	**Glow discharge system**	**Thermal evaporation**
Can sputter at high vacuum like 10^{-4} to 10^{-5} Torr.	Sputtering takes place at pressure > 10^{-3} Torr.	Can evaporate at 10^{-5} Torr or lower pressure.
Can sputter metals and insulator.	Can not sputter insulator unless RF is used.	Can evaporate metals and insulator but stoichiometry is a problem.
There is no contamination in the film as the Ar gas is passed in the ion source itself and ions are extracted.	Ar gas is filled in the chamber so there will be scattering and contamination.	Contamination due to reaction between evaporant and heat source (such as W, Ta or Mo boat).
Has independent control on energy, current density and angle of incidence of ions.	No independent control possible.	Energy and flux is related to source temperature, angle of incidence can be controlled.

In the present work, the Ag and Au films were deposited with the following conditions:

Pumping unit : Rotary + turbo pump

Base pressure : 2 x 10^{-6} Torr

While sputtering : 4.5 x 10^{-4} Torr

Ion source to target distance : 15 cm

Target to substrate distance : 14 cm

Substrate temperature : RT to 300^{0}C.

Ion energy : 150, 200, 250, 300, 400 and 600 eV

Ion current : 0.2 A.

Extractor voltage : - 40 V.

Substrates: Boro silicate glass substrates and fused silica.

2.3. Characterization Techniques

2.3.1. Thickness measurement

The thickness of the samples was measured using stylus profiler (also known as profilometer) (Model XP-1, Ambios Technology, USA). Surface profilometry is a direct, simple and fast measurement technique for determining the physical thickness of thin films [17]. The only requirement is the existence of a step as shown in figure 2.2. In this study, the step was made by covering a part of the substrate using a thin stainless steel shadow mask during deposition. This method involves loading a stylus (generally a diamond stylus) slightly in contact with the film surface and gently dragging it across the step as shown in figure 2.2. The vertical deflection measures the change in step height (film thickness) and the trace is recorded with high accuracy.

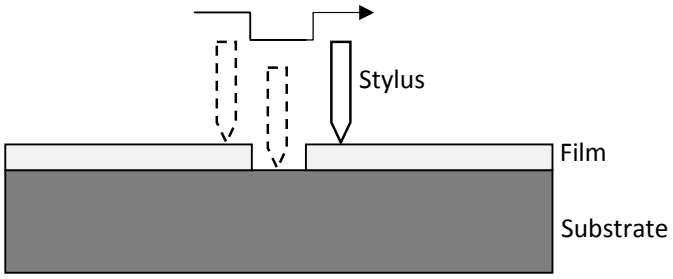

Figure 2.2. Illustration of stylus profillometry to measure film thickness.

2. 3.2. X-Ray diffraction

X-ray diffraction is a well-known technique for characterizing the crystal structure of materials. X-rays have a wavelength of the order of Angstroms (10^{-10} m), which is comparable to the inter-atomic spacing in crystalline solids. Therefore, a diffraction pattern can be observed when a beam of x-rays is directed on a crystalline material (where the atoms are arranged periodically). This diffraction pattern is directly related to the crystal structure of the material under observation. The diffraction of x-rays by a crystalline material is illustrated in figure 2.3.

In the present work, two types of X-ray diffractometers with different x-ray source were used to characterize the samples. One was equipped with Co Kα (λ=1.7889Å) radiation in a wide angled powder X-ray diffractometer (INEL Model CPS120) and a position

sensitive detector while the other one was a conventional X-ray diffractometer operating in the Bragg-Brentano geometry with Cu K_α (λ=1.54056 Å) radiation (Philips PW 1830 diffractometer). Calibration using a Si standard was done to account for the instrumental line broadening and the value was approximately 0.05^0 for the former and 0.10 for the later. The patterns were compared with standard patterns (JCPDS) and the phases and degree of crystallinity was determined. A slow scanning rate of 0.5°/min was used to extract data for the measurement of crystallite size. These results gave important information regarding the variation in the crystalline orientation of films lattice constants, crystallite size, strain etc. as a function of processing conditions.

2.3.2.1. Calculation of crystallite sizes from x-ray diffraction patterns

***Bragg's Law*:**

In figure 2.3 below, consider rays 1 and 1a in the incident beam. They strike atoms K and P in the first plane of atoms and are scattered in all directions. Only in the directions 1' and 1a', the scattered beams are completely in phase (because QK – PR = PK Cos θ - PK Cos θ = 0) and are capable of reinforcing one another.

This relationship is true of all the planes separately, and we have to find the condition for reinforcement of rays scattered by atoms in different planes. Let us take rays 1 and 2 scattered by atoms K and L, and the path difference for rays 1K1' and 2L2' is

$$ML + LN = d\sin\theta + d\sin\theta \qquad (2.1)$$

If this path difference is equal to a whole number n of wavelengths,

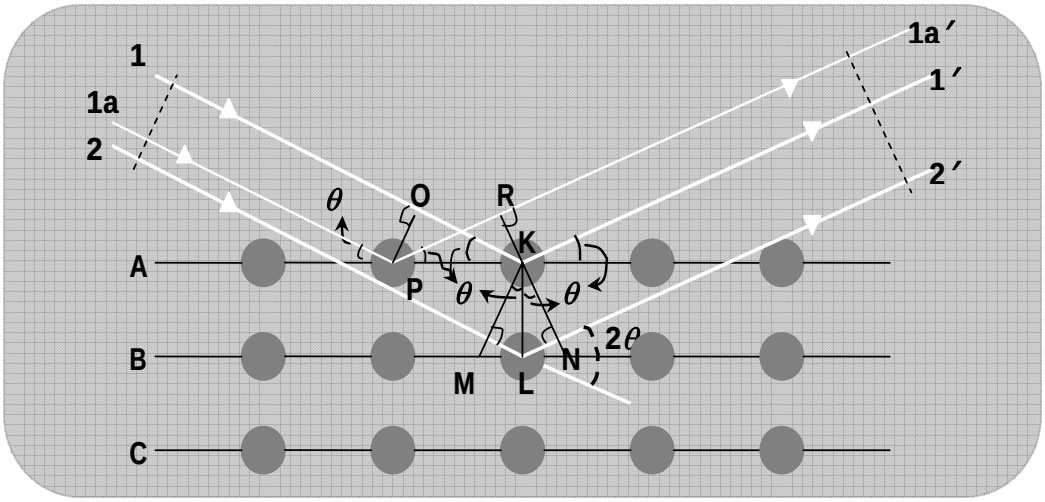

Figure 2.3. Diffraction of X -rays by periodically arranged atoms in a crystalline material.

$$n\lambda = 2d \sin\theta \qquad (2.2)$$

where, θ is the diffraction angle, λ is wavelength of the X-ray and n is the order of reflection, which may take any integral value consistent with sinθ but not exceeding unity.

This relation was first formulated by W. L. Bragg and is known as the Bragg law [18]

$$\frac{n\lambda}{2d} = \sin\theta < 1 \qquad (2.3)$$

i.e., nλ must be less than 2d. For n =1 the condition for diffraction at any observable angle 2θ is λ < 2d.

For most sets of crystal planes d is of the order of 3 Å or less, which means that λ cannot exceed about 6 Å.

Scherrer's formula is used to estimate the crystallite size, *t* given by,

$$t = \frac{0.93\lambda}{\beta \cos\theta_{\beta}} \qquad (2.4)$$

$$\beta = \frac{1}{2}(2\theta_1 - 2\theta_2)$$

where, β is angular width, in terms of 2θ and is measured in radian at an intensity equal to half the maximum intensity and is called full width at half maximum (FWHM) (shown in figure 2.4 below)

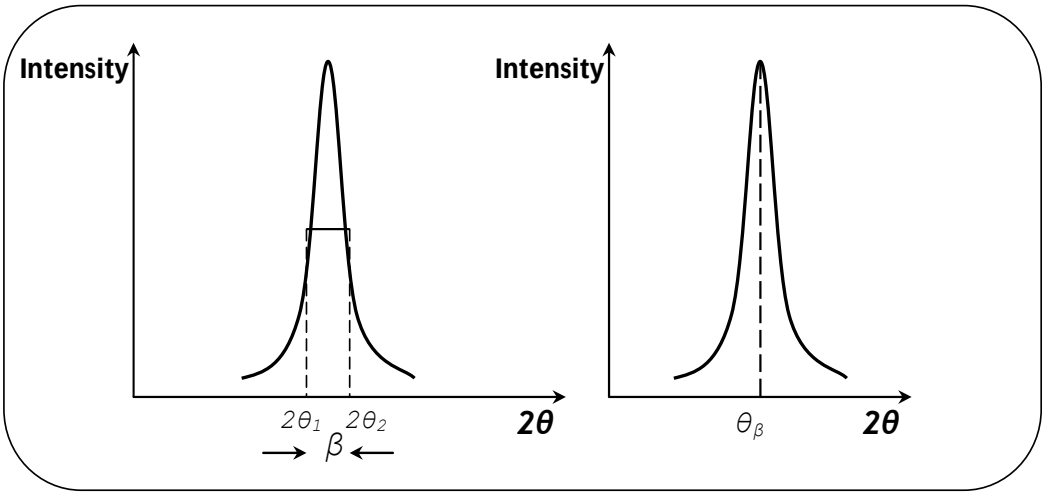

Figure 2.4. The FWHM of a x-ray diffraction peak.

2.3.3. Scanning Electron Microscopy (SEM)

SEM is a widely used technique to study surface topography of the samples. A schematic diagram of SEM is shown in figure 2.5. SEM consists of an electron source, a series of lens system which produces a finely focused beam on the specimen surfaces, two pairs of deflection coils (scanning coils) at right angles to each other, connected to a saw-tooth wave generator system, so that the finely focused electron beam can be rastered on the sample surface. The secondary electrons are gathered in a collector, amplified and fed to a cathode-ray display tube or a computer.

A high energy (typically 10-30 keV) electron beam, thermionically emitted from a tungsten filament is focused to a spot size of 1 nm to 5 nm by the condenser lenses. The focused beam passes through a pair of scanning coils, which raster the beam across the surface. The incident electrons cause low energy secondary electrons generation. The secondary electrons emitted from the sample are detected by a scintillator-photomultiplier device and the resulting signal is rendered into a two-dimensional intensity distribution that can be viewed and saved as a digital image. The most common imaging mode monitors low energy (<50 eV) secondary electrons which originates within a few nanometers from the surface. In the current work we have used Carl Zeiss Model FEG-Scanning Electron Microscope (Model Ultra 55).

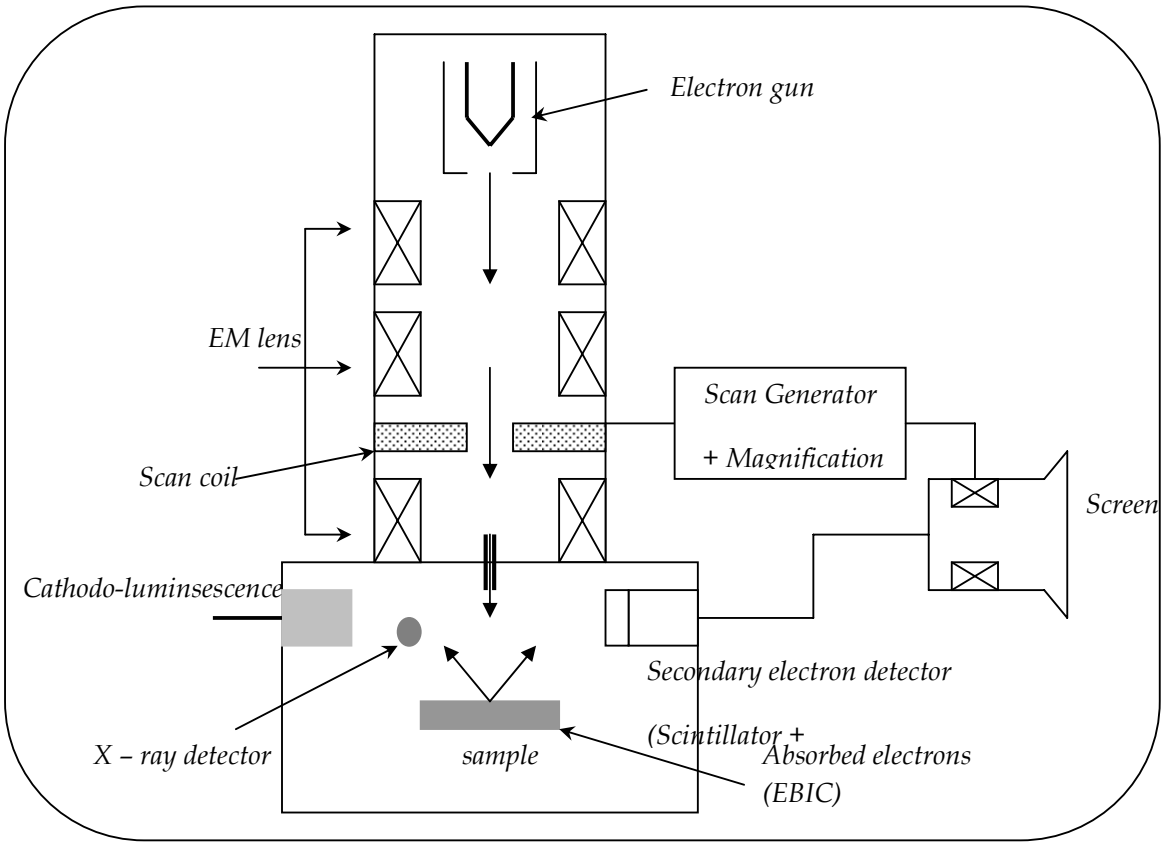

Figure 2.5. Schematic diagram of a Scanning Electron Microscope (SEM).

2.3.4. Scanning Probe Microscopy (SPM)

Scanning probe microscopy (SPM) covers several related technologies for imaging and measuring surfaces on a fine scale, down to the level of molecules and groups of atoms. SPM technologies share the concept of scanning an extremely sharp tip (3-50 nm radius of curvature) across the sample surface. The tip is mounted on a flexible cantilever, allowing the tip to follow the surface profile.

When the tip moves in proximity to the investigated object, forces of interaction between the tip and the surface influence the movement of the cantilever [19]. These movements are detected by selective sensors. Various interactions can be studied depending on the

mechanics of the probe. Our interest is in the atomic force microscope (AFM). The atomic force microscope (AFM) probes the surface of a sample with a sharp tip (often less than 100A^{o} in diameter). The tip is located at the free end of a cantilever that is 100 to 200μm long. Forces between the tip and the sample surface cause the cantilever to bend, or deflect. A detector measures cantilever deflections as the tip is scanned over the sample, or the sample is scanned under the tip. The measured cantilever deflection is mapped as the surface topography [20]. AFM can be used for insulator and semiconductor as well as electrical conductors [21]. The schematic diagram of AFM is shown in figure 2.6.

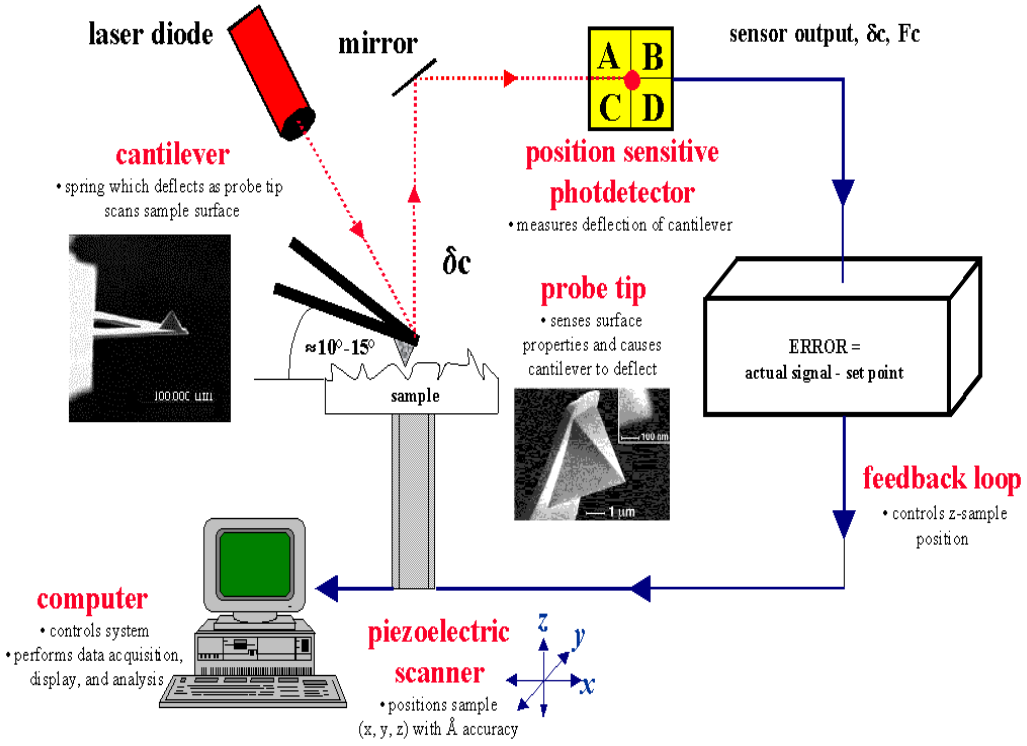

Figure 2.6. Schematic diagram of atomic force microscopy (AFM) [22].

Several forces contribute to the deflection of an AFM cantilever. The force most commonly associated with atomic force microscopy is an inter-atomic force called the Van der Waals force depending upon the distance between tip and sample as shown in figure 2.7.

Two distance regimes are labeled in figure 2.7 the contact regime and the non-contact regime. In the contact regime, the cantilever is held less than a few angstroms above the sample surface and the interatomic force between the cantilever and sample is repulsive [23]. In the non-contact regime, the cantilever is held about tens to hundreds of angstroms away from its attractive regime (largely a result of the long-range Van der Waals interactions).

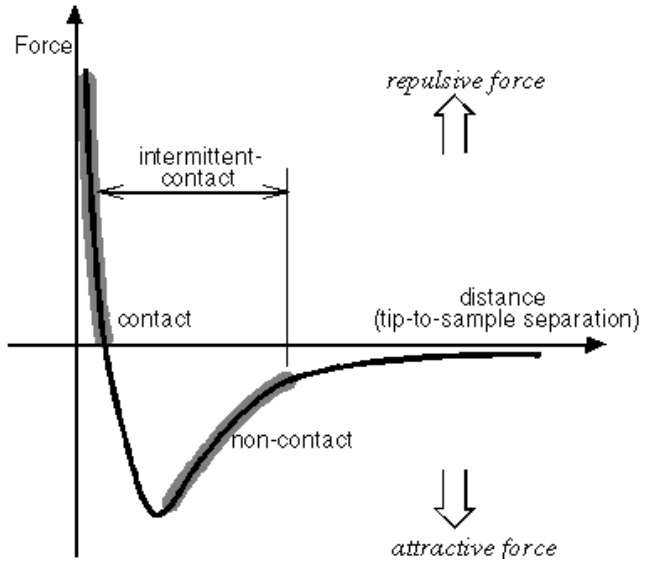

Figure 2.7. Nature of forces in the Contact and Non-contact mode of AFM operation.

2.3.4.1. Non-contact AFM

Non-contact AFM (NC-AFM, otherwise known as dynamic force microscope, DFM) is one of the modes of operation in AFM, where the cantilever is vibrated near the surface of the sample. The spacing between the tip and sample for DFM is of the order of tens to hundreds of angstroms. This spacing is indicated in the Van der Waal force curve in figure 2.7 as the non-contact regime.

DFM is desirable because it provides a means for measuring sample topography with little or no contact between the tip and sample. Similar to contact-AFM, DFM can also be

used to measure the topography of the insulator and semiconductors as well as electrical conductors. The total force between the tip and sample is very low, generally 10^{-12}N. Since the force between tip and sample in the non-contact regime is low, it is more difficult to measure this region than in the contact regime. In addition, the cantilever used in DFM is stiffer than those used for contact AFM because soft cantilevers can be pulled easily onto the sample surface. Hence, both these factors make the DFM signal difficult to measure. Thus, a sensitive, AC detection scheme is used in this operation. In the non-contact mode, the system vibrates a stiff cantilever near its resonant frequency (typically from 100 to 400 kHz). Then, it detects the changes in the resonant frequency or vibration amplitude as the tip comes near the sample surface. The sensitivity of this detection scheme provides sub-angstrom vertical resolution in the image, as with contact AFM.

The relationship between the resonant frequency of the cantilever and variations in sample topography can be explained as follows. The resonant frequency of a cantilever varies as the square root of its spring constant. In addition, the spring constant of the cantilever varies with the force gradient experienced by the cantilever. Finally, the force gradient, which is the derivative of the force Vs distance curve changes with the tip-to-sample separation. Thus, change in the resonant frequency of the cantilever can be used as a measure of change in the force gradient, which changes with the tip-to-sample spacing, or sample topography. DFM does not suffer from the tip or sample degradation effects that are sometimes observed after taking numerous scans with contact AFM. As mentioned above, DFM is preferable to contact AFM for measuring soft samples. In the case of rigid samples, contact and non-contact AFM for images may look the same. In the present study Seiko SPA-400 scanning probe microscope was used in the DFM mode to obtain the surface morphology of Ag, Au, Ag/Au, Au/Ag, Ag/TiO_2, Au/TiO_2, Ag/ZrO_2, Au/ZrO_2, and In/Ag thin film samples.

2.3.5. Transmission Electron Microscopy (TEM)

Electron microscopes use electron beams to provide images of nanoscale objects. In transmission electron microscopy (TEM), the specimen is illuminated with an electron beam. The electron beam that transmits through the specimen produces a transmitted, optical image, much like conventional optical microscopy. The wavelength of electron is much smaller than that of light, therefore the optimal resolution attainable for TEM image

is several orders of magnitude higher than that for a light microscope. Not all the electrons are transmitted through the sample, some are also scattered or diffracted. The scattered and diffracted electrons form the image contrast as denser or thicker parts of the sample scatter as well as absorb, more electrons, thus appearing as darker areas in the image [24-25].

In the present work we have used Transmission electron microscope (model: Tecnai 20 G2 STwin, FEI electron microscope operated at 20 kV using Gatan CCD camera) to investigate nano particle nucleation and growth and to determine crystal structure of Ag and Au thin films.

2.3.5.1. Imaging Modes of a TEM

The imaging system of a TEM consists of at least three lenses (Figure. 2.8): the objective lens, the intermediate lens (or lenses), and the projector lens. The intermediate lens can magnify the first intermediate image, which is formed just in front of this lens, or the first diffraction pattern, which is formed in the focal plane of the objective lens, by reducing the excitation [24]. In many microscopes, an additional diffraction lens is inserted between the objective and intermediate lenses to image the diffraction pattern and to enable the magnification to be varied in the range 102 to 106. The *bright-field mode* (BF) with a centered objective diaphragm is the typical TEM mode, with which scattering contrast and diffraction contrast can be produced with objective apertures α_o between 5 and 20 mrad. For high-resolution phase contrast, the aperture should be larger ($\alpha_o \geq 20$ mrad) to transfer high spatial frequencies. The only purpose of the diaphragm in this mode is to decrease the background by absorbing electrons scattered at very large angles. The resolution is limited by the attenuation of the contrast-transfer function (CTF) caused by chromatic aberration and not by the objective aperture α_o. Normally, the specimen is irradiated with small illumination apertures $\alpha_i \leq 1$ mrad. For high resolution, an even smaller aperture $\alpha_i \leq 0.1$ mrad is necessary to avoid additional attenuation of the CTF by partial spatial coherence. When unconventional types of contrast transfer are desired, it is often necessary to change the illumination condition by tilting the beam or using hollow-cone illumination, for example.

In the *dark-field mode* (DF), the primary beam is intercepted in the focal plane of the objective lens. Different ways of producing dark-field conditions are in use. The shifted-diaphragm method (Fig. 2.9 b) has the disadvantage that the scattered electrons pass through the objective lens on off-axis trajectories, which worsens the chromatic aberration. The most common mode is therefore that in which the primary beam is tilted (Fig. 2.9 c) so that the axis strikes the centered diaphragm. The image is produced by electrons scattered into an on-axis cone of aperture α_o. This mode has the advantage that off-axis aberrations are avoided. There is thus no increase of chromatic error.

Asymmetries in the dark-field image can be avoided by swiveling the direction of tilt around a cone, or conical illumination can be produced by introducing an annular diaphragm in the condenser lens. Another possibility is to use a central beam stop that intercepts the primary beam in the back focal plane for this, a thin wire stretched across a circular diaphragm may be employed (Fig. 2.9 d). DF micrographs need a longer exposure time because there are fewer scattered electrons. For high resolution, the contrast-transfer function (CTF) of DF is nonlinear, whereas the CTF of the BF mode is linear for weak-phase specimens. The DF mode can also be employed to image crystalline specimens with selected Bragg-diffraction spots.

Increasing the objective aperture in the BF mode allows us to transfer the primary and one Bragg-reflected beam through the diaphragm [24]. These beams can interfere in the final image. The fringe pattern is then an image of the crystal-lattice planes. Optimum results are obtained for this mode when the primary beam is tilted by the Bragg angle $+\theta_B$. The Bragg-reflected beam that is deflected by $2\theta_B$ passes through the objective lens with an angle $-\theta_B$ relative to the axis.

In the *crystal-lattice imaging mode*, more than one Bragg reflection and the primary beam form a lattice image that consists of crossed lattice fringes or an image of the lattice and its unit cells if a large number of Bragg reflections are used. This mode is most successful for the imaging of large unit cells, which produce diffraction spots at low Bragg angles so that the phase shifts produced by spherical aberration and defocusing are not sufficiently different to cause imaging artifacts. Further operating modes of a TEM are described in other sections: scanning transmission mode, Lorentz microscopy and the analytical modes

of x-ray microanalysis, electron energy-loss spectroscopy, and electron diffraction [24]. The Photograph of TEM used in this work is given in figure 2.10.

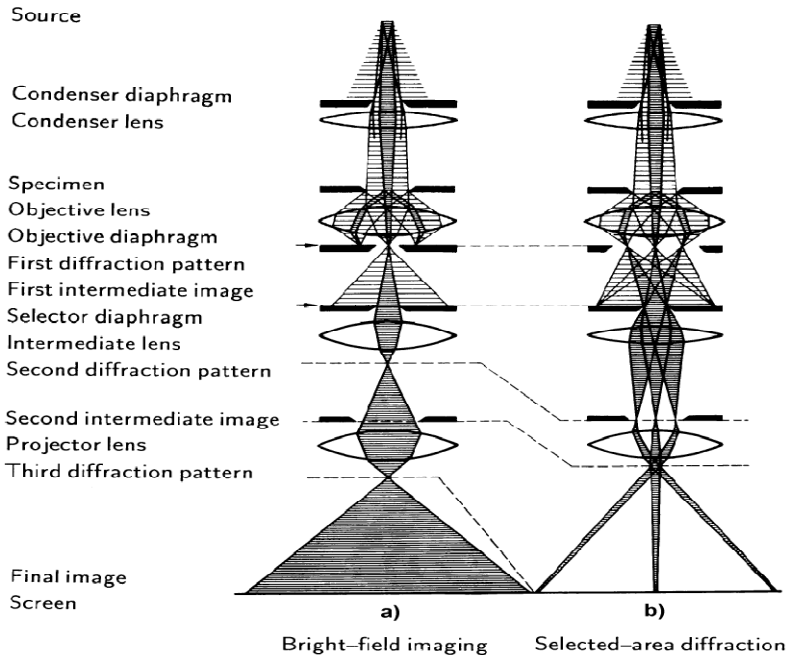

Figure 2.8. Ray diagrams for a TEM in (a) the bright-field mode and (b) selected area electron diffraction (SAED) mode [24].

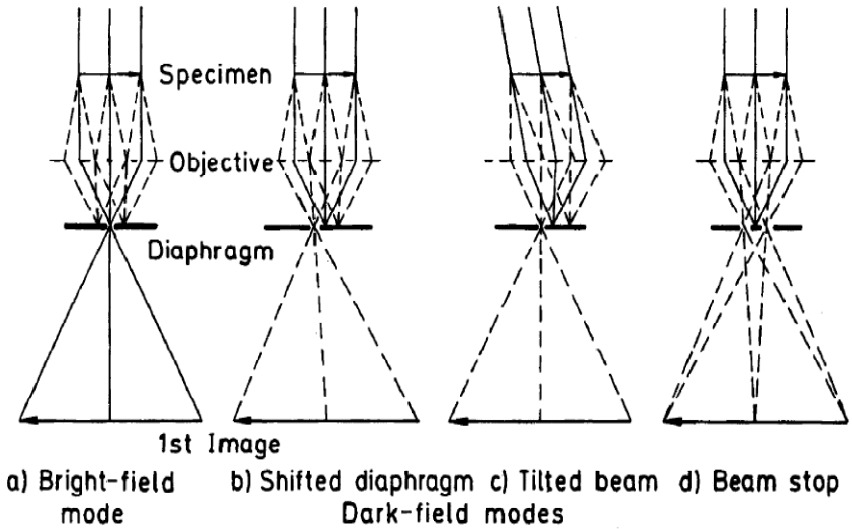

Figure 2.9. (a) Bright-field mode with a centered objective diaphragm and production of a dark-field mode by (b) a shifted diaphragm, (c) a tilted beam, and (d) a central beam stop [24].

2.3.5.2. Electron diffraction (ED)

Electron-diffraction methods are employed for the identification of substances by measuring the lattice-plane spacing and for the determination of crystal orientations in polycrystalline films (texture) or single-crystal foils. Extra spots and streaks, caused by antiphase structures or plate-like precipitates, for example, may also be observed when imaging a selected area. The selected-area diffraction technique, in which an area of the order of 0.1–1 μm across is selected by a diaphragm in the first intermediate image, is a standard method [24].

2.3.5.3. Selected-Area Electron Diffraction (SAED)

The cone of diffracted electrons with an aperture of the order of a few tens of milli radians (mrad) can pass through the small pole piece bores of the final lenses only if the back focal plane of the objective lens that contains the first diffraction pattern is focused on the screen. Figure 2.8(b) shows the ray diagram of this technique. A selector diaphragm of diameter *d* situated in the intermediate image plane (magnification M ≈20−50) in front of the intermediate or diffraction lens selects an area of the specimen of diameter d/M. This area can be chosen in the normal bright-field mode (figure. 2.8 a), in which the primary beam passes through the objective diaphragm. When the excitation of the intermediate lens is decreased, its focal length is increased and the diffraction pattern in the focal plane of the objective lens can be focused on the final screen after removing the objective diaphragm (figure. 2.8 b). The excitations of the later projector lenses are unchanged. These lenses magnify either the intermediate image or the diffraction pattern behind the intermediate lens. The diameter of the area selected cannot be decreased below 0.1–1 μm owing to the spherical aberration of the objective lens. The intermediate images of the Bragg reflections (dark-field images) are shifted relative to the bright-field image by a distance [24]

$$\Delta s = (Cs\theta^3_g - \Delta z\theta_g)\, M, \qquad (2.5)$$

which depends on the defocusing Δz and the constant Cs ($\theta g = 2\theta_B$ and θ_B is the Bragg angle). It is of course possible to compensate for the shift by a suitable choice of the defocus Δz, but only for one Bragg reflection, not for the whole diffraction pattern

simultaneously. The consequence is that Bragg reflections of high order with large θg do not come from the area that was selected in the bright-field mode. Thus, for $2\theta_B$ = 50 mrad and *C*s = 1 mm, the shift is 0.125 μm. The diffraction angle θg decreases linearly with λ as the electron energy is increased. A further selection error can result if the position of the intermediate image is shifted when the intermediate lens changes over from the imaging to the diffraction mode.

Figure 2.10. Photograph of the Transmission electron microscope (model: model: Tecnai 20 G2 STwin, FEI electron microscope operated at 20 kV using Gatan CCD camera) (established at CFN, UoH) used in the current study.

Diffraction patterns from smaller areas can only be obtained by using the rocking-beam technique or by producing a small electron probe. The resolution d/Δd of an SAED pattern can be defined in terms of the smallest lattice-spacing difference Δd that can be resolved and may be estimated from the ratio Δr/r. Here r denotes the distance from a diffraction spot to the center of the diffraction pattern in the focal plane of the objective lens, $r = 2\theta_B f = \lambda f/d$ (*f*: focal length), and Δr is the diameter of the spot, which is equal to the diameter $2\alpha_i f$ of the primary beam (α_i: illumination aperture):

$$d/\Delta d = r/\Delta r = \lambda/2\alpha_i d \qquad (2.6)$$

Thus, for λ = 3.7 pm (100 keV), d = 0.1 nm, and α_i = 0.1 mrad, we find d/Δd = 200. The resolution can be increased only by reducing α_i, but this reduces the pattern intensity. The spherical aberration of the objective lens can cause barrel and spiral distortion of the SAED pattern but this is, however, smaller than 1%; an elliptic distortion can arise due to astigmatism of the intermediate lens. The most severe distortion is caused by the projector lens. For the accurate determination of lattice spacing *d*, the diffraction (camera) length *L*) must be calibrated by using a diffraction standard [24]. The photographic image of the TEM used in the current study is shown in fig.2.10.

2.3.6. Optical Characterization

2.3.6.1. Ultra Violet-Visible Spectrophotometer

Optical properties of the Ag, Au and Ag, Au /dielectric bilalyer and metal bilayer thin films were studied using a JASCO V-570 UV-VIS-NIR double beam Spectrophotometer. The optical studies of thin films are mainly concerned with basic optical phenomena including absorption, reflection and transmission and also the interaction of photon energy with mater and consequent changes in electronic states [26]. The important parameters that can be obtained from the measured spectral absorption data include absorption coefficient and optical band gap. In the present study the data were collected in the range 190 to 2500 nm, with air as reference.

The Ultra Violet -Visible-Near Infrared (UV-VIS-NIR) spectrophotometer uses two light sources, a deuterium (D_2) lamp for ultraviolet region and a halogen lamp for visible and NIR region. The light from the source lamp gets reflected from mirror 1 and beam passes through slit 1 and hits a diffraction grating. The grating can be rotated allowing for a specific wavelength to be selected. At any specific orientation of the grating, only monochromatic (single wavelength) beam successfully passes through slit 2. A filter is used to remove unwanted higher order diffracted beam. The light beam hits a second mirror before it gets split by a half mirror (half of the light is reflected, the other half gets transmitted). One of the beams is allowed to pass through a reference sample (air in the present case), the other passes through the film coated substrate. The intensities of the light beams are then measured at the end as shown in figure 2.11. The photometer (not

shown) computes the ratio of the sample signal to reference signal (I/I_0) to obtain the transmittance.

An electronic transition consists of the promotion of an electron from an orbital of a molecule in ground state to an unoccupied orbital by absorption of a photon. The molecule is then said to be in an excited state.

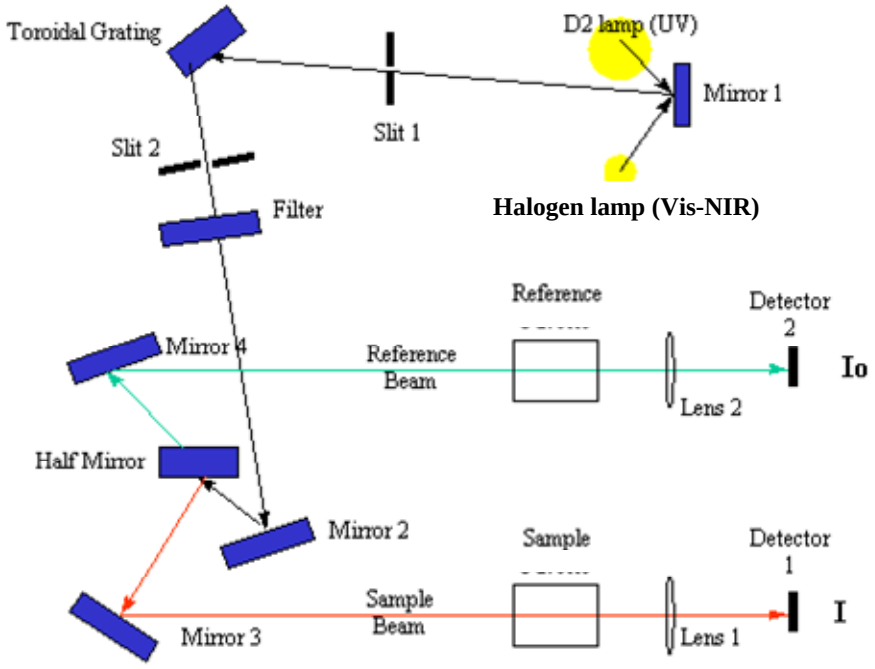

Figure 2.11. Schematic diagram of UV-VIS-NIR spectrophotometer.

Experimentally, the efficiency of light absorption at a wavelength λ by an absorbing medium is characterized by the absorbance A(λ) or the transmittance T(λ), defined as [27]

$$A(\lambda) = \log_{10} I_\lambda^0 / I_\lambda = -\log T(\lambda) \qquad (2.7)$$

$$T(\lambda) = \frac{I_\lambda}{I_\lambda^0}$$

where I_λ^0 and I_λ are the light intensities of the beams and entering and leaving the absorbing medium, respectively.

Usually the absorbance of a sample follows the Beer-Lambert law

$$A(\lambda) = \log_{10} \frac{I_\lambda^0}{I_\lambda} = \varepsilon(\lambda) lc \qquad (2.8)$$

where A is the measured absorbance, I_0 is the intensity of the incident light at a given wavelength, I is the transmitted intensity, L the path length through the sample, and c the concentration of the absorbing species. For each species and wavelength, ε is a constant known as the molar absorptivity or extinction coefficient. This constant is a fundamental molecular property in a given solvent, at a particular temperature and pressure, and has units of $1 / M * cm$ or often $AU / M * cm$.

References

1. S. S. Todorov, H. Bu, K. J. Boyd, J. W. Rabalais, C. M. Gilmore and J. A. Sprague, Surface Science **429** (1999) 63.
2. J. Nguyen, J. S. Yu, A. Evans, S. Slivken and M. Razeghi, Appl. Phys. Lett. **89** (2006) 111113.
3. H. Liu, S. Xiong, L. Li and Y. Zhang, Thin Solid Films, **484** (2005) 170.
4. R. Balu, A. R. Raju, V. Lakshminarayanan and S. Mohan, Materials Science and Engineering B, **123** (2005) 7.
5. L. Huang, K. W. Hipps, J. T. Dickinson, U. Mazur and X. D. Wang, Thin Solid Films, **299** (1997) 104.
6. J. W. Lim and M. Isshiki, J. Appl. Phys. **99** (2006) 094909.
7. M. Sasase, T. Nakanoya, H. Yamamoto and K. Hojou, Thin Solid Films **401** (2001) 73.
8. M. A. Nitti, A. Valentini, G. S. Senesi, G. Ventruti, E. Nappi and G. Casamassima, Appl. Phys. A **80** (2005) 1789.
9. T. Gallasch, T. Stockhoff, D. Baither and G. Schmitz, Journal of Power Sources **196** (2010) 428.
10. C. Ronning, D. Schwen, S. Eyhusen, U. Vetter and H. Hofsass, Surface and Coating Technology **158-159** (2002) 382.
11. K. Shimura, K. Yamaguchi, H. Yamamoto, M. Sasase, S. Shamoto and K. Hojou, Nuc. Inst. and Meth. in Phys. Res. B **242** (2006) 673.
12. T. Ichinohe, D. Kenmochi, H. Morisaki, S. Masaki and K. Kawasaki, Thin solid films **377-378** (2000) 87.
13. P. L. Tam and L. Nyborg, Surface & Coating Technology **203** (2009) 2886.
14. W. Ensinger and H. R. Muller, Surface and Coatings Technology **163-164** (2003) 281.
15. I. Kojima, B. Li, T. Fujimoto, K. J. Kim and D. W. Moon, J. Phys. D: Appl. Phys. **30** (1997) 2143.
16. K. U. Mahendra Kumar and M. G. Krishna, Semicond. Sci. Technol. **23** (2008) 105020.
17. K. Creath and A. Morales, *Contact and noncontact profilers in optical shop testing*, 2nd ed. Wiley, New york (1992).
18. B. D. Cullity, *X-ray Diffraction*, Addison-Wesley, Reading, MA (1956).

19. J. Giessibl Franz, *Review of Mod. Phys*., **75** (2003) 949.
20. P. West, *Introduction to Atomic Force Microscopy: Theory, Practice and applications* www. AFMUniversity.org.
21. Q. Zhong, *Surf. Sci. Lett*., **290** (1993) L688.
22. www.pscl.me.ntu.edu.tw
23. J.B. Hudson, *Surface Science-An introduction*, Wiley, New York (1998).
24. L. Reimer H. Kohl, '*Transmission Electron Microscopy Physics of Image Formation*', **5th** Ed, Springer, New York, 10013, USA (2008). TEM book
25. Z. L. Wang, Transmission Electron Microscopy of Shape-Controlled Nanocrystals and Their Assemblies, *J. Phys. Chem. B,* **104** (2000) 1153-1175.
26. Olaf Stenzel, *The Physics of thin film Optical Spectra: an Introduction*, Springer Germany (1996).
27. R. Swanepoel, J. Phys. E: Sci. Instrum., **16** (1983) 1214.

Chapter III: Morphology and structure of ion beam sputter deposited metal thin films

Abstract

This chapter presents the study of microstructure and structure of single layer Ag and Au thin films by Ion Beam Sputter Deposition (IBSD) with argon ion energy in the range of 150 to 450 eV and beam current of 4 – 6 mA. The films were grown at temperatures from 30 to 300^{o}C. It is shown that IBSD offers better controls over parameters for deposition of fine uniform thin films with controlled microstructure as compare to other physical vapour deposition techniques like DC sputtering and thermal evaporation. IBSD can be used as a non-lithographic technique to deposit self assembled/ordered nanostructured thin films. Different variety of nanostructures including self organized arrays of nanoparticles, nanoclusters and nanoneedles have been achieved. The coalescence behaviour of grown films are discussed and explained using known theory of growth mechanism of the thin films.

Chapter III: Morphology and Structure of ion beam sputter deposited metal thin films

3. Introduction

Recently, research on nanostructured metals has attracted much attention due to their applications in plasmonics and photonics. Two approaches are normally followed to achieve nanostructures in thin film form. The first set of techniques is based on lithographic techniques such as electron beam lithography, nanoimprint technology etc. [1, 2]. The second set of techniques is based on non-lithographic and direct writing methods such as focused ion beam, dip pen lithography, laser shock processing, electric field induced nanostructuring etc. [3, 4] Both these sets of approaches are post-processing methods that achieve nanostructures after a film is deposited on a substrate.

A third approach that has been successfully used for realizing a wide range of nanostructures are those based on soft chemical processes leading to self-organized, self-ordered and self-assembled nanostructures [5-8]. However, studies on the use of Physical vapour deposition (PVD) techniques to fabricate such structures are sparse [9, 10**].**

There are generally four main steps in the evolution of thin films deposited on substrates by PVD [11]. These are nucleation, island growth, agglomeration and finally continuous film. The first two stages would lead to largely discontinuous thin films. The microstructure at these early stages of growth would be controlled by process parameters like rates of deposition and substrate temperature and most importantly the nature of the film-substrate interface. For constant temperature and rate of deposition the growth would entirely be dependent on the nature of film-substrate interface. This is the basic premise of the current work and it is demonstrated that interfacial nanostructuring is a simple approach to achieve a variety of nanostructures such as nanoclusters, nanoparticle arrays and nanoneedles.

3.1. Comparison of microstructures

As mentioned above, there are many deposition techniques like chemical as well as physical vapor deposition but in the current work, we have used Ion Beam Sputter deposition (IBSD) technique to deposit metal thin films. IBSD technique has independently controllable parameters which provide flexibility in the deposition of novel thin film materials. One of the unique characteristics of IBSD is the ability to deposit multi component or multilayered materials using a single ion source. Ion beam sputter deposition offers the advantages of conventional sputtering while operating at a lower pressure. A low operating pressure minimizes the problem of substrate heating and gaseous impurity incorporation in the growing film. To show the flexibility and quality of films that can be fabricated by IBSD, we compared the microstructures of metal films deposited by ion beam sputter deposition technique with thermal evaporation and general DC sputtering.

Figure 3.1 shows the example of microstructure of Ag films deposited by different physical vapor deposition techniques. In figure 3.1 (a) Ag film deposited by IBSD at an Ar ion energy of 600 eV shows a uniform, spherical and dense microstructure compared to the films deposited by DC magnetron sputtering (at 300 V and 100 mA) and thermal evaporation technique shown in figure 3.1(b) and (c), respectively. The thickness of the films shown in the AFM image is 30 ± 3 nm for all the three films. It is also observed that the grain sizes are much smaller in the case of ion beam sputter deposited films compared to the other two techniques. The observed behavior of microstructure by IBSD is due to its independently controllable parameters, which is not possible in the other two techniques as difficult as mentioned in previous chapter. Therefore, it is concluded that the IBSD technique can be used to prepare very thin continuous films with good microstructure and also semicontinuous nanostructured thin films.

Some examples of microstructure of different metals deposited by ion beam sputter deposition are shown in Fig.3.2.

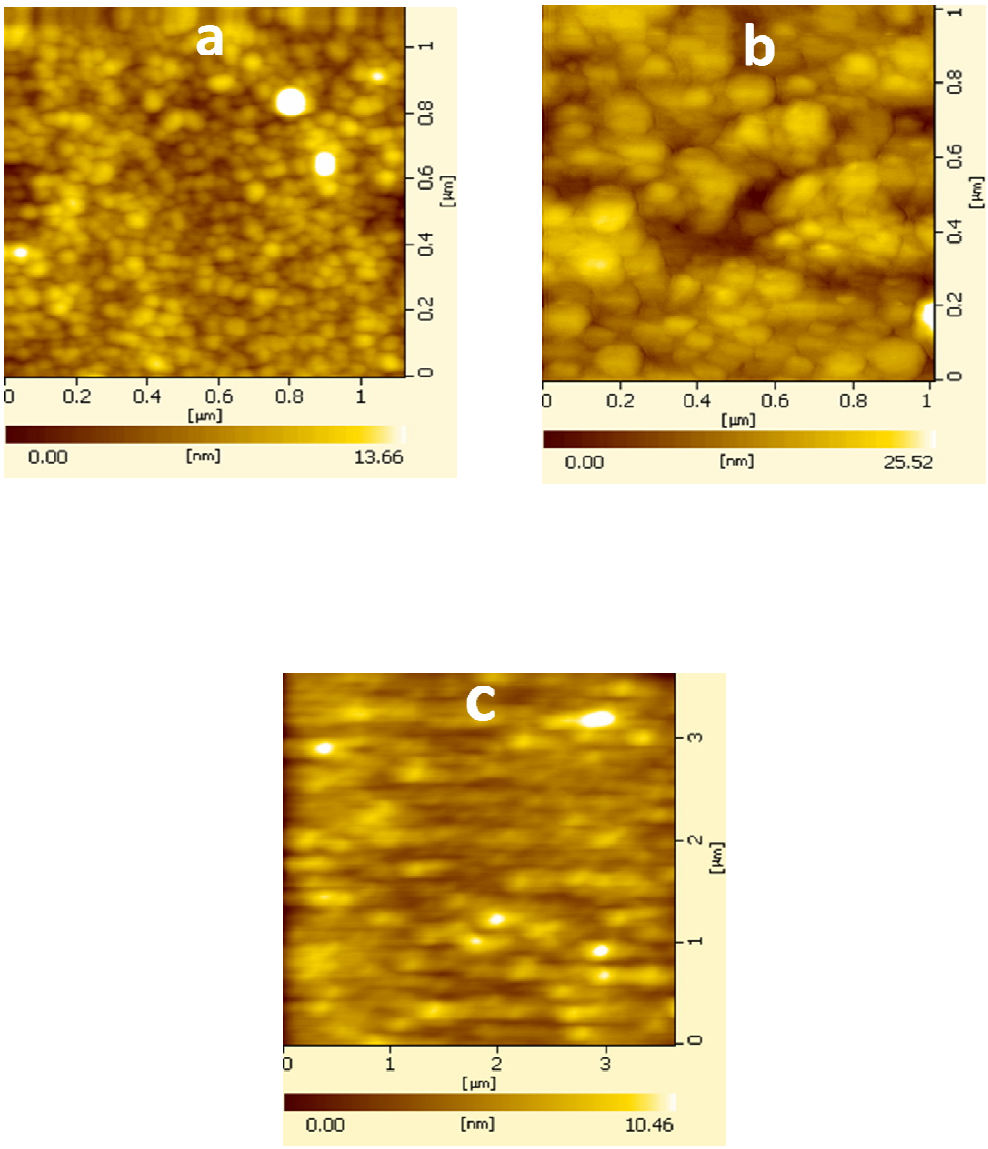

Fig. 3.1. AFM images of Ag thin films deposited by (a) Ion beam sputter deposited at 600 eV ion energy for 30 minutes (b) DC magnetron sputtered and (c) thermal evaporation.

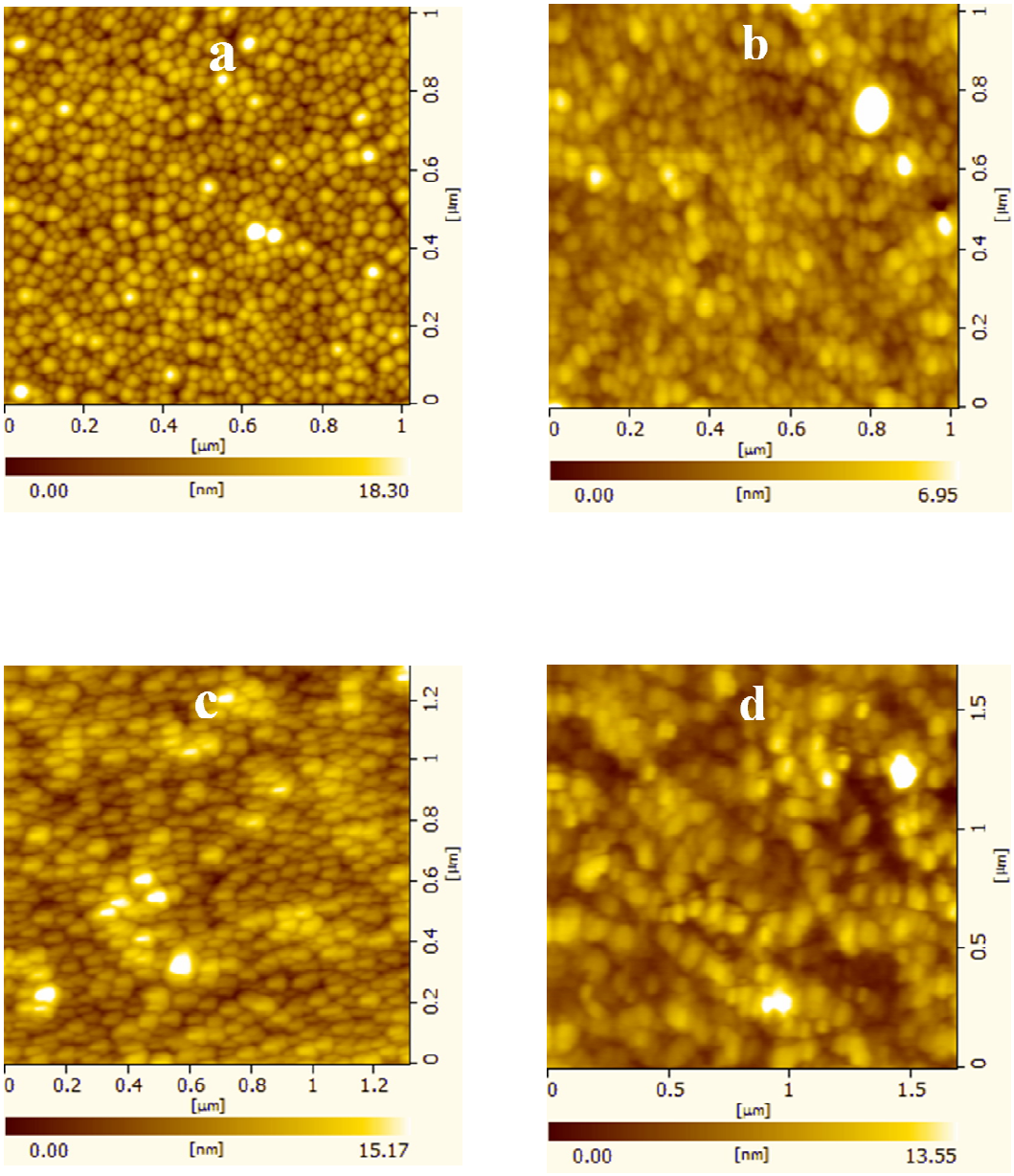

Fig.3.2. AFM images deposited by IBSD at 550 eV argon ion energy of (a) Ag (b) Au (c) Cu and (d) Ni thin films and its corresponding 3D view.

The morphology shown in AFM images in figs 3.1 and 3.2 are all for films deposited at ion energy of > 500 eV.

3.2. Optimization of ion beam parameters

In order to fabricate nanostructured thin films, the films were deposited at ion energy < 500 eV and a systematic study was done to estimate the thickness of the films. A graph of typical variation in the rate of deposition as a function of ion energy is shown in fig.3.3. It is evident that the rate of deposition increases with increase in incident ion energy from 150 to 600 eV. In this optimization experiment, the total duration of deposition was maintained constant as 30 mins., at each energy. The rate of deposition was calculated by dividing the measured thickness of the films with the deposition time. The minimum rate of deposition achieved was 0.01 nm/s at an ion energy of 150 eV. At this ion energy, the films became discontinuous for deposition durations <30 min. and therefore, measurement of thickness was not attempted for such films. For fixed incident ion energy, a linear dependence of thickness on duration of deposition was assumed and the thickness of the discontinuous films was thus estimated by simply multiplying the rate of deposition calculated earlier by the duration of deposition.

The evolution of morphology with increase in incident Argon ions energy is clearly seen in the AFM images displayed in Fig.3.4. For the same duration of deposition of 15 minutes, as the energy increases from 150 to 600 eV, the films are island-like at 150 eV and become continuous at 600eV. There are two effects of increase in the incident ion energy. The first is an increase in rate of deposition and the second is the consequent increase in thickness for the same duration of deposition. *i.e.* the film deposited at an incident energy of 150 eV for 15 min, will have a thickness of ~9 nm grown at 0.01 nm/s whereas the film deposited at 600 eV will have a thickness of ~32 nm grown at 0.04nm/s. In each case the corresponding roughness profiles are also shown. Very little correlation could be made between surface roughness and ion beam parameters.

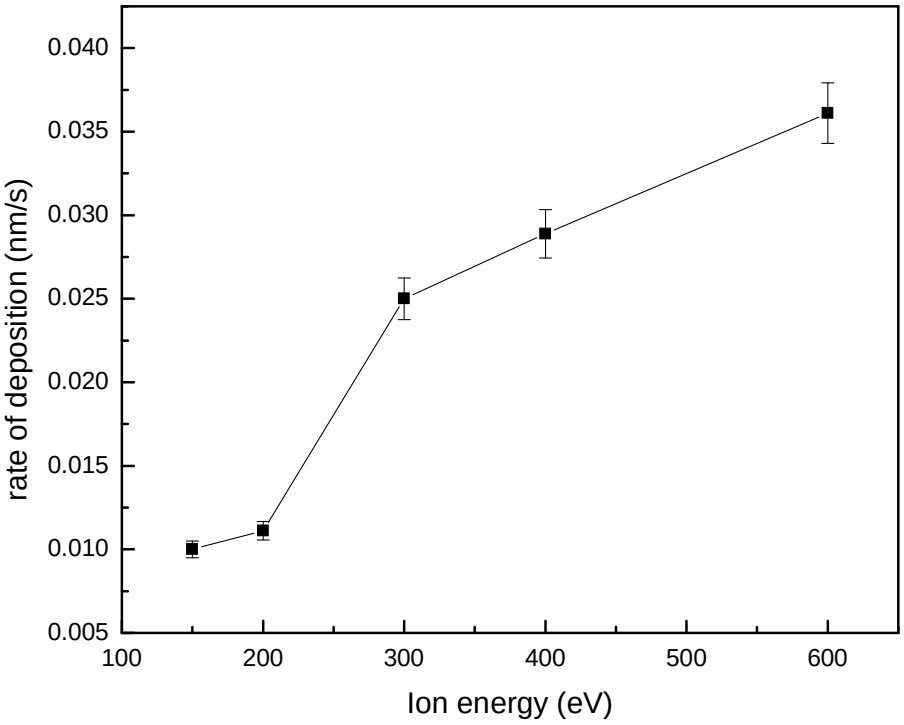

Fig.3.3. Variation in rate of deposition as a function of ion energy.

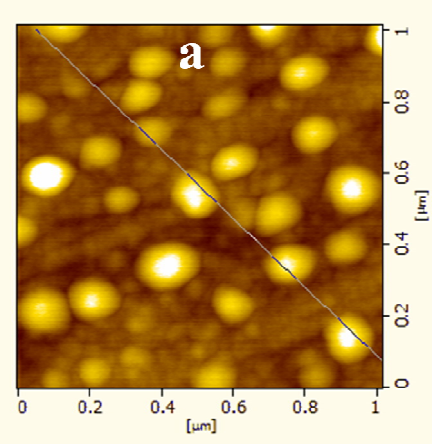
a
0
0.2
0.4
0.6
0.8
1
[µm]

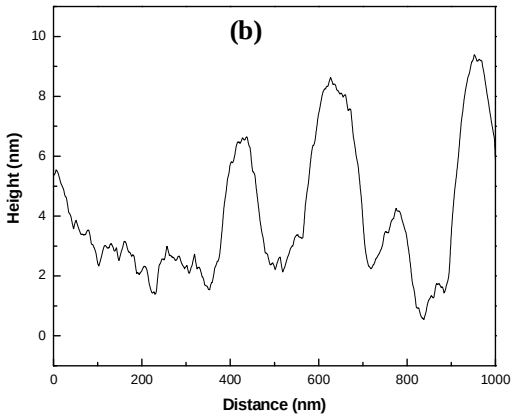
(b)
Height (nm)
Distance (nm)
0
2
4
6
8
10
0
200
400
600
800
1000

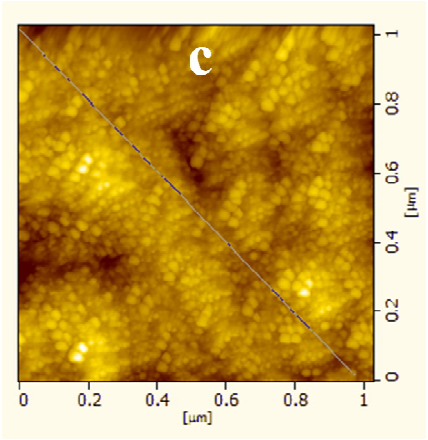
c
0
0.2
0.4
0.6
0.8
1
[µm]

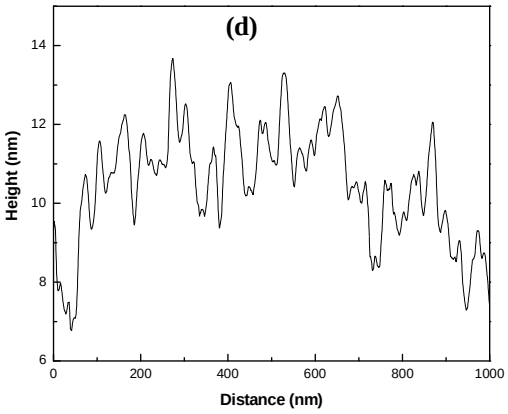
(d)
Height (nm)
Distance (nm)
6
8
10
12
14
0
200
400
600
800
1000

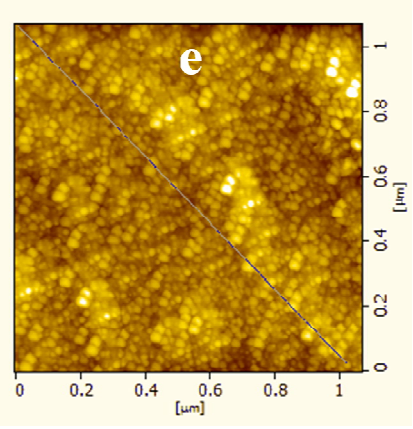
e
0
0.2
0.4
0.6
0.8
1
[µm]

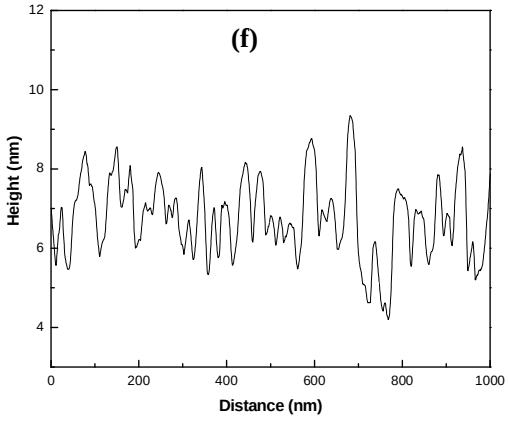
(f)
Height (nm)
Distance (nm)
4
6
8
10
12
0
200
400
600
800
1000

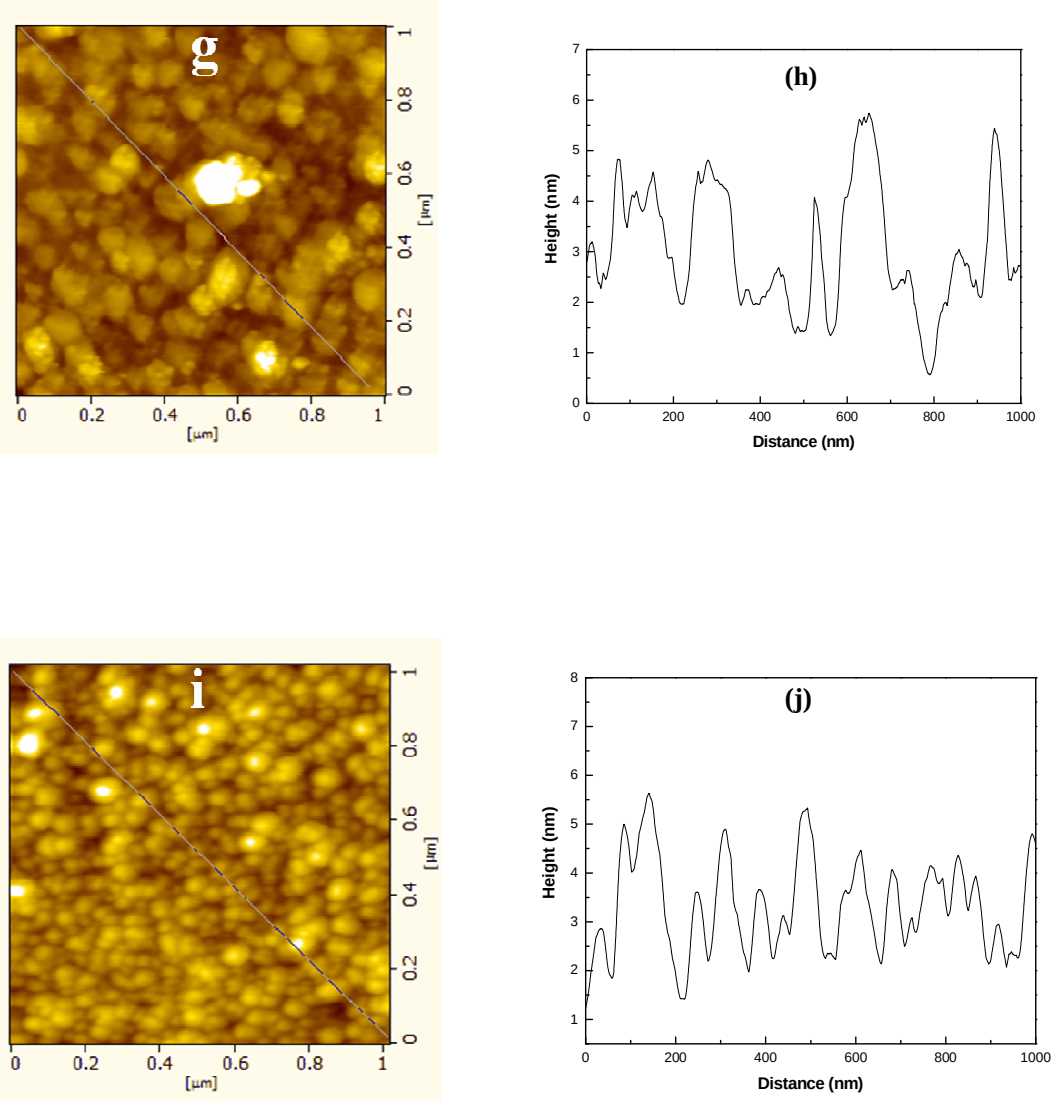

Fig.3.4. AFM images of Ag films deposited for 15 min at (a) 150 (c) 200 (e) 300 (g) 400 and (i) 600 eV and corresponding particle distance Vs height profiles are shown in (b), (d), (f), (h) and (j) respectively.

The combined effect, of the increase in rate of deposition and thickness, leads to the formation of a continuous film as the ion energy is increased. In addition, there is densification of the films as the ion energy is increased. The densification is accompanied by a decrease in particle sizes as a function of increasing ion energy as observed here. The particles size for the films deposited at 150 eV is measured to be 60-110 nm, at 200 eV it is 20-40 nm, at 300 eV particle size is 20-50, at 400 eV, it is measured to be 80-120 nm and at 600 eV, the particle size is measured to be 40-60 nm. It is clearly seen that initially the particle size is larger and then it becomes smaller with the increase of ion energy and at 400 eV it is much larger and at 600 eV it breaks down to 40-60 nm. It can be confirmed that at 400 eV ion energy, particle size reaches its critical size and breaks down to smaller with further increase of ion energy. It may be noted that with increase in energy there is an increase in thickness from 9 (at 150 eV) to 25 (at 400 eV) and finally 32 nm (at 600 eV).

In general, Physical Vapour deposition of continuous thin films onto substrates involves the following stages: nucleation, coalescence, island formation and finally continuous thin films. It has been demonstrated both theoretically and experimentally that at all stages of growth there is increase in the size of particles/aggregates/islands. The increase in size is dependent on process parameters such as rate of deposition and substrate as well as conditions on the substrate. It is observed that the above shown morphology is following the theories of thin film nucleation which are discussed below.

3.3. Theories of thin film nucleation: Kinetic processes in nucleation and growth

3.3.1. Nucleation rate:

The nucleation rate is a convenient synthesis of terms that describes how many nuclei of critical size form on a substrate per unit area, per unit time. Nuclei can grow through direct impingement of gas-phase atoms, but this is unlikely in the earliest stages of film formation when nuclei are spaced far apart. Instead, the rate at which critical nuclei grow depends on the rate at which adsorbed monomers (adatoms) attached to it.

The nucleation rate is essentially proportional to the product of three terms, namely,

$$= N^* A^* \left(\frac{nuclei}{cm^2} - s\right) \qquad (3.1)$$

N* is the equilibrium concentration (per cm^2) of stable nuclei and is the rate at which atoms impinge (per cm^2-s) onto the nuclei of critical area A* (cm^2). Upon calculation, the final nucleation rate becomes,

$$= 2\pi r^* a_0 \sin\theta \frac{PN_A}{(2\pi MRT)^{\frac{1}{2}}} n_s \exp\left(\frac{E_{des} - E_s - \Delta G^*}{k_B T}\right) \quad (3.2)$$

where, θ = contact or wetting angle,

r^* = critical nucleus size,

n_s = nucleation site density,

E_{des} = the energy required to desorb it back into the vapor,

E_s = the activation energy for surface diffusion.

ΔG^* = critical free energy, a_0 is adsorbed monomer jump distance and

M is mass of film material and R is the impingement rate.

The nucleation rate is a very strong function of the nucleation energetics which are largely contained within the term ΔG^*. A high nucleation rate encourages a fine-grained or even amorphous structure while a coarse-grained deposit develops from a low value of

.

3.3.2. Atomistic Models of the nucleation rate:

Atomistic theories of nucleation describe the role of individual atoms and associations of small numbers of atoms during the earliest stages of film formation. An important advance in the atomistic approach to nucleation was the theory proposed by Walton *et al.* [12] which treated clusters as macromolecules and applied concepts of statistical mechanics in describing them. They introduced the critical dissociation energy, E_i, defined to be that required to disintegrate a critical cluster containing i atoms into i separate adatoms. The critical concentration of clusters per unit area of size i, N_i, is given by,

$$\frac{N_i^*}{n_0} = (N_1/n_0)^{i^*} \exp(E_i^* / k_B T) \quad (3.3)$$

which expresses the chemical equilibrium between clusters and monomers. Here, E_i* may be viewed as the negative of a cluster formation energy, n_0 is the total density of

adsorption sites, and N_1 is the monomer density. Lastly, the critical nucleation rate (cm^{-2}-s^{-1}) emerges as,

$$_{i^*} = a_0^2 n_0 (\frac{}{n_0 \nu})^{i^*} \exp\left(\frac{(i^*+1)E_{des} - E_S + E_{i*}}{k_B T}\right) \quad (3.4)$$

Compared to the previous equation 3.2, this has the advantages of expressing the nucleation rate in terms of measurable parameters rather than macroscopic quantities such as ΔG^*, γ or θ. A thermally activated nucleation rate whose activation energy is dependent on the size of the critical nucleus is predicted by equation 3.4. This suggests the existence of critical temperatures where the nucleus size and orientation may undergo change. After the calculations,

$$= n_0 \nu \exp\left(-\frac{E_{des} + E_2}{k_B T_{1\to 2}}\right) \quad (3.5)$$

$T_{1\to 2}$ is temperature at which there is a transition from a one- to a two-atom nucleus.

3.3.3. Kinetic models of Nucleation:

Microscopic approaches to the modeling of nucleation processes have stressed the kinetic behavior of atoms and clusters containing a small number of atoms. Rate equations similar to those describing the kinetics of chemical reactions are used to express the time-dependent change of cluster densities in terms of the processes which occur on the substrate surface. It is appropriate to start with the fate of the mobile monomers. If coalescence is neglected, then

$$\frac{dN_1}{dt} = -\frac{N_1}{\tau_s} - K_1 N_1^2 - N_1 \sum_{i=2}^{\alpha} K_i N_i \quad (3.6)$$

Here, τ_s is mean free residence time before adsorbed monomer reevaporation.

This equations states that the time rate of change of the monomer density is given by their incidence rate, minus their desorption rate, minus the rate at which two monomers

combine to form a dimer. The latter term follows second-order kinetics with a rate constant K_1. The last term represents the loss in monomer population due to their capture by larger clusters containing two or more atoms. The general form of rate equation for clusters of size i is

$$\frac{dN_i}{dt} = K_{i-1}N_1N_{i-1} - K_iN_1N_i \qquad (3.7)$$

Where the first term on the right expresses their increase by attachment of monomers to smaller i-1 sized clusters, and the second term their decreases when they react with monomers to produce larger i+1 sized clusters. Transient as well as steady-state (*i.e.* where $dN_i / dt = 0$) solutions have been obtained for the foregoing rate equations for a variety of physical situations and for arbitrary values of i. They typically predicts that N(t) increases with time, eventually saturating at the value N_s. Venables [13] has summarized nucleation behavior for cases where i assumes any integer value. In general, the stable cluster density is given by,

$$N_s = An_0(/n_0\nu)^p \exp(E/k_BT) \qquad (3.8)$$

where A is a calculable dimensionless constant dependent on the substrate coverage. The parameters p and E have respectively yielded values for i* and the energies of desorption, diffusion, and cluster binding.

3.3.4. Cluster coalescence and depletion:

As previously mentioned, the density of stable nuclei increases with time upto some maximum level before decreasing because of coalescence phenomena. Growth and coalescence of nuclei are generally characterized by the following features:

1. A decrease in the total projected area of nuclei on the substrate occurs.
2. There is an increase in the height of the surviving clusters.
3. Nuclei with well-defined crystallographic facets sometimes become rounded.
4. The composite island generally reassumes a crystallographic shape with time.
5. When two islands of very different orientation coalesce, the final compound cluster assumes the crystallographic orientation of the larger island.

6. The coalescence process frequently appears to be liquid-like with islands merging and undergoing shape changes after the fashion of liquid droplet motion. This is specially true at elevated temperatures.
7. Prior to impact and union, clusters have been observed to migrate over the substrate surface in a process described as cluster-mobility coalescence.

Several mass transport mechanisms have been proposed in order to account for these coalescence phenomena and they are discussed in turn.

3.3.4.1. Ostwald Ripening:

Prior to coalescence there is a collection of islands of varied size, and with time the larger ones grow or ripen at the expense of the smaller ones. The desire to minimize surface free energy of the island structure is the driving force. Consider two isolated islands of surface tension γ of different size in close proximity. For simplicity, assume radii to be spherical with r_1 and r_2 and therefore the free energy (G) of a given island is $4\pi r_i^2 \gamma$ (I = 1, 2). The island contains a number of atoms n_i given by $4\pi r_i^3/3\Omega$, where Ω is the atomic volume. Defining the free energy per atom μ_i or chemical potential as dG/dn_i, after substitution,

$$\mu_i = \frac{d(4\pi r_i^2 \gamma)}{d(4\pi r_i^3/3\Omega)} = \frac{8\pi r_i \gamma dr_i}{4\pi r_i^2 dr_i/\Omega} = \frac{2\Omega\gamma}{r_i} \qquad (3.9)$$

In chemical thermodynamics the chemical potential is often associated with the so-called escaping tendency of atoms. Where μ is large the effective atomic concentration is large, forcing them to escape to where μ is small. Ostwald ripening processes never reach equilibrium during film growth.

3.3.4.2. Sintering:

Sintering is a coalescence mechanism involving islands in contact. In the case of sintering or coalescence of contacting sphere of radius r, theoretical calculations in the metallurgical literature [14] have shown that the sintering kinetics is given by

$$X^n / r^m = A(T)t. \qquad (3.10)$$

Here X is the neck radius, A(T) is a temperature-dependent constant that varies with mass transport mechanism, n and m are constants, and t is the time. Of the several mechanisms available for mass transport in films, the two most likely ones involve diffusion either through the bulk or via the surface of the islands. For bulk diffusion n = 5, m = 2, whereas for surface diffusion n = 7, m = 3. Typical thumbnail calculations show that surface diffusion dominates sintering. While surface energy and diffusion-controlled mass transport mechanisms undoubtedly influence liquid-like coalescence phenomena, sintering mechanisms are unable to explain the following:

1. Observed liquid-like coalescence of metals on substrates maintained at 77 K where atomic diffusion is expected to cease.
2. Widely varying stabilities of irregularly shaped necks, channels, and islands possessing high curvatures at some points.
3. The large range of times required to fill visually similar necks and channels.
4. Enhanced coalescence in the presence of an applied electric field in the substrate plane.

3.3.4.3. Cluster migration:

The last mechanism for coalescence considered deals with migration of clusters on the substrate surface. Coalescence occurs as a result of collisions between separate island-like crystallites (or droplets) as they execute random motion. Interestingly, the mobility of metal particles can be significantly altered in different gas ambient. Not only do the clusters translate, but they have been observed to rotate as well as even jump on each other and sometimes reseparate thereafter. Cluster migration has been observed in many systems, e.g., Ag and Au on MoS_2, Au and Pd on MgO and Ag and Pt on graphite in so called conservative systems, *i.e.*, where the mass of the deposit remains constant because further deposition from the vapor has ceased [15, 16].

The surface migration of a cap-shaped cluster with projected radius r occurs with an effective diffusion coefficient D(r) having units of cm^2 / s. The movement of peripheral cluster atoms, the fluctuations of areas and surface energies on different faces of equilibrium-shaped crystallites, and the glide of crystallite clusters aided by dislocation

motion are three models which show the dependence of D on r. In each case D(r) is given by an expression of the form [17],

$$D(r) = B(T) / r^{s} \exp - (E_c / k_B T) \qquad (3.11)$$

Where B(T) is a temperature-dependent constant and s is a number ranging from 1 to 3. The cluster migration is thermally activated with an energy E_c related to that for surface self-diffusion, and that it is more rapid the smaller the cluster.

3.3.4.4. Coalescence and grain size:

The formation of polycrystalline film, particularly terms such as nucleation, growth, and coalescence, has a familiar ring in the metallurgical literature of solid-state phase transformations. For example, a cold-worked metal matrix transforms by nucleation of recrystallized grains (islands) followed by growth, thus consuming the surrounding matrix so that there is less area available for new nuclei. During recrystallization one region will start ahead of others because of some favorable local composition, temperature, defect, or bias in the system. Then nucleation occurs elsewhere, and later somewhere else, while growth continues independently in regions of prior nucleation. The situation is much like rain droplets falling on a pond. Where rain impinges on the pond, surface wave nuclei are created. The circular ripples grow outward and begin to impinge on one another. When all of the prior untransformed matrix disappears by grain growth and impingement or coalescence, recrytallization is complete.

An important equation based on an analysis by Avrami [18] is useful in describing the kinetics of such transformations. For the case of film nucleation and growth in two dimensions where circular disk like nuclei grow, the form of the equation is

$$f(t) = 1 - e^{-\left[\pi/3\dot{G}^2 t^3\right]} \qquad (3.12)$$

Where f(t) is fractional amount of transformation and t is the time. Furthermore, (nuclei/cm^2-s) and $\dot{G}$ (cm/s) are the nucleation and linear growth rates respectively. As a function of log t, f(t) is small during what may be thought of as an initial incubation

period, then rises sharply when nucleation and growth rates overlap strongly, and finally saturates at f = 1. The Avrami equation strictly applies to closed systems transforming under conditions where there is no matter exchange with the surroundings. Inclusion of the adatom ring apparently extends the equations validity to open systems.

3.4. Morphology and structure on smooth substrate: Normal Coalescence

From the results presented in section 3.2, it is observed that the particles are large and isolated at very low ion energy deposition because surface mobility of the substrate is much larger than the material at that point due to which the film material freezes as soon as the material impinges on the substrate. It is confirmed that the deposition at very low rate and very low ion energy leads to the isolated and island kind nanostructured thin films. As given in the theory, there are four main steps in the evolution of thin films deposited by physical vapor deposition (PVD) technique. These are nucleation, island growth, agglomeration and finally continuous film. The first two stages would lead to largely discontinuous thin films. The microstructure at these early stages of growth would be controlled by process parameters like rates of deposition and substrate temperature. The film growth is controlled during the island formation stage, prior to the coalescence stage, leading to self ordered nanoparticle arrays with different sizes, shapes and interparticle separation.

Fig.3.5. (a) to (c) shows the morphology of the films deposited at 150 eV, for different deposition times or different thicknesses. As the thickness is increased from 6 to 18 nm, the films evolve from self-ordered nanostructures at 6 nm (Fig. 3.5.(a)) to semi-continuous films at 15nm (Fig. 3.5.(b)) and finally to almost continuous films at 18 nm (Fig. 3.5.(c)).

The AFM images clearly indicate that there is evolution in both shape as well as size of particles as a function of deposition parameters. The two parameters that have been controlled here are the rate of deposition (by controlling the incident ion energy at the target) and the thickness by fixing the duration of deposition time. The effect of increase in rate of deposition (fig.3.4) is to decrease the particle size, increase density of packing and thickness. On the other hand, the effect of increasing thickness (at a constant rate of

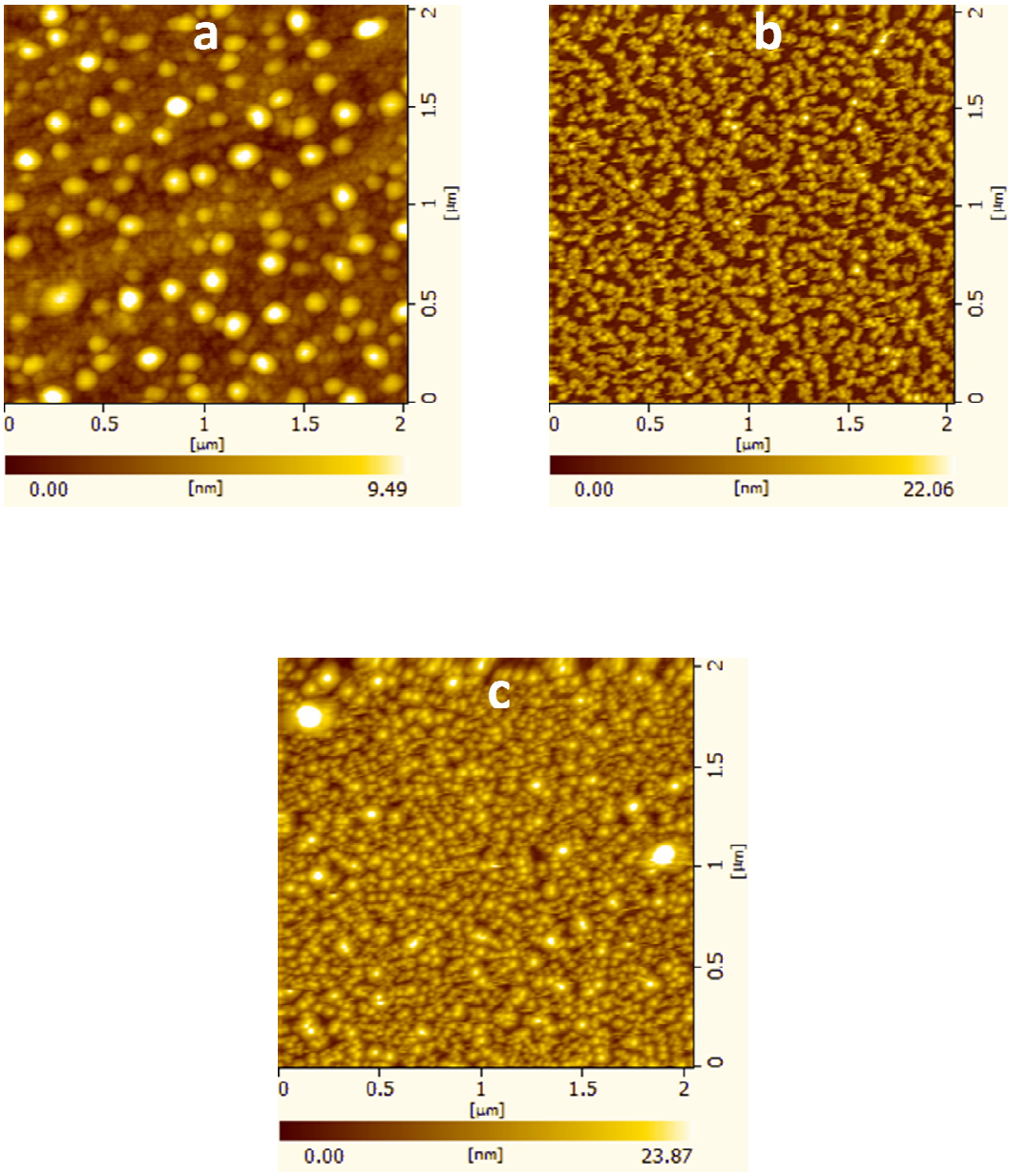

Fig.3.5. AFM images of the Ag films deposited at Ar ion energy of 150 eV at total duration of deposition of (a) 10, (b) 15 and (c) 30 minutes.

deposition) is to change the shape of particles from ellipsoidal to elongated particle chains that finally break in to a dense packed microstructure of small spherical particles (fig.3.5).

Fig.3.6. (a) – (c) shows the morphology of Au thin films deposited at 250 eV for different duration of time. The films were deposited for 10, 25 and 30 min at 250 eV of Ar ion energy. Here also, we observed that with the increase of deposition time or thickness, the films becomes denser and continuous as observed in the case of Ag thin films. The reason for depositing Au film at 250 eV ion energy is because the sputter yield of Au is much lower than that for Ag. Hence, no film deposition occurred at 150 eV in the case of Au even for duration of 40 min.

The process of film formation by vapour deposition techniques involves the transition of a solid source material in to vapour that condenses on impact with the substrate surface in to a solid film (of the source material). It is clearly observed that the morphological evolution of films is therefore, profoundly influenced by conditions on the surface of the substrate and deposition parameters. In other words, the shape, size and spacing of particles are entirely dependent on accurate control of growth parameters such as pressure, temperature and rate of deposition. However, in the case of Au it is not consistent as in the case of Ag. It is due to the wettability of Au to the borosilicate glass substrate and the contact angle to the substrate.

The observed behaviour can be attributed to two factors namely: low rate of deposition and high contact angle to the substrate. To distinguish the contributions between each of these factors Au films were deposited on Carbon coated Cu grids (used for TEM) at the same beam energy. But it was found that the Au films did not exhibit any observable growth on carbon for energies upto 450eV, clearly indicating that the interfacial energy dominated over the low rate of deposition. “Potato” shaped cluster of particles appeared when the films were deposited on carbon at an ion energy of 450eV and for a duration of 25 min as shown in fig. 3.7(a). For comparison, the TEM image of an Ag film grown for 20 min directly onto carbon coated Cu grids at 150 eV is shown in fig. 3.7(b).

It is evident from this figure that Ag films have started nucleating as in the case of the films grown on the BSG substrates. It is observed that the Au films grown on BSG substrate and CCG are totally different. Au films grown on CCG has a boot shape kind of

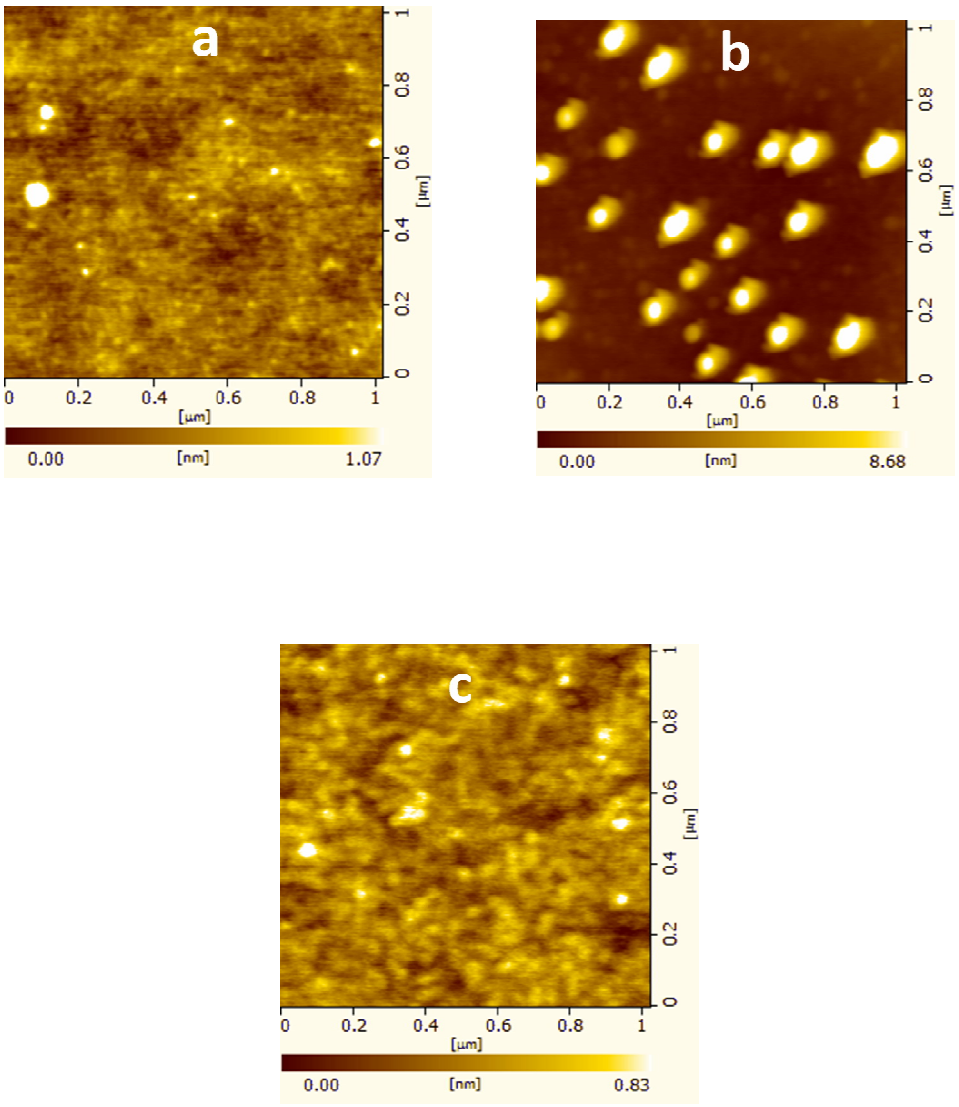

Fig.3.6. AFM images of the Au films deposited at Ar ion energy of 250 eV a total duration of deposition of (a) 10, (b) 25 and (c) 30 minutes.

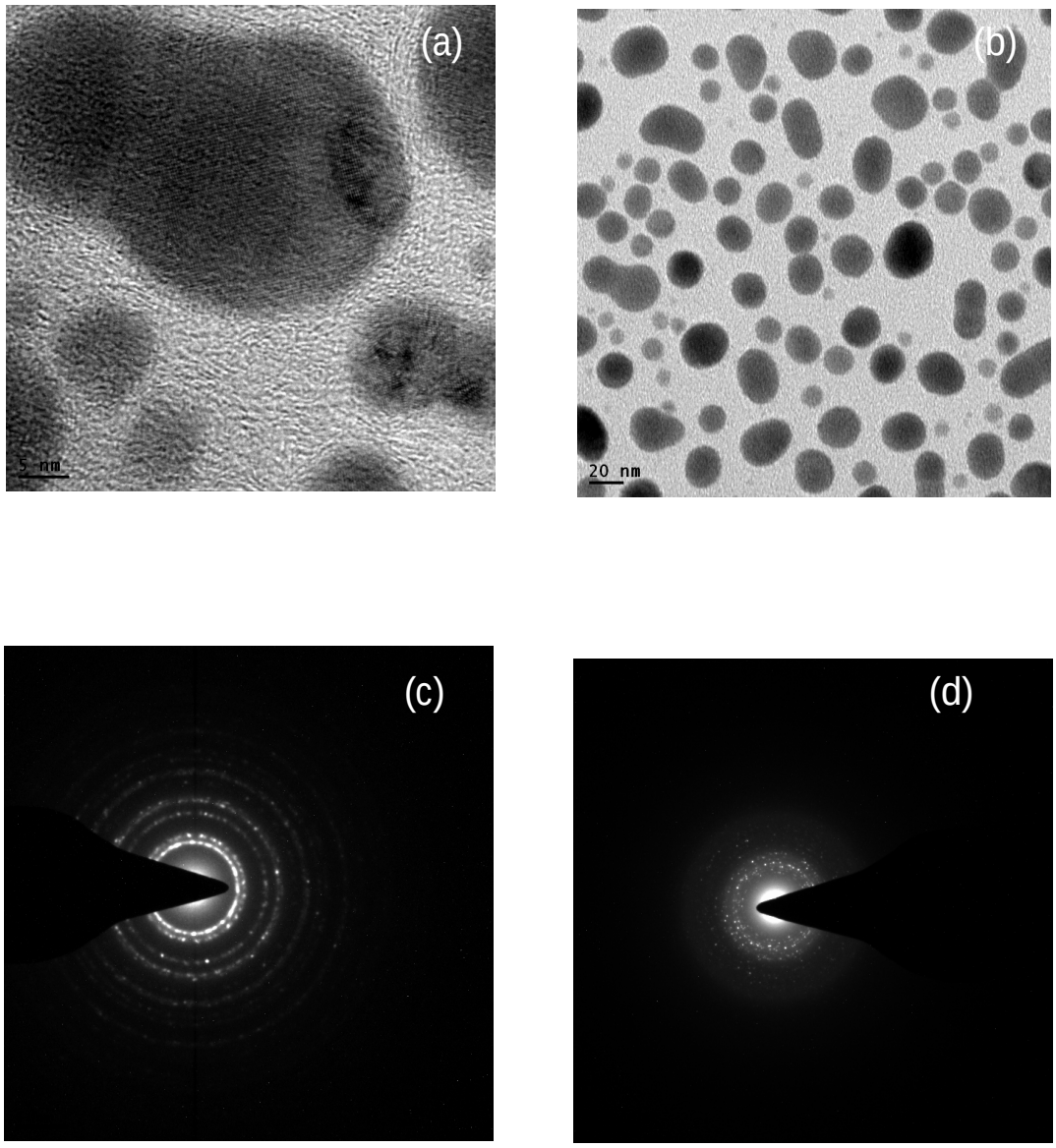

Fig.3.7. Transmission electron microscope images of (a) Au film deposited using an Ar ion energy of 450 eV for 25 min and (b) Ag film deposited using an Ar ion energy of 150 eV for 20

structures arranged themselves in array form. In both cases, Ag and Au deposited on carbon, the particles arrange themselves in the form of array with sizes between 5-20 nm. Therefore, it can be inferred that the interfacial energy of Au on BSG is lower than that for Au on carbon leading to the differences in growth on the two substrates. The high resolution TEM images displayed in figs.3.7.(a) and (b) and the selected area electron diffraction patterns shown in figs.3.7(c) and (d) for Au and Ag respectively indicate that the films are crystalline. It is observed that in both the substrates borosilicate glass and carbon coated Cu grid, the films are discontinuous and arranged in array form. The corresponding selected area diffraction patter is shown in fig3.7(c) and (d) respectively.

To investigate the growth patterns on a scale larger than those available with AFM and TEM, the growth was also examined under a scanning electron microscope. The early stages of growth on BSG substrates for both Ag (150 eV 10 min) and Au (250 eV 20 min) are similar, as seen from figs 3.8(a) and (b), respectively. The microstructure consists of an organized array of nanoparticles, as seen in the AFM and TEM images. Interestingly, in both cases the formation of nanoneedles has also been observed, as shown in figs 3.8(c) and (d) respectively for Ag and Au. They are of 500nm in length with diameters of the order of 30-40 nm. Interestingly in the case of Ag, the nanoneedle formation follows the process of organization in to an array of nanoparticles while it precedes it in the case of Au. The difference in behaviour can be attributed to the differences in interfacial energies in the two cases.

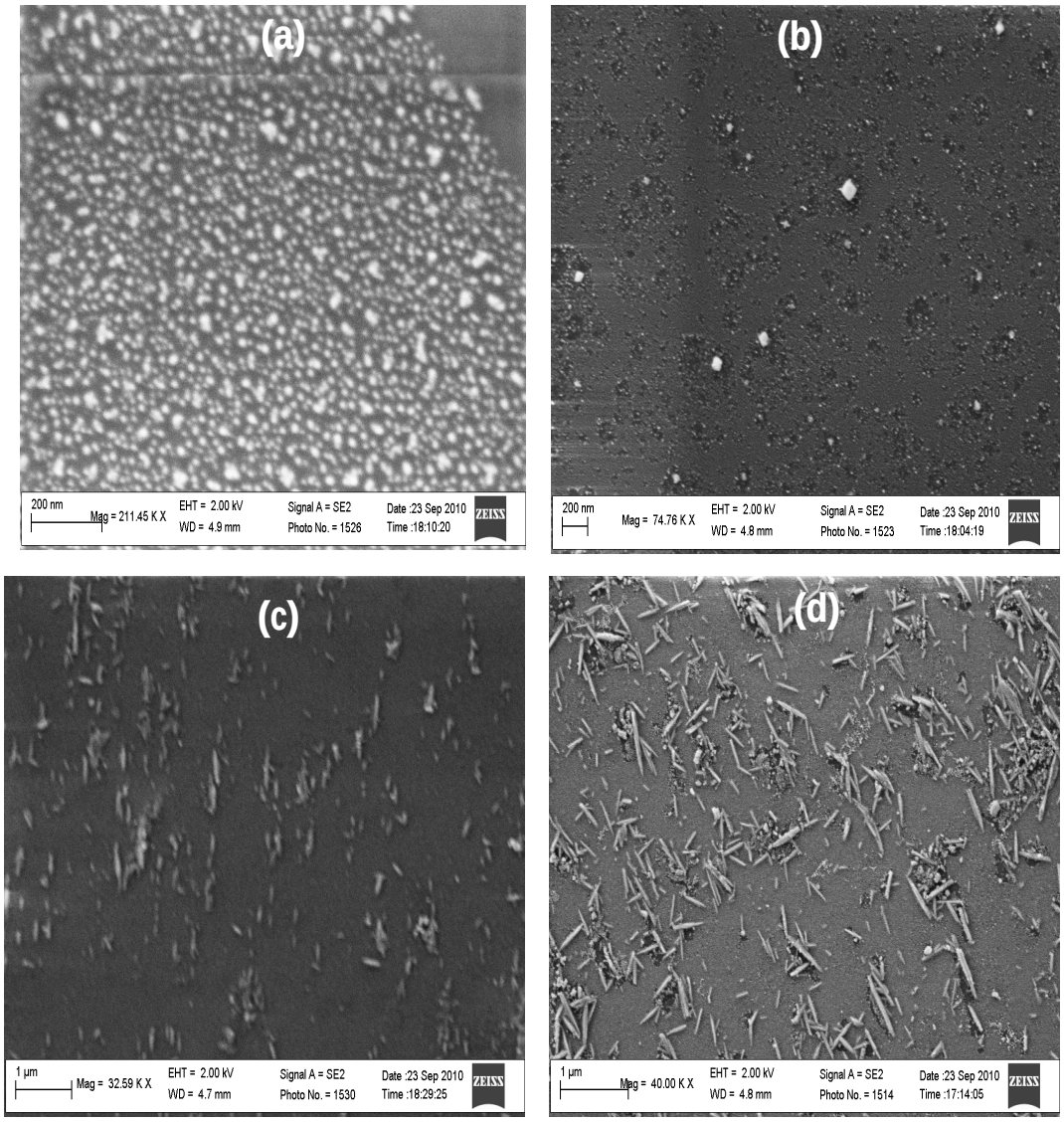

Fig 3.8. Scanning electron microscope images of (a) Ag film deposited using an Ar ion energy of 150 eV for 30 min, (b) Au film deposited using an Ar ion energy of 250 eV for 20 min onto (c) Ag film deposited using an Ar ion energy of 150 eV for 20 min and, (d) Au film deposited using an Ar ion energy of 250 eV for 30 min onto BSG substrates.

3.5. Morphology and structure on rough substrate: Abnormal coalescence

So far we have demonstrated the growth of films on different substrates at ambient temperature without considering the roughness of the surface of the substrate. There have been some attempts to model the growth of thin films on rough substrates [19-21]. The main aim of such work has been to study conditions under which smoothening of a thin film deposited on rough substrate occurs and can be controlled. There have been a few reports of experimental work where substrate roughness has been used as a control parameter for thin film growth [22–26]. All the earlier reports focus mainly on roughness evolution in the initial stages of growth but not on the size of islands/particles that constitute the film.

In this part, we demonstrate that substrate roughness influences not only film roughness in the initial stages growth but also the island sizes leading to abnormal coalescence behavior. Discontinuous Ag and Au films were deposited by low energy Ion beam sputter deposition onto rough carbon coated Cu grids (used for Transmission Electron microscopy) and borosilicate glass substrates. The evolution of morphology was studied by transmission electron microscopy (TEM) as well as atomic force microscopy (AFM). The Ag films were deposited at Argon ion energy of 150 eV while the Au films were deposited at ion energy of 450 eV. Here, two sets of experiment are done. One set of experiments was carried out on Ag and Au by varying deposition temperature from room temperature to 200 and 300^0C for a constant duration of 40 mins. Another set of experiments was carried out on Au at constant temperature 300^0C but time was varied from 5 to 15 mins.

Fig.3.9. shows the typical bright field TEM images of Ag films deposited at various temperatures. Room temperature sputter deposited films are shown in fig.3.9(a), and the corresponding particle size distribution is shown in Fig.3.9(b) and deposition at temperature 200 and 300^0C are shown in fig.3.9(c)-(d) – fig.3.9(e)-(f).

It is evident that these films are discontinuous and are comprised of spherical particles with a peak diameter of 15 nm. As we increase the deposition temperature to 200^oC, it is evident from the micrographs shown in Fig.3.9(c) that these particles are still spherical in nature with absence of particles of size greater than 15 nm (Fig.3.9(d)). The peak in this

case occurs at ~ 12 nm. A further increase in substrate temperature to 300^{o}C causes the particle size to become smaller with absence of particles greater than 12 nm size. The nanoparticle nature of the films is retained even at this temperature (fig.3.9(e) and (f)).

Fig.3.10. shows the bright field TEM images of the Au films deposited at various temperatures under a fixed deposition time of 25 minutes. It is observed that, in contrast to the Ag films, the Au films deposited at room temperatures have shown "boot-shaped" particles as shown in the micrograph Fig.3.10(a). Corresponding lattice fringes are shown in Fig.3.10(b). As we increase the deposition temperature to 200 ^{o}C, it is clear that these clusters break up to in to smaller particles that are ellipsoidal in shape (shown in Fig. 3.10 (c)-(d)). At substrate temperature of 300^{o}C, these particles change to spherical in shape as shown in the micrographs in Fig.3.10 (d)-(f). These gold particles remain crystalline at all temperatures studied here. The corresponding high resolution lattice fringes are best indexed with pure gold. It is very interesting that these gold nanoparticles exhibit (111) texture at all temperatures.

The following observations can be made from figs 3.9 and 3.10.

1. The gold films are less discontinuous than the silver films with lower island density.
2. At room temperature, the Ag nanoparticles are nearly spherical in shape with interparticle separation that is larger than the particle diameter
3. The Au particles cluster together to form the boot-shaped aggregates. The number density of these aggregates is small and the separation is smaller than their size on average.
4. As substrate temperature increases, the size of particles, in Ag and that of aggregates in Au decreases. It appears that the number density decreases in Ag but remains constant in the case of Au.
5. Both films show crystallinity but Au exhibits a (111) texture at all temperatures.
6. The island density increases with increase in temperature from approximately 3 x10^{15}/m^{2} ambient temperature to 1 x10^{16}/m^{2} at 300^{o}C, but the fragmentation is accompanied by decrease in inter-island distance.

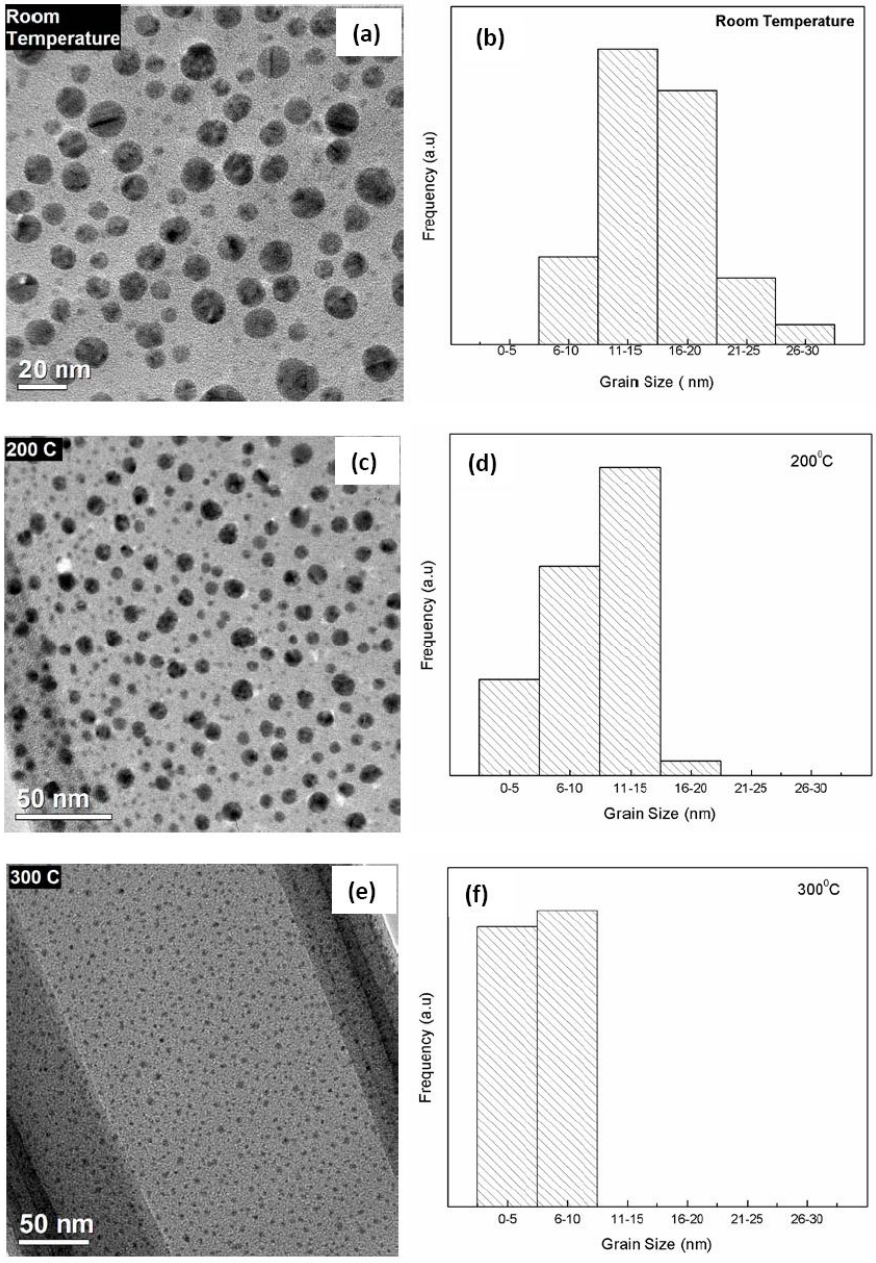

Fig.3.9. TEM images of Ag films and corresponding grain size distribution curve deposited at Room temperature (a)-(b), at 200°C (c)-(d) and 300°C (e)-(f) for 40 min at 150 eV.

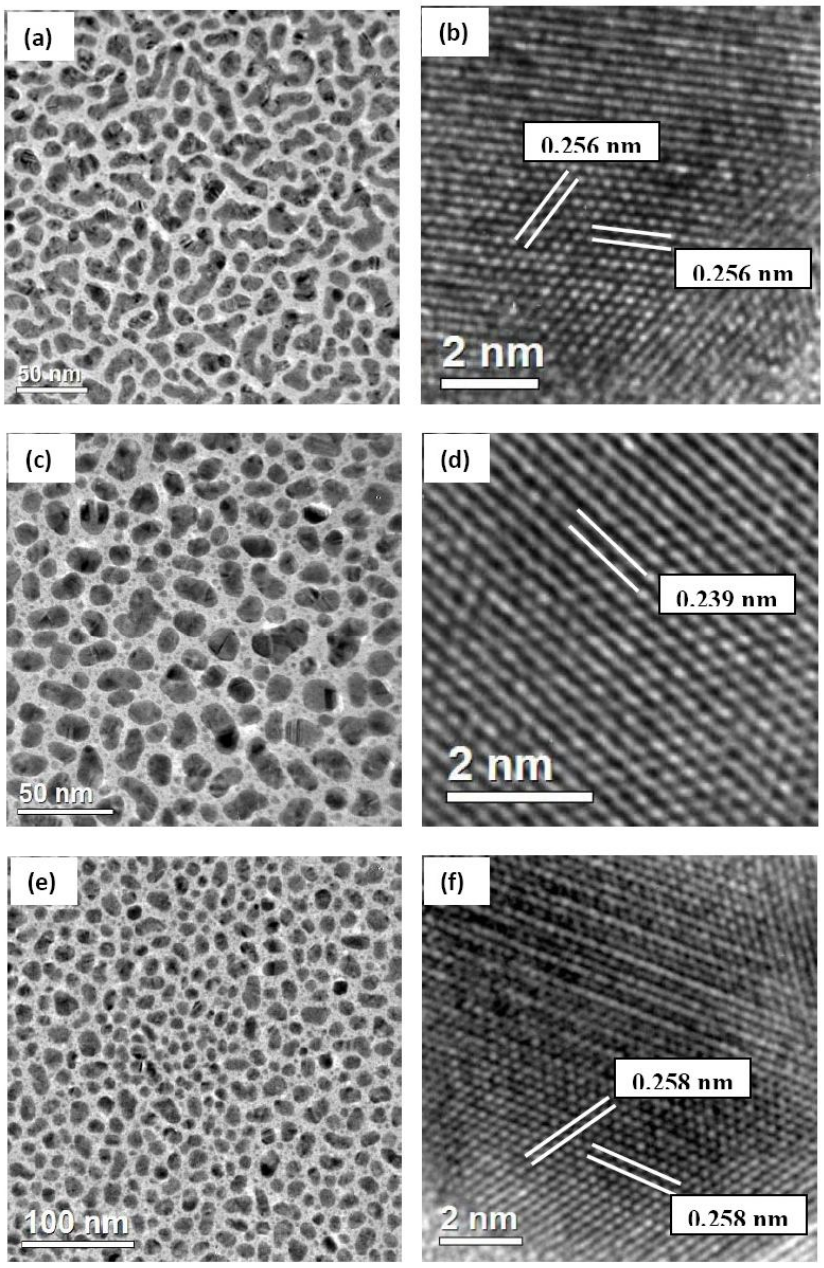

Fig.3.10. TEM images of Au films and corresponding high resolution lattice fringes are shown, (a)–(b) at RT, (c)-(d) at 200°C and (e)-(f) at300°C, for 25 min at 450 eV.

The effect of increasing duration of deposition on the microstructure of gold nano particles, at a fixed substrate temperature of 300^{o}C is shown in Fig.3.11. It is evident from the micrographs that the nanoparticles in these films have mean grain size of 7-10 nm for a deposition time of 5 minutes as seen in the fig.3.11(a), which decreases to 3-5 nm for deposition time of 10 minutes (fig. 3.11(b)) and remains constant at that size for deposition time of 15 minutes (fig 3.11(c)). Here again the island density increases with increase in duration of deposition, but the fragmentation is accompanied by decrease in inter-island distance.

It is evident from these figures that in the initial stages of growth of the Ag and Au films there is a decrease in particles/island sizes that we term as "abnormal coalescence" referring to the fact that there is coalescence but the size of the aggregates decreases instead of increasing. To investigate the origin of this behavior, films were also grown on BSG substrates (placed next to the CCG substrates) under the same deposition conditions. The effect of changing the substrate from CCG to BSG on the coalescence behaviour of the Ag and Au films is presented here. During the same deposition run in which the films were deposited on CCG, films were also deposited on to BSG substrates. The microstructure was examined using an atomic force microscope so that the films do not have to be removed from the substrate and hence the role of the substrate is still evident. The AFM images of silver films deposited on to BSG substrates maintained at ambient temperature, 200 and 300^{o}C, respectively are shown in fig.3.12.(a), (b) and (c) respectively. It is clear that, at all temperatures, the films are continuous and there is no evidence for islands. The mean particle size was between 40-60 nm.

The surface roughness of these films is plotted in fig.3.13. (a) to (c) and it is evident that the average surface roughness is of the order of 0.2 to 1.0nm and the peak to valley height is of the order of 2 nm in all three cases, with no specific dependence on substrate temperature. It may be noted that the rms roughness values were <1nm for BSG while it was between 20-25 nm for the CCG substrates.

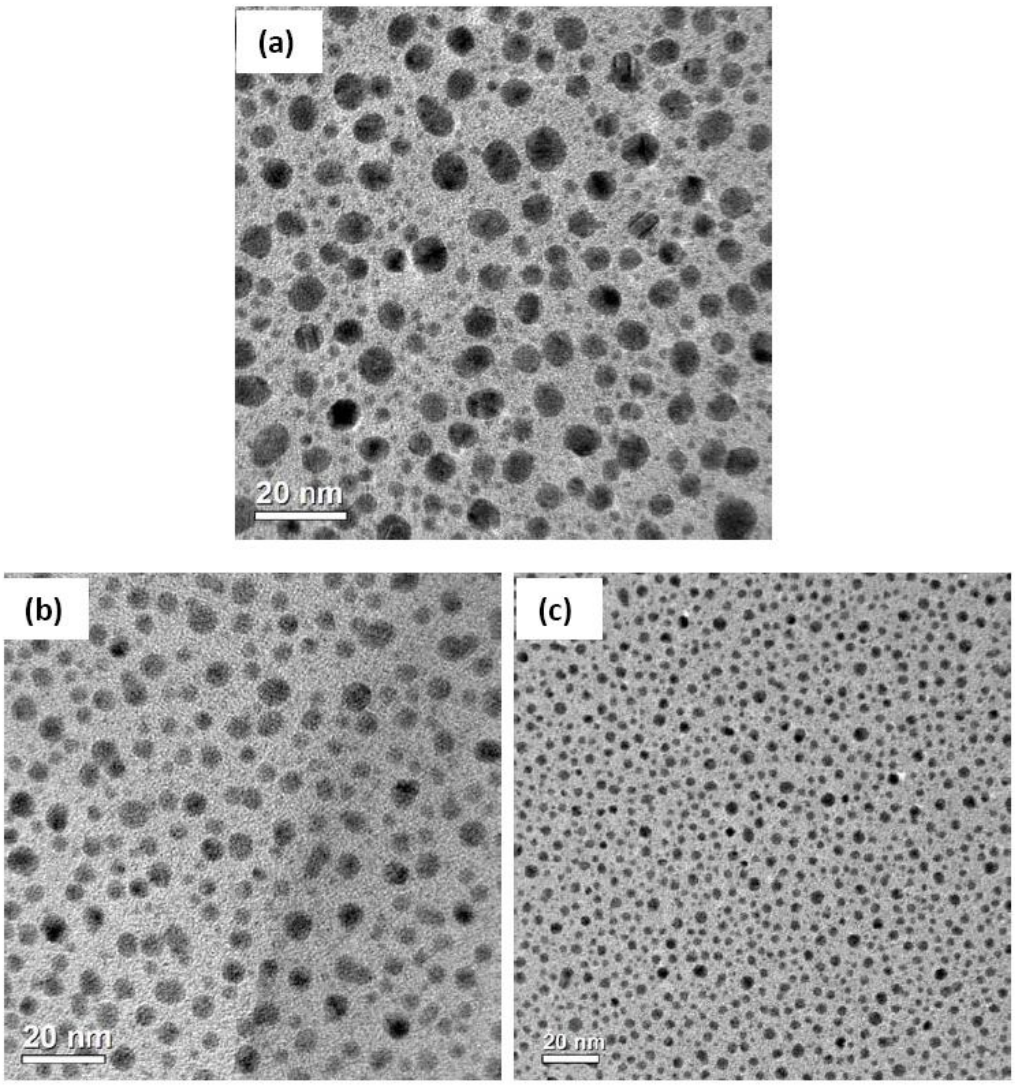

Fig.3.11. Bright field TEM images of Au films deposited at 300°C under various deposition time, (a) for 5 min (b) 10 min and (c) 15min, at 450 eV.

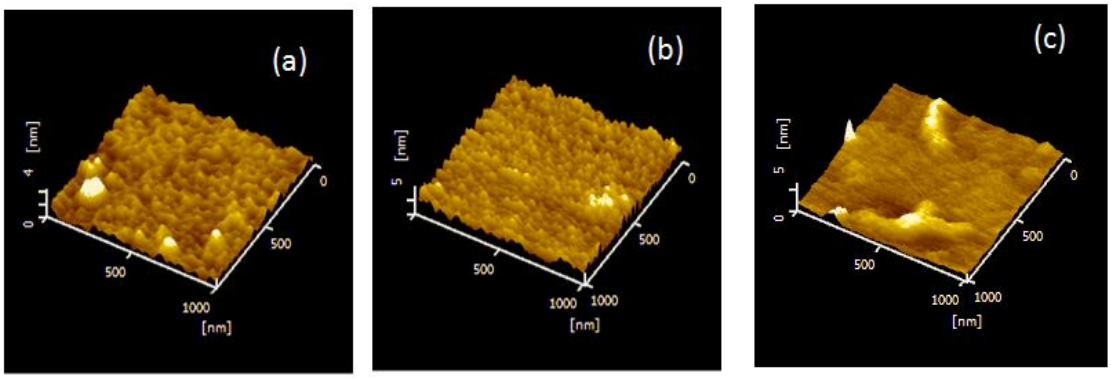

Fig.3.12. AFM images of Ag films deposited on BSG substrates at (a) room temperature, (b) 200 and (c) 300°C.

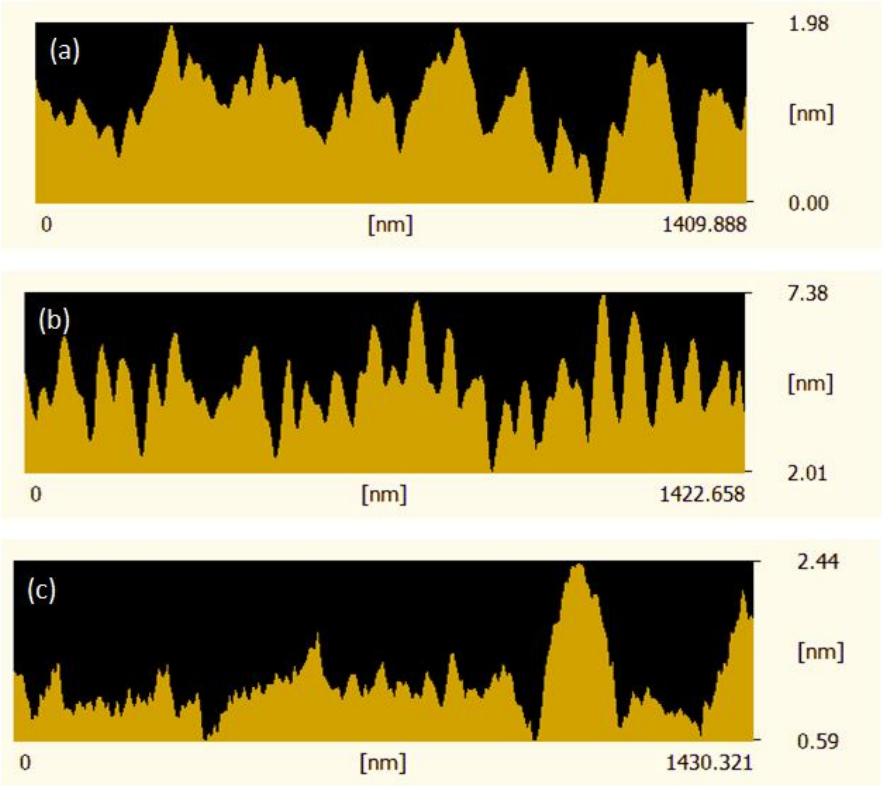

Fig.3.13. Roughness profiles of the Ag films deposited on BSG substrates at (a) ambient, (b) 200 and (c) 300°C.

The morphological evolution of Au films deposited on BSG substrates is shown in fig.3.14. (a), (b) and (c) for substrate temperatures of ambient, 200 and 300^{o}C, respectively. As in the case of Ag, the Au films are continuous even at ambient temperature and remain continuous at higher temperatures. At ambient temperature the particles are of the order of 20- 40 nm in diameter which increases to 50 to 70 nm at higher temperatures indicate coarsening of the grains. The particles also acquire elongated shapes at higher temperatures. The surface roughness of these films is plotted in figs.3.15. (a) to (c) from which it can be inferred that the average surface roughness is of the order of 1-2 nm and the peak-to-valley height is of the order of 2-3 nm, as in the case of Ag films.

The microstructural evolution on BSG is in contrast to that observed for the Ag and Au films deposited on CCG substrates. Even at the lowest temperatures and thickness the films are continuous and do not exhibit any evidence of islands or particulate growth. In both cases there is coarsening of particles with increase in temperature without much change in the surface roughness.

Several patterns of morphological evolution emerge, based on the results presented in figs 3.9 to 3.15. The first of these relates to the differences arising out of the different film materials deposited on the same substrate. It is thus expected that the morphological evolution of Ag on CCG will be different from that of Au on CCG and similarly on BSG. On both substrates Ag particles are more spherical than the Au particles that grow in the form of elongated ellipsoidal shapes. This difference can be explained using the free energy balance equation leading to Volmer-Weber type of growth [27-32].

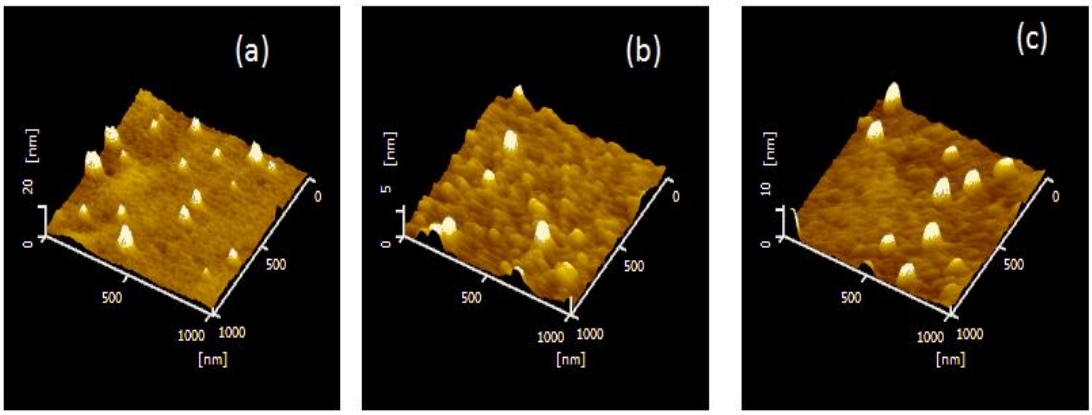

Fig.3.14. AFM images of Ag films deposited on BSG substrates at (a) room temperature, (b) 200 and (c) 300^{o}C.

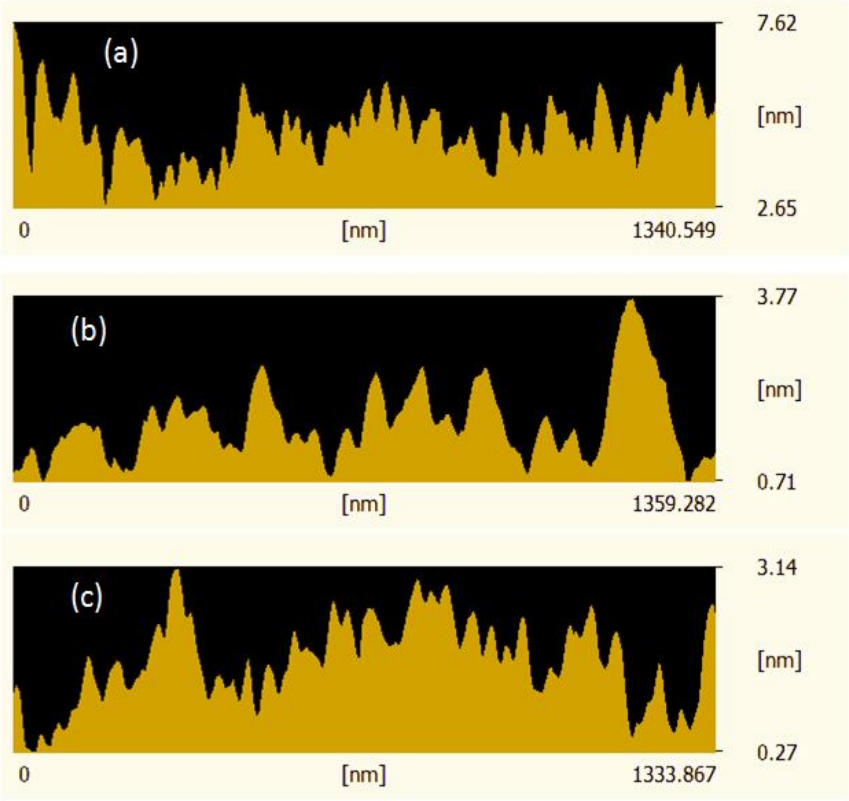

Fig.3.15. Roughness profiles of the Au films deposited on BSG substrates at (a) room temperature, (b) 200 and (c) 300^{o}C.

Three types of growth modes are observed, in general, for thin films deposited on substrates. These modes of growth named, Stranski,-Krastanov, Volmer-Weber and Van der Merwe, originate from the free energy balance between the free energies of the substrate surface γ_s, the free energy of the film surface, γ_f and the interface between the film and substrate γ_i. In addition to these contributions the contact angle θ between the film and substrate is also very important. The free energy balance can be expressed as

$$\gamma_s = \gamma_i + \gamma_f \cos\theta \qquad (3.13)$$

Some materials have a negative enthalpy of mixing with one another--they are miscible. These materials tend to mix strongly at the film substrate interface to give a film-substrate "interface width" that may extend over many atomic layers. Volmer-Weber type of growth leads to 3D islands since the film does not "wet" the substrate and the "interface width" of the growing surface increases with time.

This is manifested in eqn.(3.13) in the term $\cos\theta$ which defines the strength of the contribution of the vapour-solid contact angle to the growth of the film. It is evident from the microstructural evidence presented that the contact angle of Au is smaller than that for Ag on both CCG and BSG. For large contact angles the interface contribution dominates over that of the film surface free energy. Small contact angles also translate into better wettability of the substrate by the film material. Thus, wettability of Au on these surfaces is higher leading to elongated ellipsoidal shapes. The Ag-CCG/BSG contact angle is higher leading to more spherical shaped particles.

At a temperature, T, the growth of film is characterized by the diffusivity of adatoms, D_a on the substrate surface. It is known that the D_a has an exponential dependence on temperature that can be expressed as

$$D_a = D_s \exp(-E_a/kT) \qquad (3.14)$$

Where D_s is a pre-exponential factor and E_a is the activation energy for surface diffusion. The average grain size at impingement, $r_{i,}$ is defined as

$$r_i = (A/\pi)^{1/2} \qquad (3.15)$$

where A is the average in-plane area which depends on the relative rates of island nucleation and growth. The growth rate is also dependent on the distance, δ, over which atoms adsorbed on the substrate surface can diffuse to a growing island. This, in turn, depends on the adatom diffusivity on the substrate surface, D_a. Once islands have coalesced, further film thickening generally occurs by further growth of existing crystals rather than nucleation of new islands.

The increase in particle/grain size of Ag and Au films on BSG substrates follows the normal pattern of coarsening expected, as a function of increasing thickness and temperature.

The models discussed above successfully describe the growth of thin films on smooth, flat and planar substrates and the behaviour is referred to (in this work) as "normal coalescence". Normal coalescence indicates grain coarsening as a function of increasing temperature and thickness of films, in the early stages of growth. These models, however, do not take into account the roughness of substrates and are therefore unable to predict its effect on film growth. The effect of substrate roughness on the roughness of films grown on such surfaces has been reported by a few workers. Anders *et al.* [22] have investigated nucleation and coalescence of silver islands on glass by in situ measurements of the sheet resistance. Sub monolayer amounts of niobium and other transition metals were deposited prior to the deposition of silver. It was found that in some cases, the transition metals lead to coalescence of silver at nominally thinner films with smoother topology. The smoothing or roughening effects by the presence of the transition metal was explained by kinetically limited transition metal islands growth and oxidation, followed by defect dominated nucleation of silver. Gyure *et al.* [23] presented experimental data for the morphological evolution of InAs buffer layers which are interpreted using continuum equations of motion and kinetic Monte Carlo simulations. They observe the formation of mounds in the early stages of growth and the presence of an instability even as an initially rough surface smoothens during growth. This instability is claimed to be due to the step-edge barrier which causes a characteristic length to emerge while the surface roughness is decreasing, well before the formation of the mounds. Coluci and Cotta [24] have carried out a similar Monte Carlo simulation of the morphology evolution of films grown on rough substrates. The surfaces considered for the simulation are similar to those of substrates used for the growth of GaAs films by chemical and molecular beam epitaxy.

When the growth is simulated, decreasing film roughness is observed until a stable value is reached. During this decrease the formation of mound like structures of a few monolayers in height was observed. In some conditions the structures forming the initial rough surface present a limitation to the lateral size of these mounds. Significantly, their study predicts a surface roughness dependent size limitation but it has not been quantified. Another significant work was reported by Mathur and Erlebacher [25] who investigated the growth of thin (1–10 nm) films of Pt on Au(111). It was found that on flat Au(111), Pt grows in a layer-by-layer growth mode, but if the gold substrate is exposed to an acidic environment prior to Pt deposition, then the substrate becomes nanoscopically rough (islanded) and Pt growth follows a pseudo-Stranski–Krastanov (SK) growth mode in which an initially thin wetting layer becomes rougher with increasing film thickness. An analysis of curvature effects on epitaxial growth mode shows that thermodynamic curvature effects involving surface stress are negligible for the Pt/Au(111) system. Rather, the apparent SK growth is linked to kinetic effects associated with inhomogeneous in-plane elastic relaxation of Pt films on rough surfaces that drive Pt atoms from pits to the tops of islands in the early stages of growth. They observe that mean island height initially increases and subsequently decreases in early growth (*i.e.*, up to 4 nm film thickness) and mean island spacing remains initially constant and subsequently increases (beyond 2 nm film thickness).

The evolution of the interface width has been analyzed experimentally and numerically by Qi *et al.* [21, 26] in their work on film growth on non-planar substrates. Interestingly they report on the growth of ZrO_2 films deposited on to BK7 glass substrates of roughness 0.4 nm by ion beam sputter deposition. The films were deposited for durations ranging from 10 to 150 min at a deposition rate of 1nm/min which is the upper limit of rates of deposition used in the current study. The authors show that the early stages of growth can be characterized by three main quantities; (1) the height-height correlation function determined as a function of lateral position, r and deposition time, t (2) The interface width, w which is a measure of the interfacial roughness and (3) lateral correlation length, ξ which is defined as the largest distance in which the height of particles is still correlated. They find that the interface width goes through a minimum and the lateral correlation length goes through a maximum in the initial stages of growth, i.e for low deposition times.

Galdikas [20] has done detailed modeling of early stages of thin film formation on rough substrate surfaces using a phenomenological model. The author has introduced surface potential dependent sticking coefficients to allow for substrate roughness. The kinetics of the three main characteristics: surface coverage, island density and average island size are analyzed. From the theoretical investigation it is found that the shape of the kinetic curves qualitatively differ for 2D and 3D island growth mode. The island density at any instant of time is given by the expression

$$\frac{dn}{dt} = \frac{1}{2}\alpha_{AA} i_0 (\varphi_s + a(t)\varphi_s^*) + \alpha_{col} C_{col} \left(1 - \varphi_C - \varphi_\beta\right) \qquad (3.16)$$

The calculated dependence of the total amount of deposited material on deposition time was normalized to the number of fully covered monolayer (equivalent thickness) for different ratios of parameters α_{A0}, α_{AC} and α_{AT}, *i.e.* for different film growth mechanisms. The surface coverage by islands increases when (1) the arriving atom sticks at the already existing single adatom with probability (or sticking coefficient) α_{AA} and or (2) it sticks at the edge of already existing island with probability α_{AC}. Surface coverage, initially is therefore completely dependent on sticking coefficients which are in turn dependent on substrate roughness.

The other parameters of relevance to the current work are the island size and density. The process of island migration was described by a parameter β, which is defined as the radius of circle within which the mass center of island mass can move. At higher values of β the coalescence (mobility coalescence) occurs at lower values of surface coverage. The island density also depends strongly on the parameter λ, which represents the diffusion length of adatoms. With increase in the parameter λ, the number of islands decreases and the size of islands increases, because more adatoms can reach and stick at the existing islands. The author has made a very detailed analysis of the kinetics of island size and densities, but only relevant portions are discussed here. The calculated kinetics of island densities revealed that, for fixed value of β, the island density is constant over a large range of deposition times and decreases drastically thereafter. In contrast for small value of, λ, there is a very sharp initial increase in the island density followed by an exponential decrease beyond a critical deposition time. Similar analysis of the dependence of island size on β for fixed λ values shows that for low β values there is an initial increase in

island density beyond which it remains constant. The island density then decreases only for very long durations of deposition (in this case > 1200 s). As the β values increases the duration for which the island density remains constant decreases presumably due to increased surface diffusivity.

The temperature dependence of β has been expressed in the following equation

$$\beta(t) = \beta_o \exp(-Z(t)/Z_{max}) \qquad (3.17)$$

where β_o is the pre-exponential factor, Z(t) is the ratio of the surface coverage $\varphi_c(t)$ with islands at a time t to the relative number of islands n(t) on the surface at the same time t. Z_{max} is the maximum island size at which it becomes immobile, or two islands touch each other. It can be shown from this equation that for small values of t there will be an initial decrease in diameter of the clusters before it reaches a critical size beyond which it will increase. This is due to the decrease in island density at longer durations of deposition.

The phenomenological models developed by Galdikas [20] and Qi *et al.* [21], thus shows that films deposited on rough surfaces exhibit very different kinetics of surface coverage, diffusion and island migration than films deposited on flat substrates. There are two competing processes at the early stages of film growth; desorption and diffusion. A substrate with high roughness can be modeled as having a number of peaks and valleys, like a sinusoidal wave. At peak positions, initially, desorption dominates over the diffusion process leading to either an increase in island density or constant island density up to a critical duration of deposition beyond which the normal dynamic scaling behavior occurs. Hence the films remain discontinuous for larger effective thickness retaining the "memory" of the substrates for larger thickness. The growth on rough substrates can thus be divided into two broad regimes abnormal and normal coalescence. The abnormal coalescence observed in the Ag and Au films deposited on CCG substrates, in the present work, can be explained within the framework of the phenomenological models developed by Galdikas and Qi *et al.* [20,21,26]. Evidently, surface coverage is limited by roughness of the substrates which decreases the sticking coefficients. These and other earlier reports of film deposition on rough substrates have focused solely on smoothening of films grown on such substrates and decreasing the island density to form continuous films. In

the present work it is demonstrated that substrate roughness can also be used to control shape and size of nanoclusters in the early stages of thin film growth making it a viable technique for the fabrication of nanostructured thin films.

3.6. Summary

In summary, the growth process of metal thin films (Ag and Au) by ion beam sputter deposition (IBSD) technique is studied. It is found that the IBSD offers very fine control over growth of the films compared to DC sputtering and thermal evaporation technique. It is observed that IBSD offers a great degree of control over the size, shape and interparticle spacing in the nanostructures and nanostructured films. The films growth is discontinuous at low ion energy deposition and become island like and continuous with the increase of deposition time or rate of deposition. This process of growth is very well explained by the theory of growth and nucleation.

A variety of nanostructures such as non-regular array of nanoparticles, nanoneedles and nanoclusters have been realized. Discontinuous Ag and Au thin films were grown on different substrate by IBSD. Two distinct regimes of coalescence are observed depending on the substrate roughness. Normal coalescence, defined as the regime where grain coarsening as a function of increasing deposition duration and temperature occurs, is observed on smooth BSG substrates. Abnormal coalescence defined as the regime where the cluster sizes decrease as a function of increasing deposition duration and temperature occurs, is observed on rough CCG substrates.

References

1. D.M. Tennant and A.R. Bleier, in Comprehensive Nanoscience and Technology (Elsevier) **4** (2011) 35.
2. T. Balla, S M Spearing and A. Monk, J. Phys. D: Appl. Phys. **41** (2008) 174001.
3. K. Gamo**,** Nucl. Instrum. Meth.B, **121** (1997) 464.
4. M G Krishna and P. Kumar, in Emerging Nanotechnologies for manufacturing ed. Jackson M and Ahmed W (Elsevier) **93** (2010).
5. C. Didiot, S. Pons, B. Kierren, Y. Fagot-Revurat and D. Malterre, Nat. Nanotech., **2** (2007) 617.
6. C. N. R. Rao, V V Agrawal, K Biswas, K. G. Ujjal, M Ghosh, A. Govindaraj, G. U. Kulkarni, K. P. Kalyanikutty, K. Sardar and S. R. C. Vivekchand, Pure Appl. Chem., **78** (2006) 1619.
7. O Masala and R Seshadri, Annu. Rev. Mater. Res. **34** (2004) 41.
8. E Y Zhang and C R Wang**,** Curr. Opin. Coll. Interf. Sci., **14 (**2009) 148.
9. J. Stangl, V. Holý, G. Bauer, Rev. Mod. Phys., **76** (2004) 725.
10. A. R. Woll, P. Rugheimer and M. G. Lagally, Mater. Sci. and Eng. B**, 96 (2002) 94.**
11. L. Maissel and R. Glang, in Handbook of Thin film technology (McGrawHill) 1970.
12. D. Walton, T. N. Rhodin and R. W. Rollins, J. Chem. Phys. **38** (1963) 2698.
13. J. A. Venables, Surf. Sci. **299/300** (1994) 798.
14. R. M. German, Powder Metallurgy Science. Metal Powder Industries Federation, Princeton, NJ, 1984.
15. J. G. Jackson, R. W. Fonseca and J. A. Holcombe, Spectrochimica Acta Part B **50** (1995) 1837 – 1846.
16. H. Xu and K. Y. S. Ng, J. Vacuu. Sci. and Technol. B, **15**, Issue 2, (1997) 186-191.
17. D. Kashchiev, Surf. Sci. **86** (1979) 14.
18. M. Avrami, J. Chem. Phys. **7** (1937) 1103; **8** (1940) 212; **6** (1941) 177.
19. D. G. Stearns, Appl. Phys. Lett. **62** (1993) 1745.
20. A. Galdikas, Thin Solid Films, **418** (2002) 112-118.
21. H. J. Qi, J. D. Shao, D. P. Zhang, K. Yi, Z. X. Fan, Appl. Surf. Sci. **249** (2005) 85-90.

22. A. Anders E. Byon, D-H Kim, K Fukuda, S H.N. Lim, Solid State Commun. **140** (2006) 225–229.
23. M F. Gyure, J J. Zinck, C Ratsch, and D D. Vvedensky, Phys Rev Lett, **81** (2000) 4931.
24. V.R. Coluci and M.A.Cotta Phys Rev B **61** (2000)13703.
25. A. Mathur and J. Erlebacher Surface Science **602** (2008) 2863–2875
26. H J Qi, L.H. Huang , Z.S. Tang , C.F. Cheng , J.D. Shao , Z.X. Fan Thin Solid Films **444** (2003) 146.
27. C Ratsch and J A Venables, J. Vac. Sci. Technol.A, **21** (2003) S96.
28. N. Israeli and D. Kandel, Phys. Rev. Lett. **88** (2002) 116103.
29. H.J. Frost, C.V. Thompson and D.T. Walton Acta Metallurgica et Materialia **38** (1990) 1455-1462
30. C V Thompson, Annu. Rev. Mater. Sci.**20** (1990) 245-68.
31. T. P. Nolan, R. Sinclair and R Beyers, J. Appl. Phys. **71** (1992) 720.
32. M. Hu, S Noda, and H Komiyama, J. Appl. Phys., **93** (2003) 9336.

Chapter IV: Optical response of single layer metal thin films

Abstract

Metal thin films have very interesting optical properties in nano-scale range. This chapter presents the optical response of single layer Ag and Au thin films. The possibility of tuning Surface Plasmon Resonance (SPR) by controlling the particle size and shape by the deposition process is investigated. It is observed that the SPR peak of Ag films shifts towards the longer wavelength depending on the particle shape and size and splitting in SPR peak is also observed for different shape and size of nanoparticles. Similar behaviour of optical response is observed in the case of Au thin films. The plasmon resonance shifts towards red with the increase of thickness of the film. However, optical behaviour is different in the case of deposition at different temperature. Ag and Au films deposited at different temperature for fixed time shows blue shift in the plasmon resonance with increase in substrate temperature. The observed blue-shift is a consequence of the decreasing particle size with increase in substrate temperature. The optical behavior of the films deposited at a fixed substrate temperature of 300^{o}C but varying durations of deposition is very different. In this case, SPR peak shifts towards red with the increase of deposition time. This is due to the increase in particle size and thickness of the film. Detailed simulations have been carried out based on Maxwell Garnett theory to distinguish the effects of shape and size on plasmon resonances. This study shows the ability to tune the surface plasmon resonance by controlling the particle size and shape during deposition by IBSD technique with its wide range of control parameters.

Chapter IV: Optical response of single layer metal thin films

4. Introduction

In recent years, interest in thin film metal nanostructures has increased due to their unique optical properties and potential applications which include ultrafast optical switches, optical tweezers, labels for biomolecules, optical filters, biosensors, surface enhanced spectroscopies, plasmonics and chemical sensors [1, 2]. The most important requirement of these applications is control of size and shape of the metal nanoparticles. These metal nanoparticles exhibit local surface plasmon resonance (SPR) by interaction of incident electromagnetic radiation with surface electrons. The ability to tune the SPR wavelength for various applications is also an essential consideration. Among all the metals, Ag and Au have attracted much interest for several decades due to their SPR in the visible region of the spectrum [3-6].

In the present study, thin films of Ag and Au were deposited by Ion Beam Sputter Deposition (IBSD) technique on to borosilicate glass substrates. The chamber was evacuated to 2 x 10^{-6} Torr and maintained at 4 x 10^{-4} Torr after introducing the Ar gas through during the deposition.

4.1. Optical response of Ag single layer thin films

The optical response of Ag thin films deposited at different Ar ion energies for the same duration of deposition at ambient temperature is first investigated. The purpose of this is to see the effect of ion energy on the optical response of the Ag thin films. Fig. 4.1 shows the absorption spectrum of Ag thin films deposited at different ion energy for the duration of 15 minutes deposition time. The deposition is reported in terms of duration of deposition time instead of mentioning thickness since the films were discontinuous in majority of the cases. The ion energy *vs* rate of deposition plot is shown in the previous chapter III (fig.3.3) in order to estimate the thickness of the films.

It is observed that the absorption spectra are red shifted with the increase of thickness of the Ag films which is due to the increase in ion energy at the deposition. The peak is due to the surface plasmon resonance (SPR) of Ag. It is observed that initially the absorption peak was at 382 nm for the deposition energy of 150 eV and shifted to 440 nm for 200 eV and 450 nm for 250 eV Ar ion energy. The absorption peak shifted up to 682 nm for the film deposited at 600 eV along with broadening in width with the increase in ion energy at the deposition. It may be recalled that increase in ion energy causes increase in rate of deposition as well as thickness of the films. The films deposited at 600 eV are 62 nm thick, densely packed and continuous films. These films would, therefore, display very broad plasmon resonances. The films deposited at 150 eV, on the other hand, are only 18 nm thick and discontinuous in nature. These films should display sharper plasmon resonances as expected. The fig.4.2 shows the absorption peak variation with the increase in ion energy. It is observed that the plasmon resonance peak red-shifts with the increase of ion energy. The peak positions compare very favorably with those reported by other workers. Martens *et al.* [5] have reported on two dimensional silver nanoparticle arrays in silicon. They observed that increase in Ag deposition thickness leads to larger shape anisotropy and thus larger plasmon red shift. Sonnichesen *et al.* [7] reposted on the variation of plasmon peaks with the increase of cluster sizes of gold and silver. Noguez [8] reported on the influence of the shape and the physical environment on gold and silver nanoparticles on surface plasmon resonance and noted that there is a red shift in the plasmon resonance peak with increase in grain size. Lee *et al*. [9] have studied the effect of the sized silver (Ag) nanoparticles on the optical property of surface plasmon resonance. They have prepared the Ag nanoparticles on fluorine-doped-tin-oxide (FTO) coated glass substrates by RF magnetron sputtering with various deposition times and the subsequent rapid thermal annealing (RTA) to control the particle size. Ag films of different thicknesses were first deposited on either glass or FTO substrate by a vacuum sputtering technique. Some of the samples founded nanoparticles by rapid thermal annealing. The substrate with and without nanoparticles were then sensitized by immersing them in a 0.2 mM N719 dye solution and they investigated the absorption coefficient by adsorbing it on fine Ag islands. The surface plasmon resonance enhanced the absorption by the sample with Ag nanoparticles above that of the sample without nanoparticles. They have found that the peak position of the surface plasmon characteristic absorption increased with the grain size of the nanoparticles in a red-shift

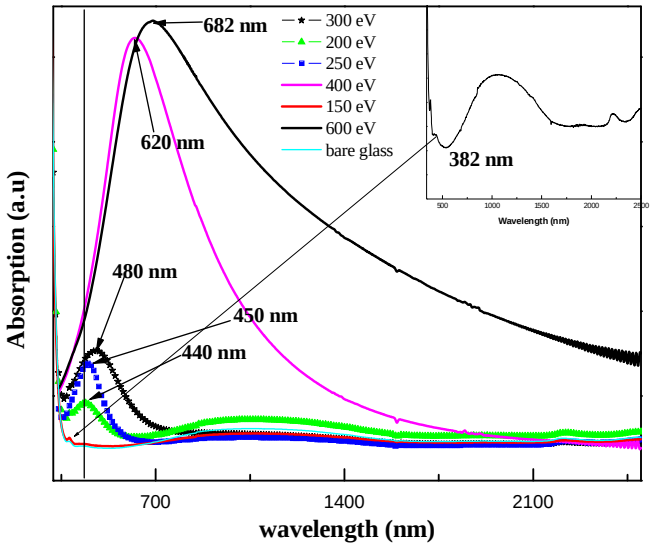

Fig.4.1. Optical absorption spectrum of ion beam sputter deposited Ag thin films at different Ar ion energy for 15 minutes.

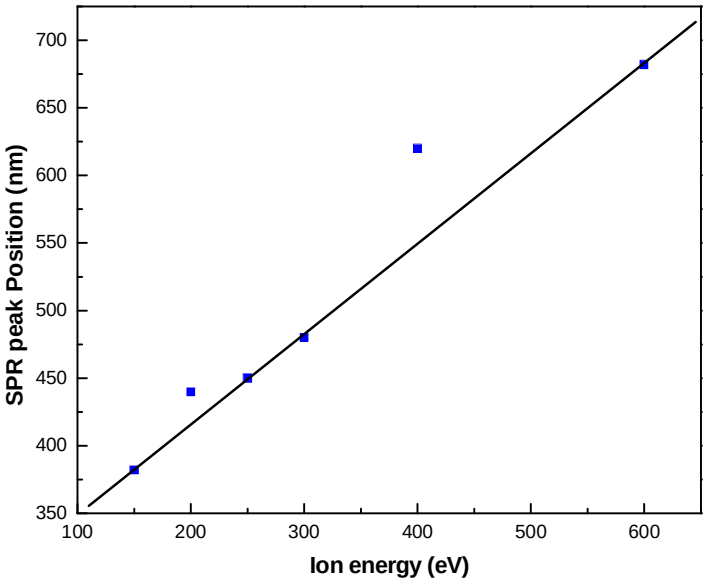

Fig.4.2. Plot of ion energy Vs SPR peak position.

and also observed that the structure and the quantity of Ag particles were very critical to the surface plasmon resonance effect. Gnanavel *et al.* [10] have discussed on optical absorption behaviour of nanostructured Ag films 2, 5 and 10 nm thick obtained by thermal evaporation. They observed that all films are quasi-amorphous and 2 nm thick films exhibit nanotriangles in the nature of Mie particles which exhibit surface plasmon resonance (SPR). They found that the increase of thickness produces a shape change from nanotriangle to spherical triangle and a red shift in SPR. They also observed that the systematic iodization throws up a quasi-particle transition namely plasmon-exciton transition even as Ag metal film is converted into an insulating/semiconducting AgI film. Thus, the above observed behaviour of surface plasmon resonance peak shifting towards red shift and increase in width is due to the increase in thickness of the Ag films with the increase of the ion energy at the deposition. Singh et al have shown how the LSPR of a silver nanoplatelet colloid can be fine-tuned towards the blue by a controlled exposure to a femtosecond laser of appropriate fluence. The achieved a blue shift of 40 nm with a laser wavelength (800 nm) on the red side of the LSPR (600 nm). This shift can be increased further by using a laser of shorter wavelength. The laser irradiation induces a reshaping of the particle around the tips and the edges. This changes the aspect ratio (diameter to thickness ratio) which causes the observed blue shift. They have done numerical calculations using a model of increasingly truncated nanoplatelets that supported their results. This controlled tuning of LSPR peak increases the usefulness of nanoparticles for different applications. They have also shown that the stability of the nanoplatelets against irradiation at moderate intensities can be increased by adding PVP to the colloidal solution. The PVP molecules attach to the plane constituting the tips and suppress the process of tip reshaping [11]. Tilaki *et al.* have studied the effects of the surrounding liquid environment on the size and optical properties of silver nanoparticles prepared by laser ablation by a pulsed Nd:YAG laser operated at 1064 nm. The silver targets used were kept in acetone, water and ethanol. They observed that nano silver in acetone showed a narrow size distribution with a mean size of 5 nm and the colloidal solution was stable. In deinonised waster a rather narrow size distribution with a mean size of 13 nm was observed and nanoparticles were precipitated slowly after about two weeks. They observed a broadening in size distribution and optical extinction spectra in ethanol. Silver nanoparticles in ethanol with a mean size of 22 nm were completely precipitated after 48 h. In acetone, deionised water and ethanol, the wavelengths of

maximum optical extinction were at 399, 405 and 411 respectively and these are attributed in increasing the size of the nanoparticles [12].

These results clearly indicate that the surface plasmon resonances of single layer Ag films can be tuned from 382 to 682 nm by controlling the ion beam parameters and therefore the microstructure of the films. The resonances are broad due to the large width of particle size distribution, as will be discussed in the following sections.

4.2. Optical response of self organized / ordered nanostructure Ag thin films

The results of the study on the optical response of discontinuous and nanostructured Ag films are now presented. In this case, the Ag self assembled nanostructured thin films were deposited by ion beam sputter deposition (IBSD) at low ion energy 150 eV for which the rate of deposition as low as 0.01 nm/sec was obtained. Experiments were carried out at 150 eV, for deposition times of 10 to 30 mins corresponding to increase in thickness from 6 to 18 nm. The details of rate of deposition as a function of ion energy was discussed in the previous chapter [fig.3.3]. The transition from self organized nanoparticle array to a continuous film occurs by control of these parameters together with the total duration of the deposition. The films were grown on Borosilicate Glass (BSG) substrates that were kept at ambient temperature during deposition. Fig.4.3(a) and fig.4.4(b) shows the optical absorption spectrum of self organized nanostructured Ag thin films deposited at 150 eV ion energy for the duration of different time / thickness. The optical absorption spectrum of the semi-continuous 18 nm film consists of a single peak at 580 nm (curve (iii) in Fig. 4.3(a)) which shifts to 532 nm (curve (ii), Fig. 4.3(a)) for the 15 nm film. In the previous chapter [fig.3.5], it was shown using AFM images that the microstructure in this case consists of elongated islands that are loosely connected. As the thickness is further reduced to 6 nm (curve (i), Fig.4.3(a)) completely discontinuous structures start appearing. This is accompanied by the appearance of two plasmon resonances, one of which occurs at 380 nm and a broad peak centered at 440 nm (as shown in the inset). In the case of the 9 nm thick films (curve (i), Fig. 4.3(b)) there are two resonances one at 380 nm and a weak peak at 425 nm. When the thickness of the film is increased to 12 nm, the absorption peak (curve (ii), Fig. 4.3(b)) at 436 nm becomes strong, while the other resonance is relatively invariant. The self ordered nanostructures are thus characterized by multiple resonances while the continuous films by single

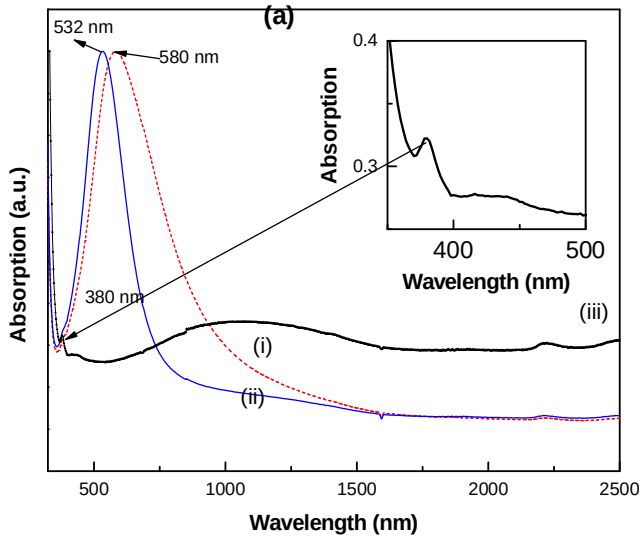

Fig. 4.3(a). Plasmon resonances of the Nanostructured Ag films deposited at an Ar ion energy of 150 eV with a thickness of (i) 18, (ii) 15 and (iii) 6 nm.

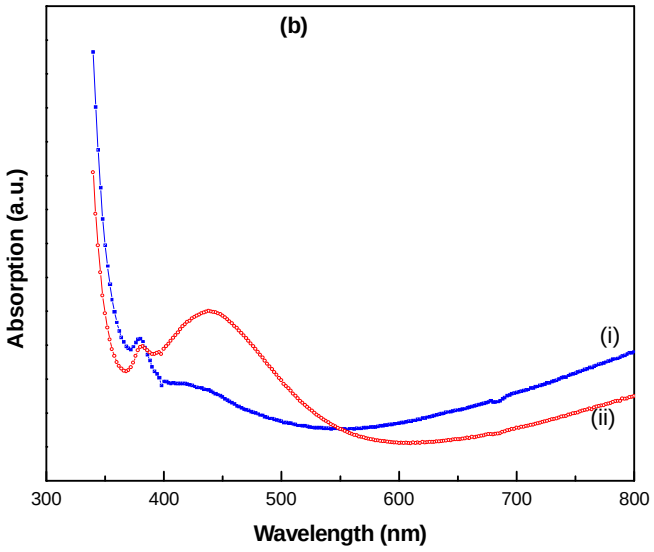

Fig.4.3(b). Plasmon resonances of the Nanostructured Ag films deposited at an Ar ion energy of 150 eV with a thickness of (i) 12, and (ii) 9 nm. The region beyond 900 nm is not shown in this figure since it is dominated by the absorption band of the BSG substrate.

plasmon peaks. It is significant that the transition from multiple resonances to single plasmon resonances is very sharp and tunable by microstructural evolution. The variation in the plasmon resonance peak position and its width is dependent on thickness, packing density of films (discontinuous or continuous) as well their shapes. However, it is difficult experimentally to control and isolate the effect of each of these parameters on the SPR behavior.

4.3. Optical response of Au single layer thin films

Initially, thin films of Au were deposited on borosilicate glass substrates at different ion energies. The ion energy in this case was varied from 250 eV to 450 eV. Fig. 4.4 shows the absorption spectrum of Au films deposited at different ion energies for the deposition time of 30 minutes. The absorption peak for ion energy of 250 eV is observed at a wavelength of 578 nm and 600 nm for 300 eV ion energy. With further increase of the ion energy to 400 eV, the absorption peak is further red-shifted to 648 nm. At an ion energy of 450 eV, the film behaved like a bulk metal with a flat peak centered at 590 nm. It is very clearly observed that the absorption peak shifts towards red with the increase of the ion energy. It is also observed that the width of the peak increases with the increase in ion energy which is observed in the case of Ag thin films.

The shifts in the absorption peak and the increase in the width of the peak can be attributed to the increase in the thickness of the films which is due to the increase in the ion energy. The above results very well agree with the work done by others. Sreeja *et al.* have prepared gold nanoparticles of different sizes by laser ablation of a gold target in deionized water. An increase in the particle size was observed with increasing laser pulse energy and the absorption spectrum was redshifted in wavelength with an increase in the particle size. The optical absorptive nonlinearity of the nanoclusters showed an optical-limiting-type nonlinearity, which finds application in the fabrication of optical-limiting devices. The efficiency of limiting increased with a decrease in the particle size. The nonlinear refraction of the Au nanoclusters showed a negative index value, indicating self-defocusing-type nonlinearity. They observed that both the real and imaginary parts of nonlinear susceptibility increased with a decrease in the particle size, which was attributed to the size-dependent enhancement in the oscillator strength of the nanoparticle. The stable and flexible nonlinear devices were fabricated by incorporating the Au

nanocrystals showing better nonlinearity in a poly vinyl alcohol (PVA) matrix. The enhancement in the nonlinear refractive index for the Au nanocrystals in the polymer matrix as compared to the Au nanocrystals in water was attributed to the thermal effects arising in the solid film [13]. Takeda *et al.* have studied on optical properties of Au nanoparticle composites and a grid structure of Cu nanoparticle composite. Negative ion implantation was applied to synthesize Au and Cu nanoparticles in amorphous SiO_2 and Al_2O_3. Au nanoparticles were embedded within a depth of 30 nm by 60 keV Au^- implantation. The surface plasmon resonance (SPR) of $Au:SiO_2$ and $Au:Al_2O_3$ composites shifted to red and to blue, respectively, compared to calculated ones by the Mie theory. They have measured optical nonlinearity with pump-probe femto second spectroscopy and the transient spectrum of $Au:Al_2O_3$ composite presented a large red shift from the SPR peak. Image mapping of far-field transmitted intensity of Cu-implanted SiO_2 with a fine grid structure drawn by laser-lithography was observed by a scanning near-field optical microscopy (SNOM) system [14]. Neff *et al.* have studied optical properties of very thin gold films evaluated by Fresnel analysis, with optical boundary conditions pertaining to the surface plasmon resonance (SPR) at the gold–water interface and the experimental SPR characteristic was evaluated in the angular interrogation mode. They have characterized the film morphology by high resolution transmission electron microscopy. They observed that the magnitude of the resonance, *i.e.*, the SPR signal, sensitively depends on, and is affected by film thickness and morphology. A sharply defined thickness of 55 ± 5 nm is required, to achieve optimum SPR excitation conditions, and instrumental sensitivity. With decreasing film thickness, below 40 nm, the resonance angle starts to shift to larger values. A substantial increase of the intrinsic resonance broadening parameter is observed below 70 nm, associated with an increasingly asymmetric SPR line shape. They also observed a similar effect occurs in the presence of a very thin chromium adhesion layer. Surface roughness and film thickness modulations determine the experimentally observed line broadening parameter [15].

Fig.4.5. shows the absorption spectrum of Au thin films deposited at 250 eV of ion energy for duration of different time. The absorption peak deposited for the duration of 10 min was found to be at 552 nm which shifted to 560 nm for the deposition time of 15 minutes. It is observed that the peak shifts towards red with the increase of the deposition time. The peak for the deposition time of 25 minutes is at 574 nm which shifts to 584 nm for the deposition duration of 30 minutes. With further increase of deposition time to 35

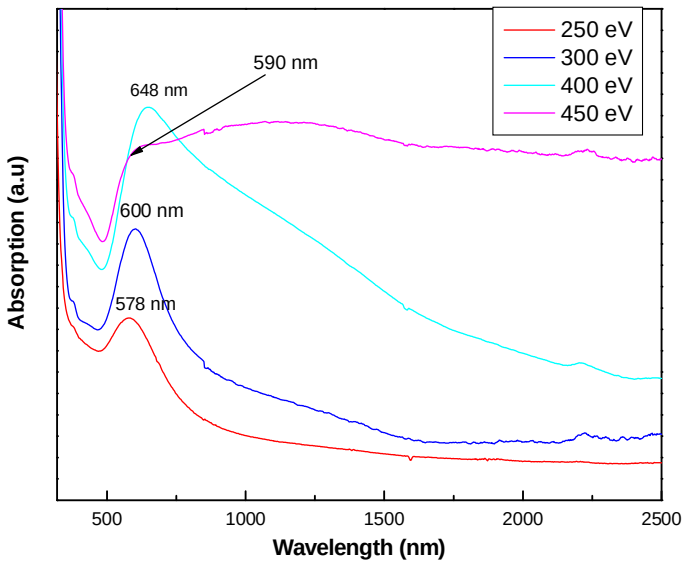

Fig.4.4. Absorption spectrum of Au thin films deposited at 250, 300, 400 and 450 eV for 30 min.

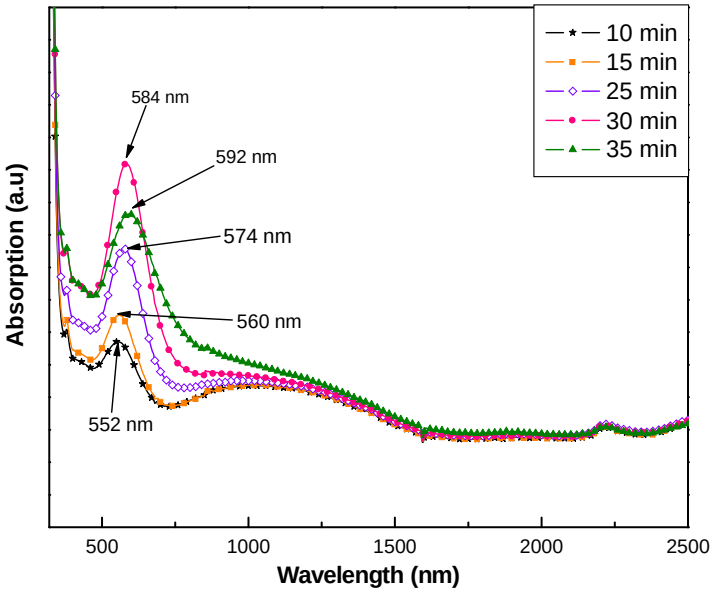

Fig.4.5. Absorption spectrum of Au thin films deposited at 250 eV ion energy for different times.

minutes, this peak was found to shift to 592 nm. The observed behaviour of the spectrum is similar to the case of Ag films. The red shift in the absorption peak is due to the increase in the thickness of the films with the increase of the duration of the deposition time. As the thickness increases the film behaves like a bulk metal in which the volume effects dominate over the surface phenomena and hence surface plasmons are not observed, confirming that SPR is a purely surface and size dependent phenomenon.

4.4. Optical response of Ag and Au single layer thin films deposited at different temperatures

The Ag and Au films were deposited by ion beam sputter deposition at ion energy of 150 eV and 450 eV for Ag and Au respectively. Here, two sets of experiment were done. One set of experiments was carried out on Ag and Au single layer thin films by varying deposition temperature from room temperature to 200^0C and 300^0C at constant deposition time. Another set of experiment was carried out on Au single layer thin films at constant temperature 300^0C but deposition time was varied. Fig.4.6. shows the absorption spectrum of Ag thin films deposited at 150 eV for 40 minutes.

The Ag films exhibit surface plasmon resonance due to their nanoparticle nature, as observed from Fig. 4.6 (a) to (c). At room temperature there is a single plasmon resonance at 452 nm which blue shifts to 424 nm at 200^oC. There is a further blue shift of the primary resonance to 384 nm at 300^oC, with considerable decrease in intensity. The absorption spectra of Au films deposited for a fixed duration of 25 mins at 450 eV argon ion energy and varying substrate temperature is shown in Fig. 4.7. As in the case of the Ag films, there is a blue shift in the Plasmon resonance with increase in substrate temperature. At room temperature the plasmon resonance is observed at 628 nm, which shifts to 610 nm at 200^oC and finally to 600 nm at 300^oC. The position of the SPR peak in nanostructured metal films can shift due to variations in particle size or shape or thickness of films or a combination of these parameters. In the current case although the average particle increases with substrate temperature, presumably their shape also changes leading to a stronger dipole coupling and hence a blue-shift in the SPR peak. The optical behavior of the films deposited at a fixed substrate temperature of 300^oC but varying durations of deposition time is shown in Fig.4.8. It is observed that, for deposition duration of 5 min, the absorption peak occurs at 534 nm. When the deposition time is increased to 10 min., it

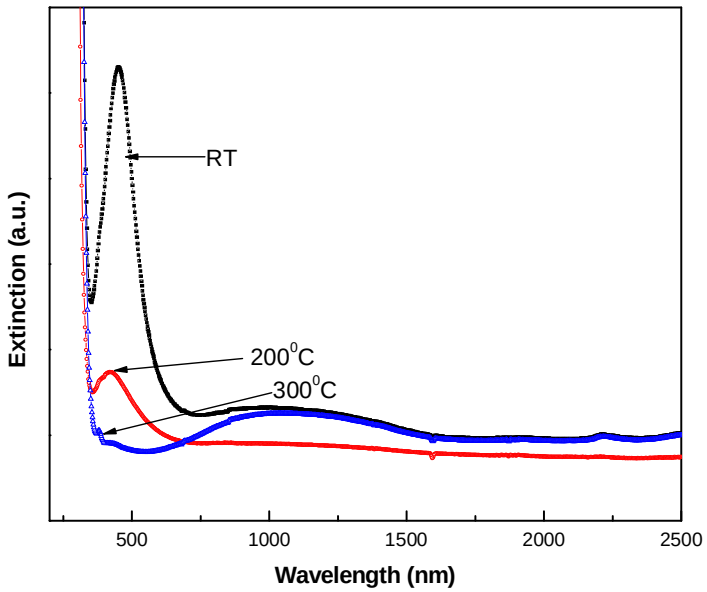

Fig. 4.6. Absorption spectrum of Ag thin films deposited at 150 eV for 40 min. at different temperatures.

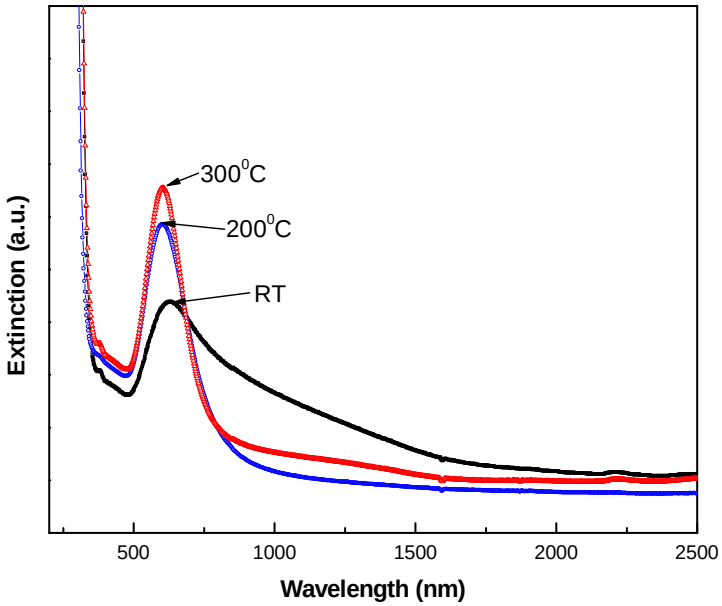

Fig.4.7. Absorption spectrum of Au thin films deposited at 450 eV for 25 min. at different temperatures.

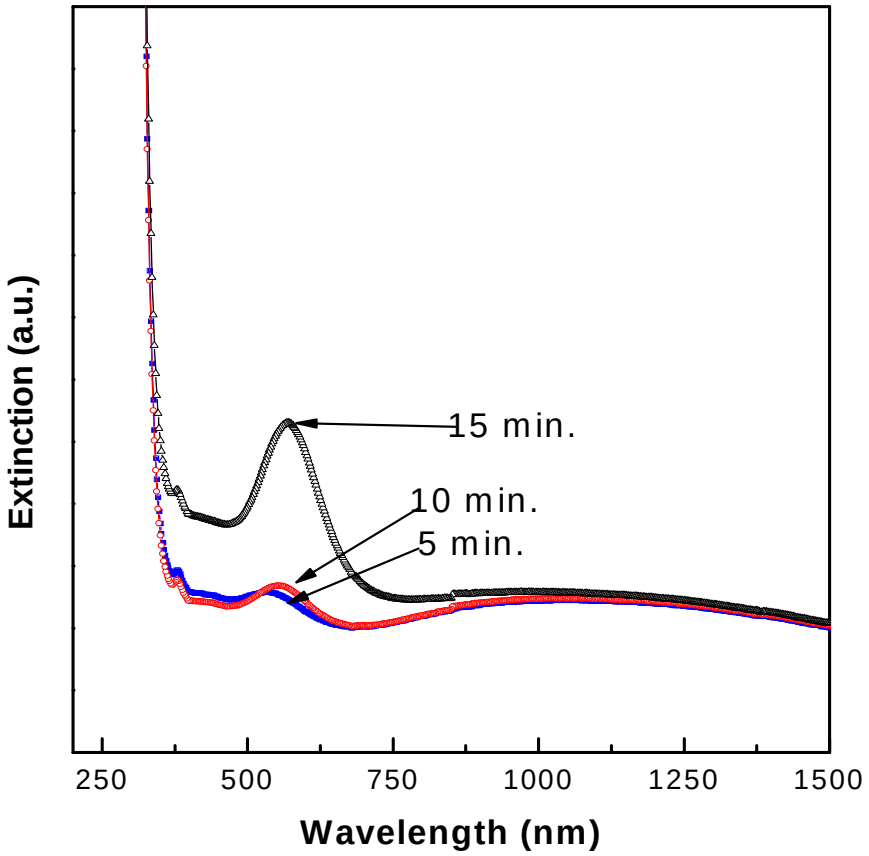

Fig.4.8. Absorption spectrum of Au thin films deposited at 450 eV at 300^0C for different times.

is red shifted to 554 nm and as the deposition time is increased to 15 min., there is a further red shift in the absorption peak to 566 nm. Here, the red shift in the absorption peak is attributed to the increase in thickness with the increase in duration of the deposition time and as well as increase in the grain size as observed from the microstructural studies.

4.5. Simulations of optical response based on Maxwell-Garnett Theory

In order to explain the observed optical behaviour of the nanostructured Ag and Au films, we have chosen the Maxwell-Garnett (M-G) effective medium theory to model the dielectric constant of the composite medium. Consider small spherical particles, each of radius a having a complex dielectric constant ε_m, which are embedded in a host medium of dielectric constant ε_h. The relationship between the effective dielectric constant of the composite medium $\bar{\varepsilon}$, the dielectric constants of the constituent media and the atomic polarizability, calculated from Clausius-Mosotti equation is

$$\frac{\bar{\varepsilon} - \varepsilon_h}{\bar{\varepsilon} + \varepsilon_h} = \frac{f}{a^3}\alpha \qquad (4.1)$$

where α is the particle dipole polarizability, f (= $4\pi/3\ Na^3$) is the volume fraction of the embedded particles and N is the particle number density. For sphere size much smaller than the wavelength of the incident light, the electrostatic value of the polarizability α is given as [16]

$$\alpha = \frac{\varepsilon_m - \varepsilon_h}{\varepsilon_m + 2\varepsilon_h} a^3 \qquad (4.2)$$

Substituting of Eq. (4.2) in Eq. (4.1) and further simplification results in the Maxwell-Garnett formula [16]

$$\frac{\bar{\varepsilon} - \varepsilon_h}{\bar{\varepsilon} + 2\varepsilon_h} = f\,\frac{\varepsilon_m - \varepsilon_h}{\varepsilon_m + 2\varepsilon_h} \qquad (4.3)$$

This formula assumes particles to be spherical in shape. Further generalization to more realistic, non-spherical shapes is desirable, which is done by incorporating an additional parameter into the simple Maxwell-Garnett theory [17] to account for ellipsoidal particles. If the incident electric field is parallel to the principal axis of the ellipsoid of volume V, then its polarizability is given as

$$\alpha = V\frac{\varepsilon_m - \varepsilon_h}{\varepsilon_h + L[\varepsilon_m - \varepsilon_h]} \qquad (4.4)$$

Then the extended Maxwell-Garnett formula [18] for parallely oriented ellipsoids is obtained as

$$\frac{\bar{\varepsilon} - \varepsilon_h}{\varepsilon_h + L[\bar{\varepsilon} - \varepsilon_h]} = \frac{\varepsilon_m - \varepsilon_h}{\varepsilon_m + L[\varepsilon_m - \varepsilon_h]} \qquad (4.5)$$

The above formula is valid when the ellipsoids are all identical in shape and oriented in the same direction, with a depolarization factor L. The expression for the spherical particles (Eq.4.3) can be recovered as a special case of the above by substituting L = 1/3. Further generalization of the above formula to obtain the effective dielectric constant of a composite medium consisting of randomly oriented ellipsoid particles is possible and the formula [19] for the same is

$$(1-f)\frac{\bar{\varepsilon} - \varepsilon_h}{\varepsilon_m - \varepsilon_h} = \frac{f}{3}\sum_{i=1}^{3}\frac{\varepsilon_h}{\varepsilon_h + L_i[\varepsilon_m - \varepsilon_h]} \qquad (4.6)$$

where L_i (i=1, 2, 3) are the depolarization factors along each of the three axes, such that $L_1 + L_2 + L_3 = 1$.

Let the particle size be D and the shape factor be S. Denoting the ellipsoid diameters along x, y and z axis respectively as D_1 , D_2 and D_3 and assuming that the two lower diameters are equal ($D_2 = D_3$), the relation between the particle size and the shape factor can be expressed as [20].

$$D_1 = D(1 + \sqrt{1-S}) \qquad (4.7)$$

$$D_2 = D(1-\sqrt{1-S}) \qquad (4.8)$$

and the depolarization factor L_i is given by

$$L_i = 2D_1D_2D_3\int_0^\infty \frac{du}{(D_i^2+4u)\sqrt{(D_1^2+4u)(D_2^2+4u)(D_3^2+4u)}} \qquad (4.9)$$

4.5.1. Simulation

The surface plasmon spectra are computed as a function of different parameters, viz., the filling factor f, the shape factor S, the particle diameter D and different layer thicknesses and some of the results of the current study are presented in the following.

Fig.4.9. shows the dependence of absorption on the shape factor. It is observed that with decreasing shape factor S (=1 and .992), the resonance is red shifted, together with an increase in the absorption. It may be recalled that S=1 corresponds to spherical particles and all other values of S represent non-spherical shapes. We have observed that for decrease in shape factor, the position of the resonance shifts to the red side, with an associated increase in absorption.

The absorption spectrum of these localized surface plasmons depends strongly on the dielectric constant of embedded particles, which in turn is dependent on the volume filling fraction f. Varying the volume filling fraction of metal nanoparticles embedded in the host medium (air) changes the effective dielectric constant of the composite layer, thus influencing the absorption spectra. In fig.4.10., absorption spectra for different filling fractions are plotted, assuming spherical shaped particles. It is observed that the plasmon resonance is shifted towards longer wavelengths (red shift), as the filling factor is increased from 0.5 to 1.

The oscillating behavior of electrons is governed by the geometry, which is determined by the shape and size of metal particles. In the following analysis, particles of spheroidal shape (prolate or oblate) alone are considered. For prolate spheroids, in which two minor axes are equal, one observes two spectrally separated plasmon resonances (as shown in

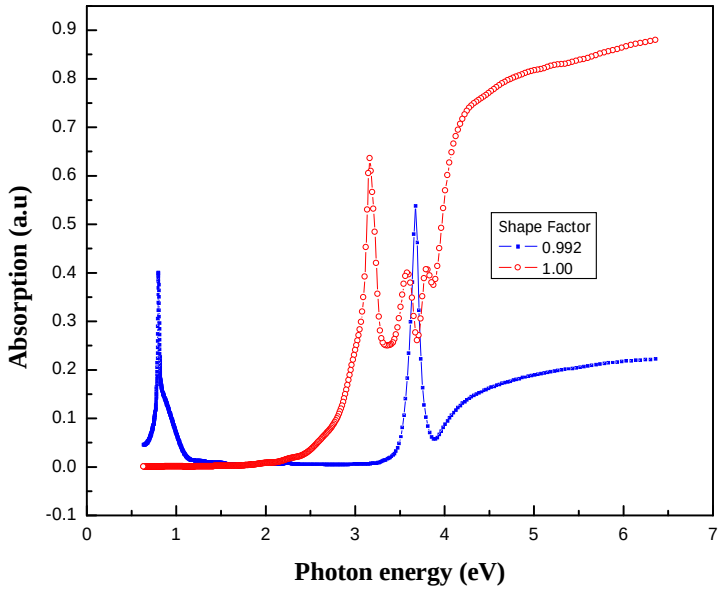

Fig.4.9. Results of simulation showing the effect of varying shape factor on the plasmon resonance behavior for S=1 and 0.992 at constant filling factor.

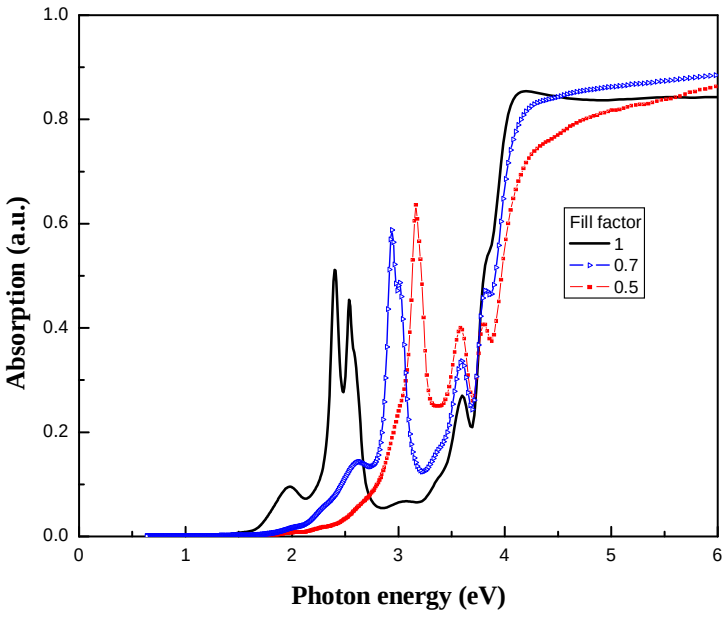

Fig.4.10. Results of simulation showing the effect of varying filling factor on the plasmon resonance behavior for f=1, 0.7 and 0.5 for a constant S=1.

fig.4.4), in contrast to the single resonance for the spherical shaped particles. This resonance position corresponds to the vanishing denominator on the R.H.S. of Eq. (4.5), which results in the relation

$$\varepsilon_h + L_i(\varepsilon_m - \varepsilon_h) = 0 \qquad (4.10)$$

The dielectric constant is given by

$$\varepsilon_h = \varepsilon_m(1 - \frac{1}{L_i}) \qquad (4.11)$$

Assuming the dielectric constant to be purely Drude type without any damping,

$$\varepsilon_h = (1 - \frac{\varpi_p^2}{\varpi^2}) \qquad (4.12)$$

where ϖ_p is the plasma frequency of the free electron. Simplification of the above two equations gives,

$$\varpi^2 = \frac{\varpi_p^2 L_i}{\varepsilon_m + L_i(1 - \varepsilon_m)} \qquad (4.13)$$

For the case where $L_1 < L_2 = L_3$, the plasmon resonance corresponding to L_1 occurs at lower frequencies, while that for L_2 is present at higher frequencies, in contrast to the behavior from the spherical case. Therefore, change in the shape factor from S=1 (spherical) to values of S<1 (spheroidal) results in splitting of the absorption peak, as shown in fig.4.10. The separation between the peaks is a function of the filling factor for a constant S. Significantly, the peak corresponding to oscillations of conduction electrons along the major axis shows a red shift compared to the plasmon resonance of a sphere of same volume.

It is evident from Figs. (4.4) and (4.5) that changing the shape for a constant filling fraction has a stronger influence on the resonance position as compared to the variation in filling fraction for a given shape factor.

4.5.2. Experiment vs. Simulation

A basic absorption experiment consists of the sample under study placed in the path of a light source and a detector. The absorption of the light beam by the sample is then measured by the detector. The theoretically calculated absorption spectra have been fitted to experimental data obtained for silver nanoparticles and these are shown in Figs. 4.11 to 4.14. The nanoparticles were realized in Ag thin films deposited on Borosilicate glass substrates of refractive index ~ 1.5. The mean value of particle diameter in the films was varied from 50 to 200 nm, with a large distribution.

The result of simulation on the bulk property of silver particles, namely the strong absorption in the ultraviolet region (> 4 eV), is in good agreement with the experiment as shown in Fig 4.11. For the particle size D = 0.1 μm and the shape factor S = 0.85, with corresponding depolarization factors $L_1 = 0.1514$, $L_2 = L_3 = 0.4243$ and the volume filling fraction f = 0.2667, the peak position at 2.74 eV of absorption from the simulation coincides with the experimental absorption peak, as shown in Fig.4.12. This corresponds to the spectrum shown in fig. 4.1(deposited at 200 eV). For D = 0.1μm and the shape factor S = 0.7 and corresponding depolarization factors $L_1 = 0.09216$, $L_2 = L_3 = 0.45166$ and a volume filling fraction of 0.2133, the peak position at 2.24 eV obtained from the simulation again coincides with the experimental absorption peak as shown in Fig.4.13. This corresponds to the spectrum shown in fig. 4.1(deposited at 400 eV). For D = 0.1μm and the shape factor S = 0.5 and corresponding depolarization factors $L_1 = 0.045$, $L_2 = L_3 = 0.4775$ and the volume filling fraction f = 0.0667, the peak position at 1.75 eV predicted by the simulation coincides with the experimentally observed peak as shown in Figure 4.14. This corresponds to the spectrum shown in fig. 4.1(deposited at 600 eV).

It is apparent from the results presented above, that the theoretical simulation predicts the localized plasmon peak position; it's splitting and also the position of the bulk plasmons. However, there is a difference in the width of the peaks. This is probably due to the

assumption of mono sized particles in our theoretical simulation, in contrast to the large size distribution observed in the actual experiments.

A comparison with experimental results, presented above, shows that when the films are discontinuous, the positions of the SPR peak is determined by the shape of the particles rather than their size or spacing. Evidence for this appears in the form of peaks that are split and spectrally separated (figs (4.1) and 4.3)). As the film thickness is increased, the filling factor (referred to as packing density) increases and therefore the SPR peak positions are completely determined by particle sizes rather than their shapes. This is because, at higher thickness and higher packing density, the particles naturally assume spherical shapes. Thus, using the M-G theory the contributions from shape and size of particles can be distinguished. A point to be noted here is that the peak widths predicted by theory and those observed in experiments are different. Theory predicts much sharper peaks since it assumes a medium in which all particles are of the same size. However, real materials always show a distribution of different sizes leading to larger peak widths in the spectrums. It is observed that experimental well agrees with the theoretical calculations.

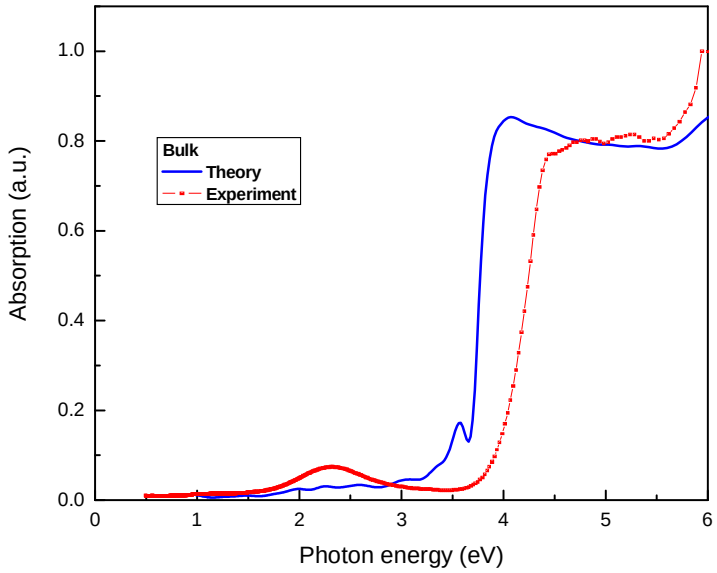

Fig.4.11. Fitting of the simulated absorption spectrum of Ag with the experimentally measured spectrum of bulk silver.

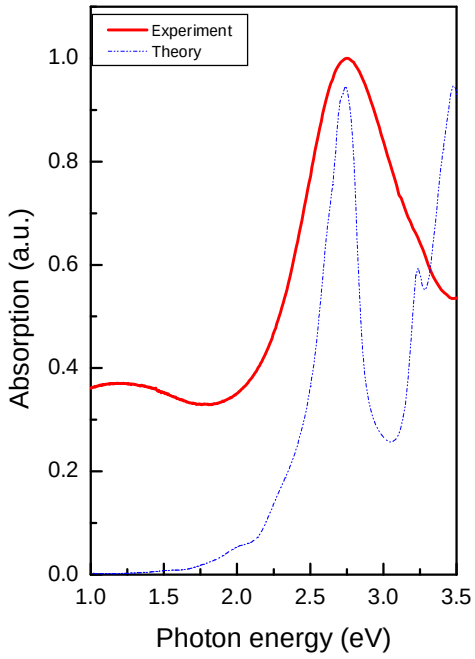

Fig.4.12. Fitting of the simulated absorption spectrum of Ag with the experimentally measured spectrum.

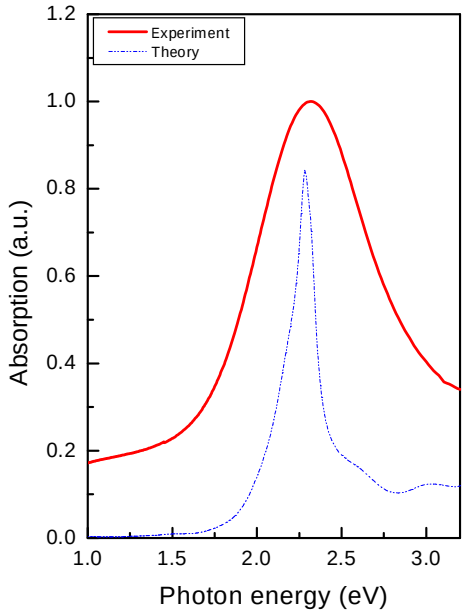

Fig 4.13. Fitting of the simulated absorption spectrum of Ag with the experimentally measured spectrum.

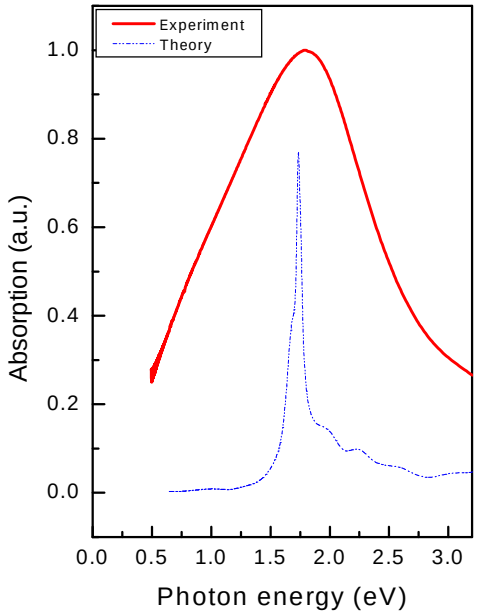

Fig.4.14. Fitting of the simulated absorption spectrum of Ag with the experimentally measured spectrum.

4.6. Summary

In summary, the optical response of single layer Ag and Au thin films have been studied briefly. In the case of Ag and Au thin films, the plasmon resonance peak is found to be red shifting with the increase of the thickness of the films which is due to the increase in ion energy and increase in duration of the deposition time. It is observed that the simulation results agrees well with the experimental results and found that the shape factor has more influence then the volume fractions.

In the case of Ag and Au thin films deposited at fixed energy at different temperature, the surface plasmon resonance peak shifts towards blue with the increase of the temperature and this is due to the decrease in the particle size. For the Au films deposited at 450 eV ion energy for constant temperature 300^{o}C and at varying duration of deposition time, it is observed that the plasmon resonance peak shifts towards red which is due to the increase in the thickness of the films due to the increase in duration of deposition time and as well as increase in the grain size.

References

1. H. G. Craighead, G. A. Niklasson, Appl. Phys. Lett. **44** (1984) 1134.
2. A. C. R. Pipino, G. C. Schatz, R. P. Van Duyne, Phys. Rev. **B53** (1996) 4162.
3. T. W. H. Oates, A. Mucklich, Nanotechnology **16** (2005) 2606.
4. R. Gupta, M. J. Dyer, W. A. Weimer, J. Appl. Phys. **92** (2002) 5264.
5. H. Mertens, J. Verhoeven, A. Polman, F. D. Tichelaar, Appl. Phys. Lett. **85** (2004) 1317.
6. M. Hirai, A. Kumar, J. Appl. Phys. **100** (2006) 014309.
7. C. Sonnichsen, T. Franzl, T. Wilk, G. Von Plessen, J. Feldmann, New J. Phys. **4** (2002) 93.1.
8. C. Noguez, J. Phys. Chem. **C 111** (2007) 3805.
9. K. C. Le, S. J. Lin, C. H. Lin, C. S. Tsai and Y. J. Lu, Surface & Coating Technology, **202** (2008) 5339-5342.
10. M. Gnanavel, D. Bharathi Mohan and C. S. Sunandana, Thin Solid Films, **517** (2008) 1058 – 1062.
11. A. Singh, J. Jayabalan, R. Chari, H. Srivastava and S. M. Oak, J. Phys. D: Appl. Phys. **43** (2010) 335401.
12. R. M. Tilaki, A. Irajizad, S. M. Mahdavi, Appl. Phys. A **84** (2006) 215-219.
13. R. Sreeja, P. M. Aneesh, A. Arvind, R. Reshmi, R. Philip and M. K. Jayaraj, Journal of the Electrochemical Society, **156** (10) (2009) K167 – K172.
14. Y. Takeda, O. A. Plaksin, H. Wang, K. Kono, N. Umeda and N. Kishimoto, Optical Review, **13** No. 4 (2006) 231-234.
15. H. Neff, W. Zong, A. M. N. Lima, M. Borre and G. Holzhuter, Thin solid films, **496** (2006) 688 – 697.
16. J. D. Jackson, “Classical Electrodynamics”, Wiley, New York (1999).
17. F. L. Galeener, Phys. Rev. Lett. **27** (1971) 421; F. L. Galeener, Phys. Rev. **B27** (1971) 1716.
18. R.W. Cohen, G. D. Coutts and B. Abeles, Phys. Rev. **B8** (1973) 3689.
19. H. Fricke, Phys. Rev. **24** (1924) 5775.
20. J. A. Stratton, “Electromagnetic theory”, IEEE Press, New York (2007); L. Nicolais, “Metal Polymer Nano Composites”, John Wiley, New Jersey (2005), Chap.6.

Chapter V: Optical response of metal-metal and metal-dielectric bilayer thin films

Abstract

This chapter presents the morphology and optical response of metal-metal and metal-dielectric bilayer thin films. The systems studied are (1) Ag/Au (Ag as top layer), (2) Au/Ag (Au as top layer), (3) In/Ag (In top layer), (4) Ag/TiO_2 and Ag/ZrO_2 (Ag as top layer) and (5) Au/TiO_2 and Au/ZrO_2 (Au as top layer) bilayer thin films. In the case of Ag/Au and Au/Ag bilayer, the underlayer thickness is constant. Morphology of bilayer is denser than the single layer films and surface plasmon resonance (SPR) shifts towards red and width of the peak increases with the increase of the top layer in both the cases. In the case of Ag/In bilayer, underlayer thickness is varied and top Ag layer thickness is constant. It is observed that SPR peak shifts towards red with splitting in the peak when In layer thickness is increased. The observed behaviour of SPR is discussed by hybridization model. In the case of metal-bilayer films, the bilayer thin films show enhanced light absorption in the ultraviolet region and refractive index controlled optical absorption at near infrared wavelengths. It is observed that the SPR of the metal exhibits a red-shift with increase in refractive index of the dielectric underlayer. The details of this behaviour are discussed here.

Chapter V: Optical response of metal-metal and metal-dielectric bilayer thin films

5. Introduction

Majority of the work on surface plasmons is either on elemental films of Ag or Au or these elements embedded in a dielectric matrix. Experimental studies as well as theory of the effect of shape and size of metal nanoparticles on the optical absorption and therefore plasmon resonances in such systems have been reported [1-15]. Bimetallic and other complex metallic nanostructures have also evinced considerable interest in the context of their optical response [16-20]. Tuning of the SPR is usually achieved by controlling the size, shape and spatial arrangement of nanoparticles. Further tuning of the SPR over a wide energy range can be obtained using Ag-Au bimetallic nanoparticles, either as core-shell or as alloyed structure [21]. A simple way to obtain Ag-Au nanoparticle systems is deposition of metal island films as they can be obtained during the initial stage of the deposition. Recently metal island films have been used as building blocks for photonic and plasmonic structures [22]. Typical growth of metal island films results in wide distribution of size and shape of particles, which can be controlled by the deposition conditions and post-deposition treatments. However, as in the case of the elemental thin films much of this work is focused on the Au-Ag bimetallic system with Ag-Cu being another system that has been studied. It has been shown that bimetallic nanosystems can be used for tuning surface plasmon resonances that may be useful for SPR applications. Although metal multilayers with a dielectric sandwiched between the metallic layers have been studied [23-27], the case of metallic bilayers has not been considered frequently. Analogous to bimetallic nanostructures, which are essentially core-shell type of structures, it is expected that the contrast in dielectric functions of two dissimilar metals should lead to a wide range of plasmon resonances.

In other systems of metal nanoparticles, nanostructured metal/dielectric bilayers films exhibit a diverse range of optical properties with great potential for application. Bilayers of Ag and Au with TiO_2 are extremely useful for photocatalytic applications. It has been demonstrated that TiO_2 and Ag/TiO_2 has an intense absorption of light below 385 nm due

to the transitions near the band gap which can be exploited for photocatalytic degradation of environmental pollutants [28-32]. Photochromism and enhanced two photon luminescence has also been reported in Ag/TiO_2 [33]. ZrO_2/Au nanocomposite thin films have potential for applications in sensors [34] and catalysis [35]. An important application of metal-dielectric nanocomposites is in surface plasmon resonance based devices where tunability of plasmon resonance is the central issue. In noble metal thin films tunability is generally achieved by controlling shape and size of nanoparticles. Effective medium theories show that tunability can also be achieved by controlling the dielectric function of the medium surrounding the metal [2, 36, 37]. This is easily realized by fabricating metal-dielectric core-shell structures and bimetallic particles to control the position of plasmon resonance [17, 38, 39]. The aspect of plasmon resonances in metallic and metal-dielectric bilayers and multilayers is, however, not as well studied as metal-dielectric core shell structures [40-42]. It has recently been shown that surface plasmon resonances in noble metal particles can also be effectively exploited to increase efficiency of solar cells by improving light trapping in regions of the electromagnetic spectrum where the cells have negligible absorption [43-45]. Therefore, study on optical properties of metal/dielectric bilayer thin films in the UV-Vis-NIR region is also important since it provides important insight in to the electronic and band structure of the metal and the dielectric layers. In addition, it is possible to obtain information on the microstructural origins of the optical response.

In the present work, two types of bilayer systems were investigated. One is to investigate the effect of metal-metal interface on SPR behaviour and the second is to study the effect of dielectrics environment on the optical response on metal-dielectric bilayers. In the case of metal-metal bilayer thin films the systems studied are (1) In/Ag (Ag as top layer) (2) Ag/Au (Ag as top layer), (3) Au/Ag (Au as top layer), The metal-dielectric systems studied are (1) Ag/TiO_2 and Ag/ZrO_2 (Ag as top layer) and (2) Au/TiO_2 and Au/ZrO_2 (Au as top layer) bilayer thin films.

5.1. Optical response of Ag/In bilayer thin films deposited by thermal evaporation technique.

Silver-indium bilayer films were prepared by thermal evaporation, maintaining a pressure of 3.5×10^{-6} Torr during the deposition process on to fused silica substrates at ambient

temperature. First, pure indium (purity 99.99%) films were prepared. For these single In layers, the characterization for optical properties, morphology, thickness and structure analysis was done before the deposition of Ag layer on top. The In layer thickness was varied between 3 and 30 nm. After characterizing the In layers, silver (purity 99.99%) films of a constant thickness of 5 nm were coated on the top of all indium films. In both cases, detailed optimization and calibration of thickness vs time of deposition was carried out. The error in thickness estimate is of the order of ±1 nm based on statistics of several experiments. The bilayers and individual Ag layers were also characterized for all the properties mentioned above.

They x-ray diffraction pattern for single layer of both the metal films and bilayer films are shown in fig.5.1. X-ray diffraction pattern of a single layer In film of thickness 30nm is shown in fig.5.1.(a). It is observed that the film has crystallized in to the body centred tetragonal (BCT) structure showing the (101) and (202) reflections. It was observed that the onset of crystallization occurred at a thickness of ~10 nm. The Ag layers did not show any evidence for the presence of long-range order as observed in (fig.5.1(b)). The x-ray diffraction patterns of the bilayers are shown in fig.5.1. (c) to (f). It is evident that the nature of crystallinity of the Indium layers is not affected by the presence of the Ag layers. Both the observed peaks can be attributed to Indium and there is no evidence for crystalline indium oxide formation. The crystallite size measured from the x-ray diffraction patterns was 40 - 45 nm.

The morphology of pure indium and silver films deposited on fused silica substrates and silver overlayers on these indium films were studied by atomic force microscopy (AFM). The morphology of pure Ag and In film is shown in fig.5.2(a) and 5.2(b) respectively. Thin film deposition at ambient temperature by thermal evaporation leads to large agglomerates due to low surface mobility of the adatoms. This is evident in the morphology of the 3 nm thick In film shown in fig.5.2.

Both these images show similar semi continuous nature with grains of mean size 60 and 80 nm. The large grain sizes are a result of the aggregation process that is typical of thermally evaporated thin films. At 3 nm the grain size is 60 nm, which increases to 210 nm at 20 nm and 290 nm at 26 nm shown in fig.5.3 (a) and (b). It is probably due to aggregation of a number of smaller sized grains as stated earlier. From table 5.1 it is

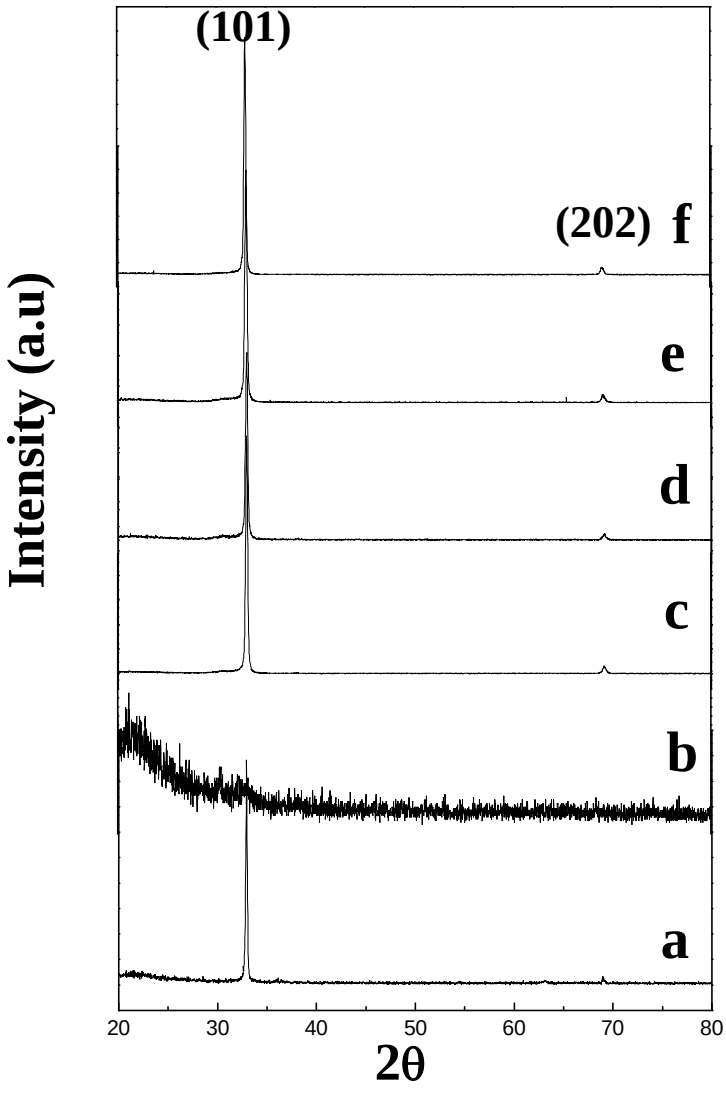

Fig.5.1. XRD patterns of (a) 30 nm thick pure In film, (b) 5 nm thick pure Ag film and In /Ag bilayer films with In thickness of (c) 3, (d) 10, (e) 20 and (f) 25 nm.

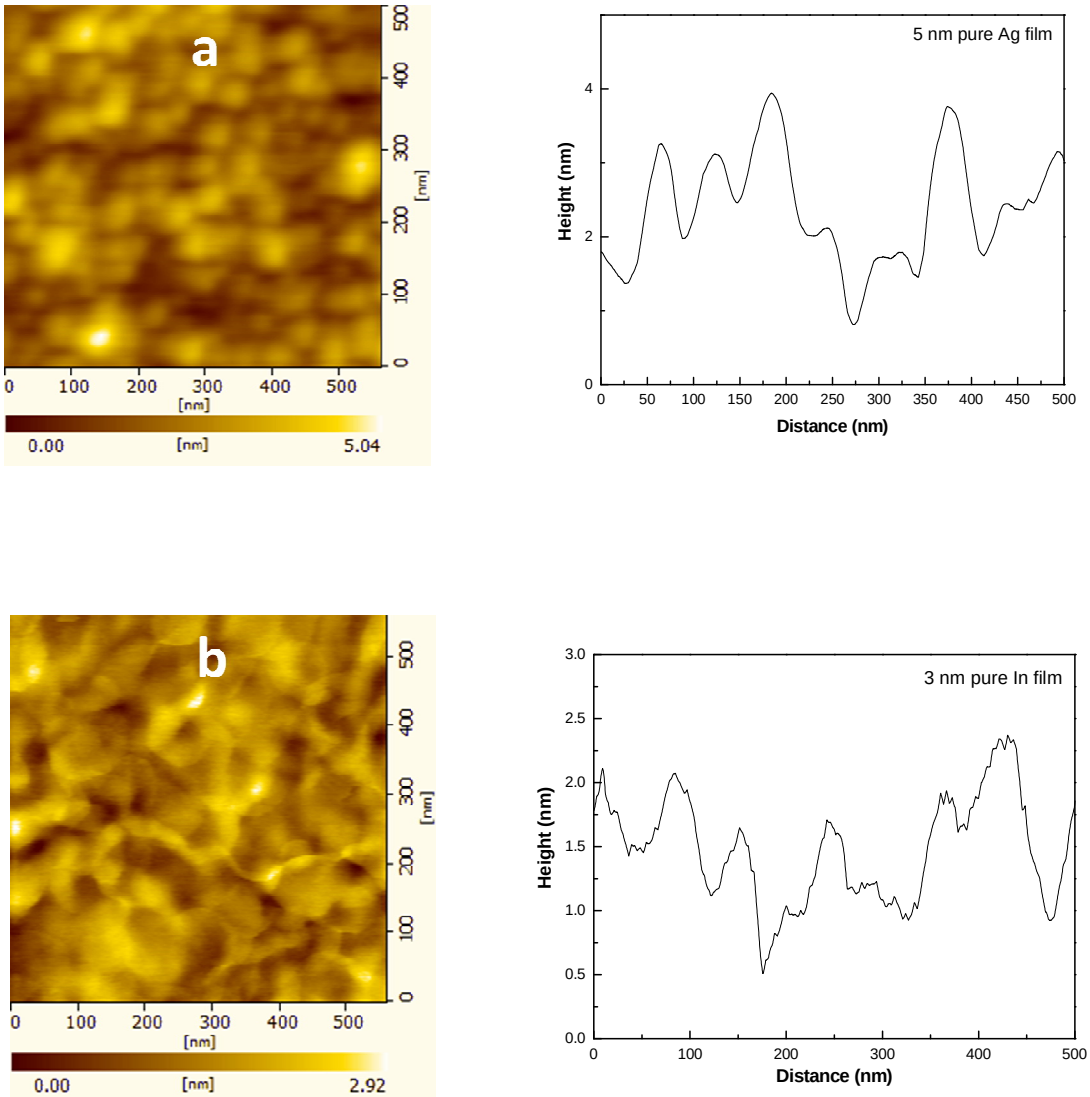

Fig. 5.2. AFM images of Pure (a) 5 nm Ag thin film and (b) 3 nm In thin film and its corresponding height profile.

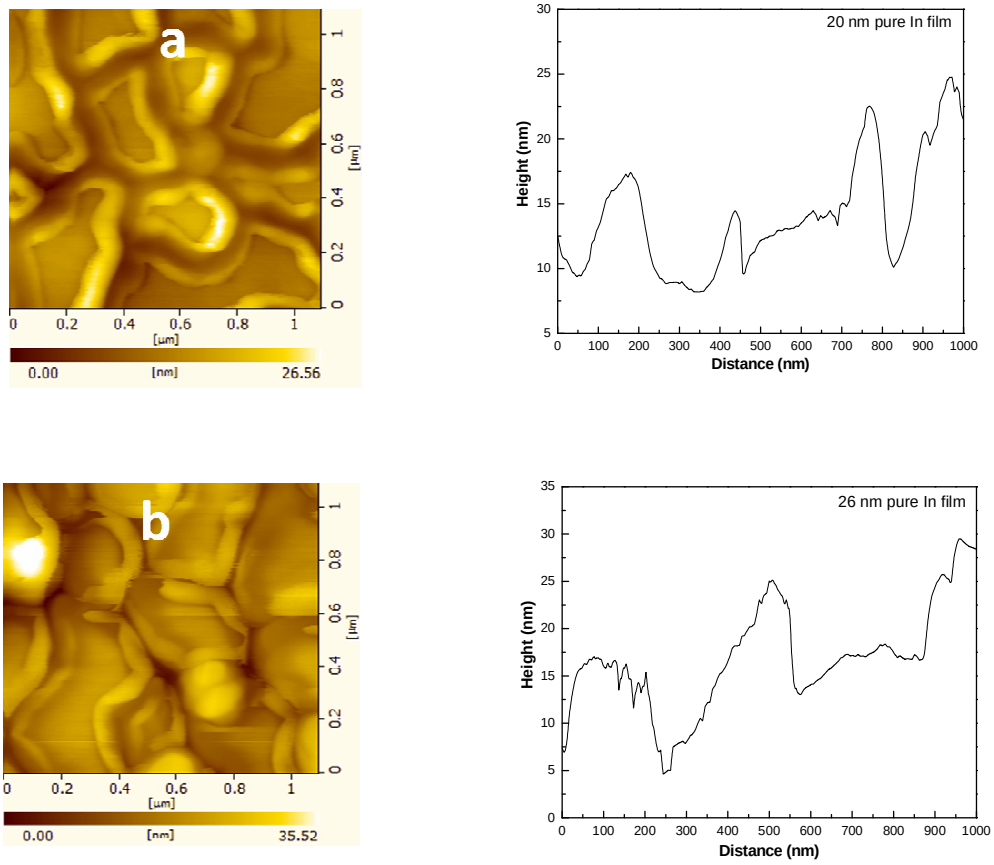

Fig.5.3. AFM images of pure In films of thickness (a) 20 and (b) 26 nm and its corresponding height profile.

Table 5.1. Thickness, surface roughness and grain size of pure In and Ag films.

Thickness of film (nm)	**RMS surface roughness (nm)**	**Grain size (nm)**
In – 3 nm	1 nm	60 nm
In – 15 nm	6 nm	168 nm
In – 20 nm	4 nm	210 nm
In – 26 nm	13	290 nm
In – 30 nm	9 nm	350 nm
Ag – 5 nm	1 nm	80 nm

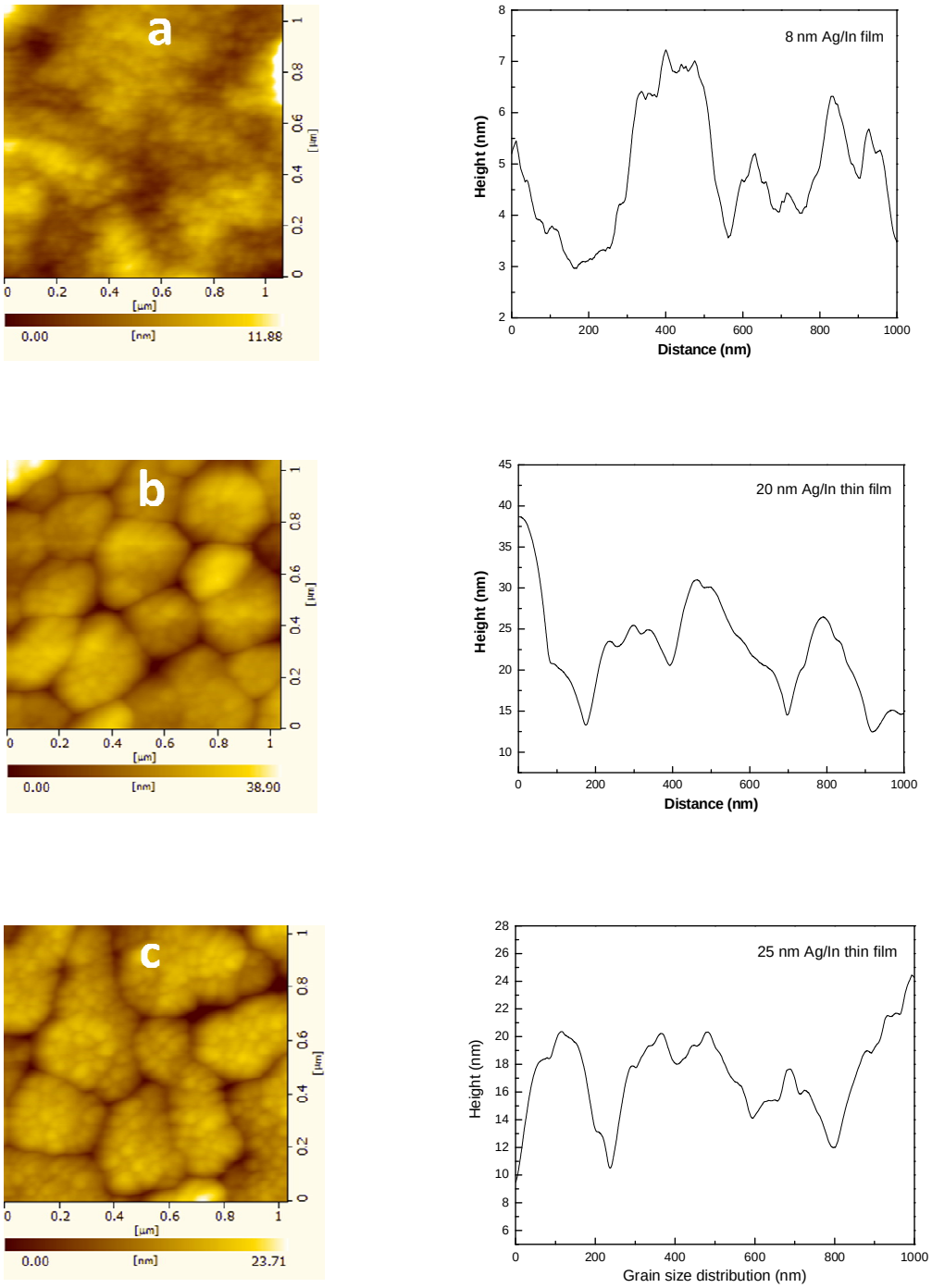

Fig.5.4. AFM images of Ag/In bilayer thin films with In thickness of (a) 3, (b) 15 and (c) 20 nm and its corresponding height profile.

Table 5.2. Thickness, surface roughness and grain size of Ag/In bilayer films.

Thickness of Ag/In film (nm)	RMS surface roughness (nm)	Grain size (nm)
8 nm	2 nm	80 nm
20 nm	7 nm	100 nm
25 nm	5 nm	120 nm
31 nm	15 nm	300 nm
35 nm	5 nm	280 nm

observed that the surface roughness of the In films increases from 1 nm at 3 nm to 13 nm at 26 nm and decreasing thereafter at 30 nm. The morphology of the bilayers is much more uniform as seen in fig.5.4.(a) and (b) for two different thicknesses of In and presented in table 5.2 for all the films.

The roughness of the films increased from 2.14 nm at 8 nm to 7.26 nm at 20 nm and 5.78 nm at 35 nm. These values clearly indicate the granularity of the surfaces under consideration.

The growth of the films follows the structure zone models that have been used to describe the evolution of thin film microstructure as a function of surface adatom mobility which is described in the chapter III [46-50]. At substrate temperatures (T_s) much lower than the melting point (T_m) of the elements the adatom mobility is insufficient for impacting vapour atoms to move on the substrates. The adatoms freeze instantly on impact on the substrate and subsequent atoms deposit on these initial layers leading to a columnar microstructure as observed in the AFM images shown in fig5.2(a). The melting point of In is 156.61^{o}C and therefore deposition at ambient temperature gives a value of 0.2 for the ratio of T_s/T_m For silver with a melting point of 962^{o}C, this value is even lower. Thus, the films exhibit the Zone I type of microstructure expected from the structure zone models. Furthermore in the initial stages there is agglomeration of the condensing atoms giving rise to a “cauliflower” type of growth on the top surface and therefore a roughness which is comparable to the thickness or in some cases greater than that. This is again evident in the morphology shown in fig.5.2(b) where both roughness and height of the agglomerated objects is comparable to the thickness of the films.

The absorption spectra of pure indium films deposited on fused silica substrate are shown in Fig.5.5 (a) to (e) for different thicknesses. From the spectra, it is observed that the absorption peak for the single layer films is red shifted with increase in thickness. For the 3 nm In film there is a peak centered at 372 nm with a width of 180 nm. On further increase in thickness to 10 nm, there is appearance of a "shoulder" at the shorter wavelength side while the main absorption peak shifts to a wavelength of 420 nm and the width increases to approximately 225 nm. Further increase in the thickness results in sharpening of the low wavelength peak at 320 nm with the "shoulder" appearing on the longer wavelength side. In both cases, the peak is centered around 390 nm with a width of approximately 200 nm. The 30 nm thick film showed a very broad peak in absorption at 685 nm with a very high long wavelength tail. The single layer Ag film (fig. 5.5(f)) showed a peak at 590 nm.

The features in the optical absorption of a metal thin films normally arise from either scattering, interband transitions or the presence of plasmons. Each of these features are evident in different regions of the spectrum and can be detected depending on the crystallographic texture or microstructural evolution of the films. Surface plasmons are an entirely size dependent effect observed only in nanostructured metal thin films. There are very limited reports on studies of plasmon resonances in In films [51-54]. In a significant study, Anno and Tanimoto [51] have investigated the size dependence of interband transitions and optical plasmon resonances of In nanoparticles in In thin films. They varied the particle size over the range of 22 to 52 nm with increase in thickness from 4.4 to 11.6 nm and observed two features in the optical absorption spectra one of which was centred around 234 nm and the other at 335 nm. The latter feature showed a size dependent shift. While the feature at 234 nm has been attributed to interband transition, the feature at the longer wavelength is attributed to optical plasmon resonance. Rama and Pino [52] have studied plasmon resonances of In nanoparticles synthesized by preparing a hybrid of In and toluene and In and paraffin oil mixtures. In this study by varying the particle sizes from 1.3 to 12 to 107 nm they found plasmon resonances at 281, 291, 319, 340 and 350 nm.

On coupling the In and Ag layers, very interesting behavior in optical absorption is observed as shown in fig.5.6 (a) to (e).

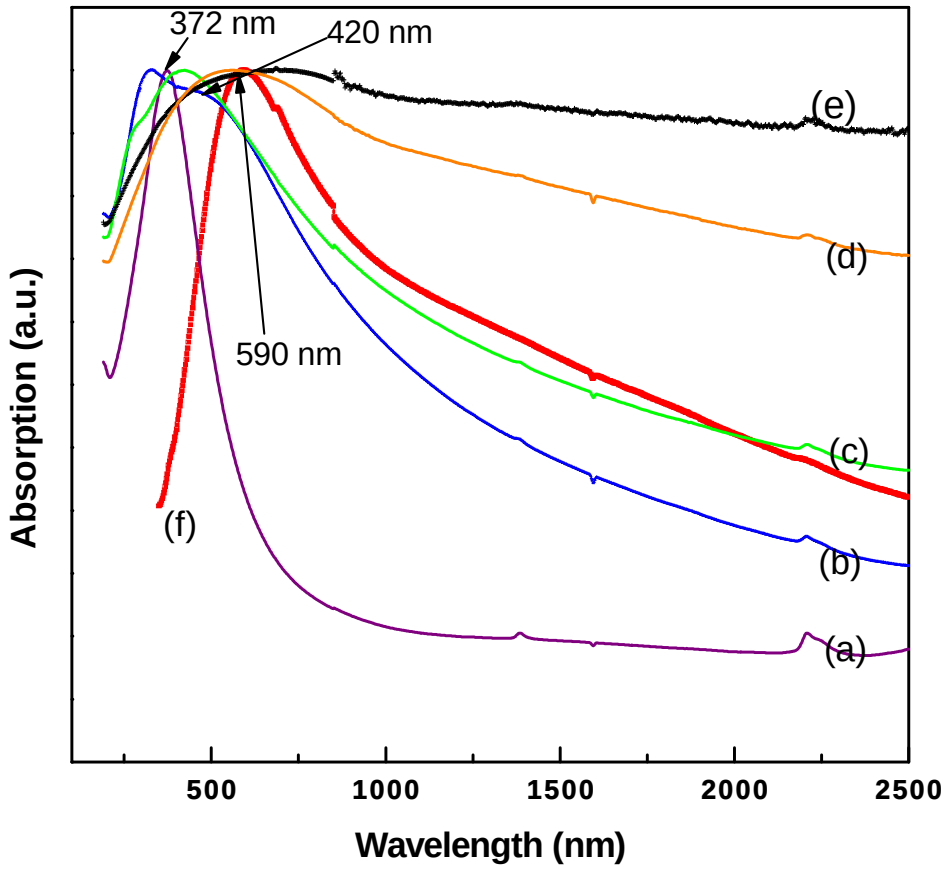

Fig.5.5. Absorption spectrum of pure In films with increasing thickness (a) 3, (b) 10, (c) 20, (d) 25 and (e) 30 nm and (f) absorbance spectrum of the 5 nm thick pure Ag film.

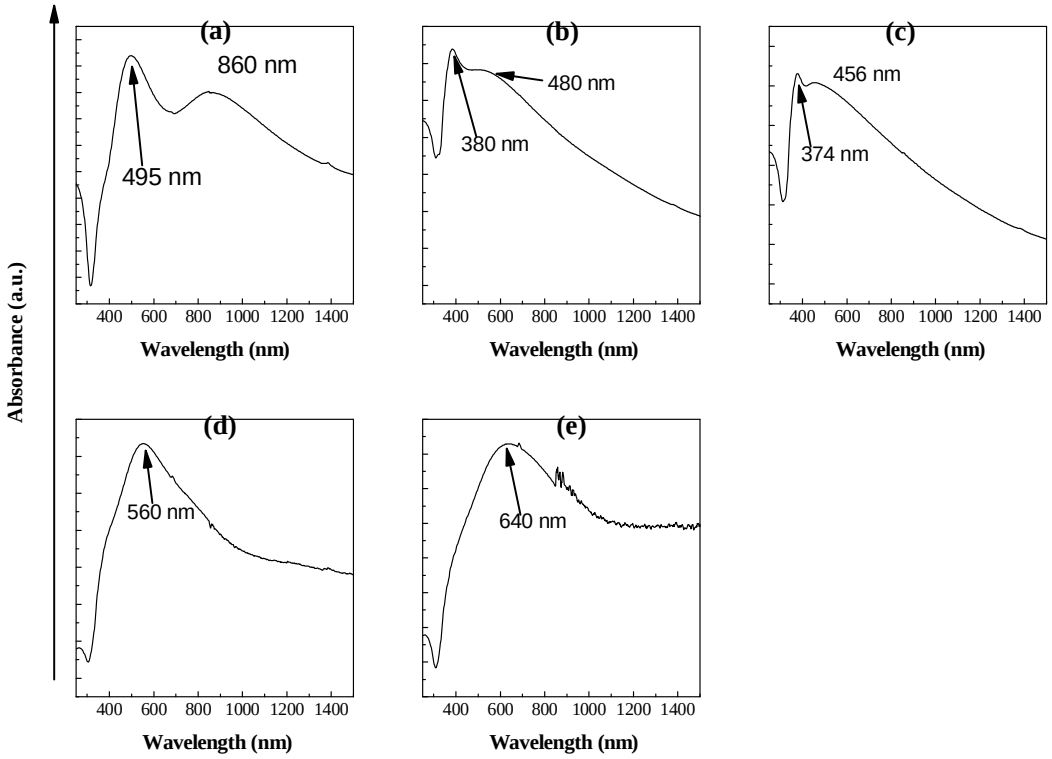

Fig.5.6. Absorption spectrum of Ag/In bilayer films with In thickness of (a) 8, (b) 10, (c) 20 (d) 25 and (e) 30 nm.

It should be noted that the thickness of the Ag layer is maintained constant at 5nm in the following discussion. Only the thickness of the In layer in the Ag/In bilayer is varied and hence only that thickness is mentioned. For the 3nm thick In film in the Ag/In bilayer two resonances appear. The first peak is at a wavelength of 495 nm while the second peak is at a wavelength of 860 nm. For the 10 nm thick In film in the Ag/In bilayer, the splitting in the resonances is decreased with a peak at 380 nm and a broad shoulder centered around 480 nm and for 20 nm Ag/In films, the splitting in the resonance further decreased with a peak at 374 nm and a broad shoulder around 456 nm. Further increase in the thickness of the In layer causes the merger of these two peaks and the appearance of a single resonance (fig 5.6(c)) at 560 nm (for the 20 nm In layer) and finally a red shift to 640 nm for the 30 nm thick In layer (fig. 5.6.(e)).

5.2. Optical response of Ag/Au (Ag as top layer) and Au/Ag (Au as top layer) bilayer thin films

Ag/Au (Ag on top layer) and Au/Ag (Au on top layer) bilayer thin films were deposited by ion beam sputtering technique on borosilicate glass substrate from Ag (99.99%) and Au (99.99%) target material at ambient temperature. In both the bilayer case, the thickness of bottom layer was kept constant whereas top layers thickness was varied by depositing for different time. The Ag films were deposited at 150 eV of ion energy and Au films were deposited at 250 eV of ion energy. The chamber was evacuated to 2×10^{-6} Torr before introducing Ar gas and deposition was carried out at 4×10^{-4} Torr throughout the experiment. Optical absorption spectrum was measured from 190 nm to 2500 nm wavelength using a UV-Vis-NIR spectrophotometer and the microstructure and morphology analysis were carried out in an atomic force microscope.

The morphology of the single layer Ag and Au is shown in fig.5.7 (a) and (b) respectively. Morphology of bilayer Ag/Au and Au/Ag film is shown in fig.5.8 and fig.5.9. It is observed that the morphology of single layer of Ag and Au thin films are semi continuous with an average grain size of 40 – 60 nm in both the cases. The Ag film has more spherical in shape and the grains in Au film are island kind connected to each other. The film becomes denser and continuous in the case of bilayer films in both the cases and grain size remains same. The continuous nature of the film is due to the contributions from both the layers.

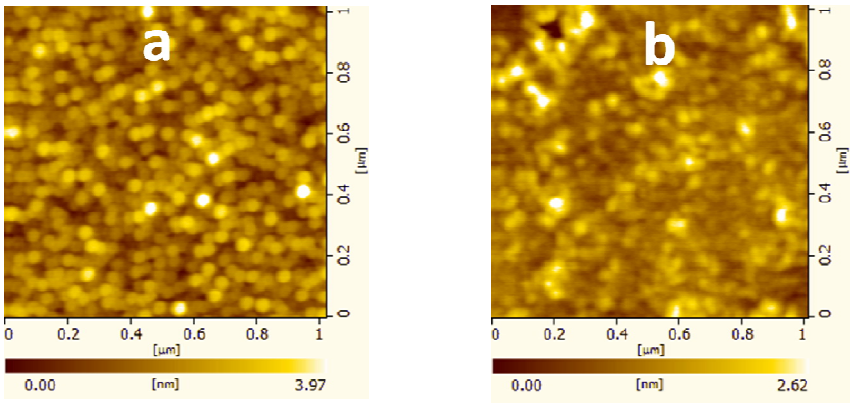

Fig.5.7. AFM images of single layer (a) Ag and (b) Au thin film.

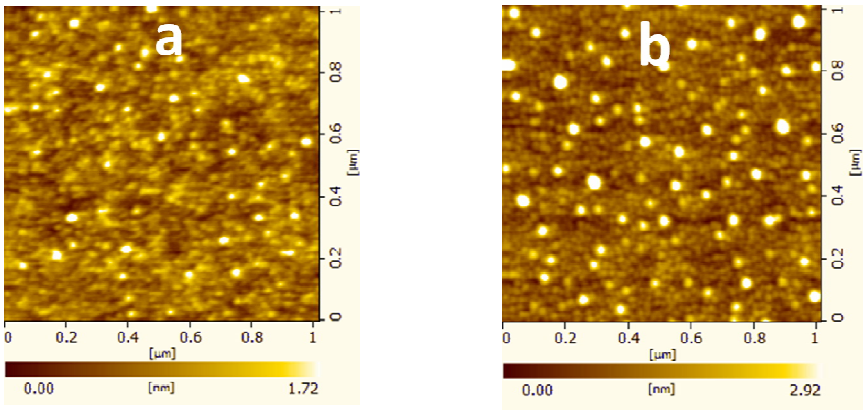

Fig.5.8. AFM images of bilayer Ag/Au films with Ag deposition of (a) 20 and (b) 30 min.

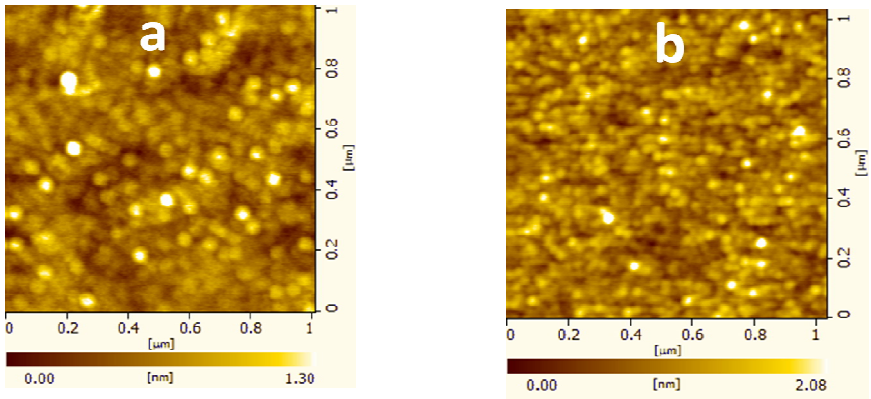

Fig.5.9. AFM images of bilayer Au/Ag films with Au deposition of (a) 15 and (b) 25 min.

Fig.5.10. shows the absorption spectrum of single layer Ag and Au thin films. The surface plasomon resonance (SPR) peak for single layer Ag is at 444 nm and Au is at 586 nm. When Au is coated on Ag layer, the SPR peak is found to be shifted and the same case is observed when Ag is deposited Au single layer. Fig.5.11. shows the absorption spectrum of Ag/Au bilayer thin films in which case the thickness of Au layer is constant and Ag layer is varied. Here, it is observed that the SPR peak shifts towards red with the increase of the thickness of the Ag layer which is very true for the single layer Ag thin films [55]. Fig.5.12. shows the absorption spectrum of Au/Ag bilayer thin films.

Here, Au is top layer with different thickness and Ag is bottom layer with constant thickness. In the case of Au/Ag too, the SPR peak shifts towards red with the increase of thickness. It is clearly observed from the SPR peak that the width is increasing with the increase of the thickness of the film in which case, it could be said that the affect on SPR is due to the hybridization of the metal layer.

5.3. Origin of splitting and broadening of plasmon resonance peaks in metal-metal bilayers

The nature of plasmon resonances in a single layer of metal embedded in a dielectric matrix have been studied theoretically, as stated in chapter IV, within the framework of Mie and Maxwell-Garnett theories and the Effective medium approximation [56-58]. These theories describe the modification of the applied electric field by the dipole fields of individual polarizable spherical metallic particles embedded in a dielectric medium. These models are valid in the size regime where the macroscopic Maxwell's equation can be applied, which is true so long as their dimensions are less than the wavelength of light in the medium. Starting from Clausius-Mosotti equation it can be shown that if x is the volume fraction of the insulator then the dielectric function of the metal ε_m and ε_i is that of the insulators can be expressed in the form

$$\frac{\varepsilon(\omega)-\varepsilon_i(\omega)}{\varepsilon(\omega)+2\varepsilon_i(\omega)} = (1-x)\frac{\varepsilon_m(\omega)-\varepsilon_i(\omega)}{\varepsilon_m(\omega)+2\varepsilon_i(\omega)} \qquad (5.1)$$

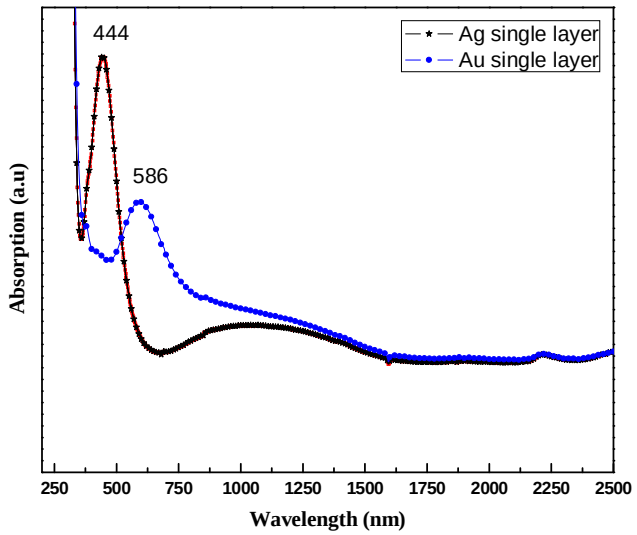

Fig.5.10. Absorption spectrum of single layer Ag and Au thin films.

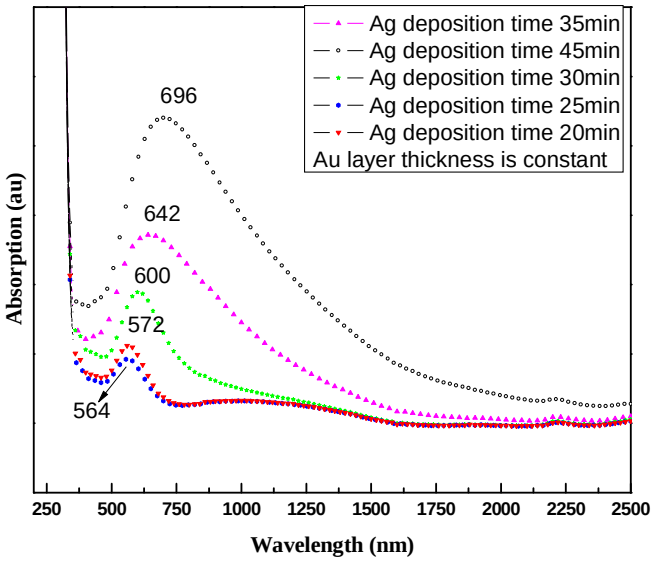

Fig.5.11. Absorption spectrum of Ag/Au bilayer thin films with Ag layer deposited for different time.

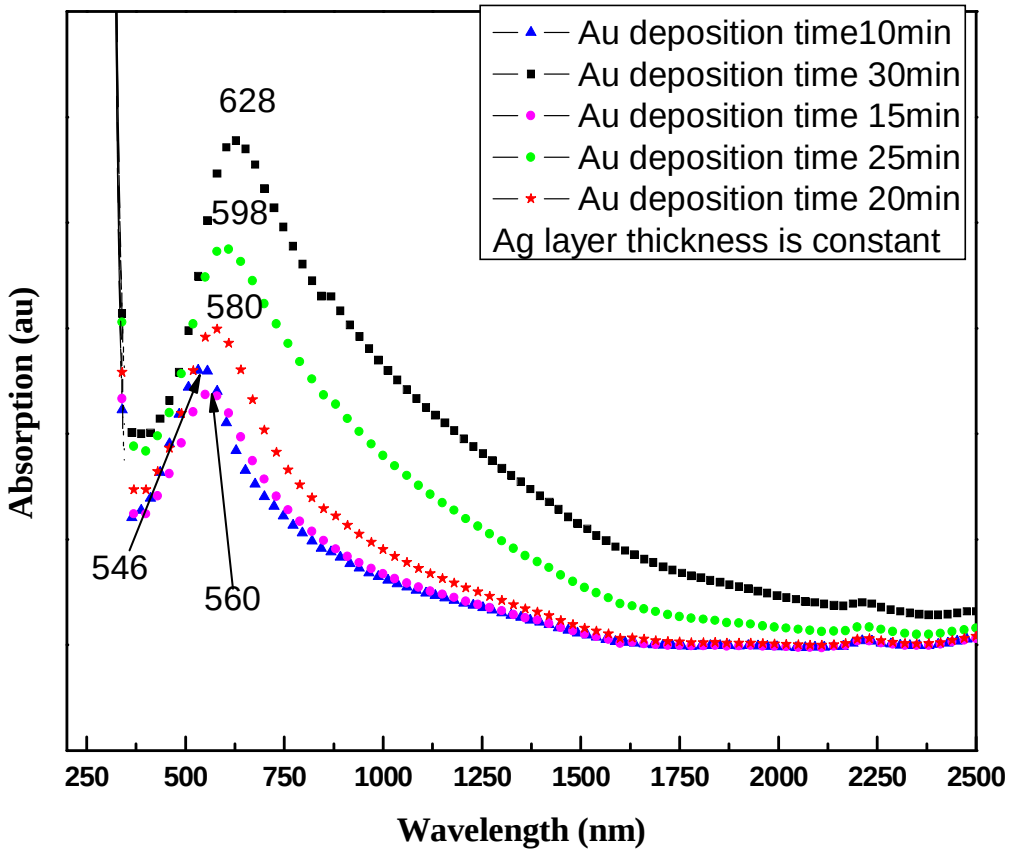

.

Fig.5.12. Absorption spectrum of Au/Ag bilayer thin films with Au layer deposited for different time.

Equation (5.1) assumes that the particles are spherical in shape. The non-spherical shape of the particles is taken in to account by introducing the depolarization factors L_m, so that the equation becomes

$$\frac{\varepsilon(\omega)-\varepsilon_i(\omega)}{\varepsilon(\omega)+2\varepsilon_i(\omega)} = (1-x)\frac{\varepsilon_m(\omega)-\varepsilon_i(\omega)}{L_m\varepsilon_m(\omega)+(1-L_m)\varepsilon_i(\omega)} \qquad (5.2)$$

For spheres $L_m = 1/3$ and in general $0 \leq L_m \leq 1$.

These equations have been used to theoretically predict the position of surface plasmon resonance peaks and that a combination of volume fraction less than 1 and non-spherical shapes can lead to splitting of the plasmon resonance peaks. The magnitude of splitting is dependent on the strength of dipole interactions due to a combination of the volume fraction and anisotropy in shape (also called the "shape factor"). This model has been used very successfully to describe various features observed in the absorption spectrum for single layer metal films. Typically effects due to scattering are observed in the infrared while the contributions due to interband transitions occur at frequencies well separated from the plasmon resonance. The interband transition for In, Ag and Au occur at occurs at wavelengths around 950, 310 and 250 nm respectively [59, 60]. It is thus evident that the features in the absorption spectra of individual metal layers contain contributions from plasmon resonances with splitting due to shape and volume fractions, and scattering. In the case of thicker films the scattering effects dominate over the plasmon resonances leading to complete suppression of the plasmon resonance which is manifested as a broad peak for the 30 nm film. The red shift with thickness of the films is due to a combination of the change in shape of particles and the porosity of the films (*i.e.* volume fraction).

The observed plasmon resonance behavior in the metal bilayers can be explained based on the plasmon hybridization model, proposed by Prodan *et al.* and refined by other workers [61-63]. According to this model, the metal nanoshell can be considered as a two-interface system that supports two distinct plasmon modes, one due to the outer shell-surface of the sphere mode (top layer in the current case) and the other is the inner shell-surface cavity mode. These modes couple or hybridize with each other, leading to a splitting into two new modes. They further show that the antisymmetric combination of these modes results in a blue-shifted plasmon mode, while the symmetric combination results in a lower red-shifted plasmon mode. The symmetric combination of these modes leads to a plasmon resonance that lies in the visible or near-infrared region. The strength of this plaasmon interaction thus determines both the position of the resonance and the extent of the splitting. Thus, the absorption spectrum will exhibit features of both metals, depending on relative concentrations and also a band due to the coupling of the aggregated particles. This is evidently the case in the metal bilayers, in the current study, leading to plasmon resonances over a large range of the spectrum from approximately 370 to 686 nm in both the bilayer cases.

5.4. Optical response of metal/dielectric bilayer thin films

In this work, Ag and Au films were deposited on to the TiO_2 and ZrO_2 thin films. Initially, The TiO_2 and ZrO_2 films were deposited by the sol-gel approach on to Borosilicate glass (BSG) and fused silica substrates, respectively, [64] with thicknesses in the range of 200 to 300 nm. The reason for depositing the ZrO_2 films on the fused silica substrates is that their band gap is larger than that for BSG. Hence, to estimate the band gap it was necessary to deposit on a substrate that had a larger band gap than ZrO_2. The band gap of SiO_2 is 8.9 eV while that of ZrO_2 is ~5eV. On the other hand, the band gap of the BSG substrate is 4.2 eV. The refractive index in the dispersion free region of the spectrum is 1.9 and 2.2 for the ZrO_2 and TiO_2 films, respectively. The prepared films were characterized for structural, microstructural and optical properties and then the Ag and Au films were ion beam sputter deposited onto the dielectric layers with Argon ions of energy in the range of 150 to 450 eV and beam currents of 4-6 mA. The target substrate distance was about 14 cm. The combination of low energy, low flux and large substrate distances resulted in extremely good control over the microstructural evolution of the Ag and Au films.

The following stacks were studied in the present investigation: Ag(or Au)/TiO_2/SiO_2 and Ag(or Au)/ZrO_2/SiO_2 and studied for structural, mictrostructural and optical properties for all the films.

The first objective was to prepare TiO_2 and ZrO_2 films with a dense microstructure suitable for the deposition of Ag and Au films on top of these layers. This was achieved after a detailed optimization of the sol-gel coating process. Typical morphology of the optimized TiO_2 and ZrO_2 films, obtained from atomic force microscopy, is shown in fig.5.13 (a) and (b). It is evident that films are smooth and very densely packed with particle sizes of the order of 30 to 50 nm in both the cases.

The morphology of the 18nm thick Ag films deposited on top of the different dielectric layers at 150 eV Ar ion energy, obtained from atomic force microscopy, is shown in fig.5.14 (a) and (b). A typical high resolution TEM image of the Ag film deposited on the Cu grid is shown in fig. 5.14(c) and the corresponding electron diffraction pattern is shown in fig.5.14(d). Analysis of the electron diffraction pattern shows that it corresponds to a polycrystalline Ag film. It is observed that the surface morphologies of Ag films on TiO_2 and ZrO_2 are very distinct. The Ag surface consists of discontinuous particles of size 60-80nm on TiO_2. The film deposited on ZrO_2, on the other hand, is very dense with particle sizes of the order of 20-50 nm. In contrast, Au films deposited on TiO_2 are continuous whereas the discontinuous nature is observed for films deposited on ZrO_2. This is evident from the AFM images of 30 nm thick Au films, shown in figs. 5.15 (a) and (b). The TEM image of the Au film deposited on the Cu grid (fig.5.15(c)) shows the discontinuous nature of the film. The corresponding electron diffraction pattern, shown in fig. 5.15(d), reveals that the film is polycrystalline in nature. The crystal structure behavior is similar to that exhibited by Ag films deposited on the Cu grid (fig.5.14(c)). The differences in microstructure can be attributed to the fact that the wettability of Ag (Au) on TiO_2 and ZrO_2 is not the same. In general, it was observed that the packing density of the metal films increased with increase in duration of deposition at a fixed energy as observed from the AFM images.

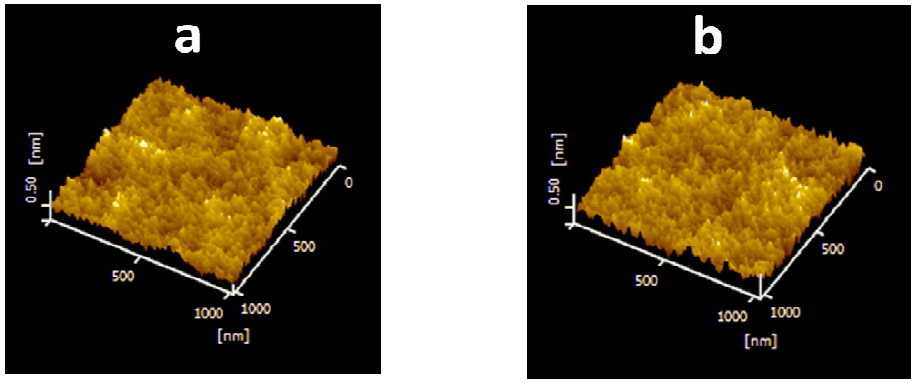

Fig.5.13. AFM images showing the dense surface morphology of the sol-gel prepared (a) TiO_2 and (b) ZrO_2 films.

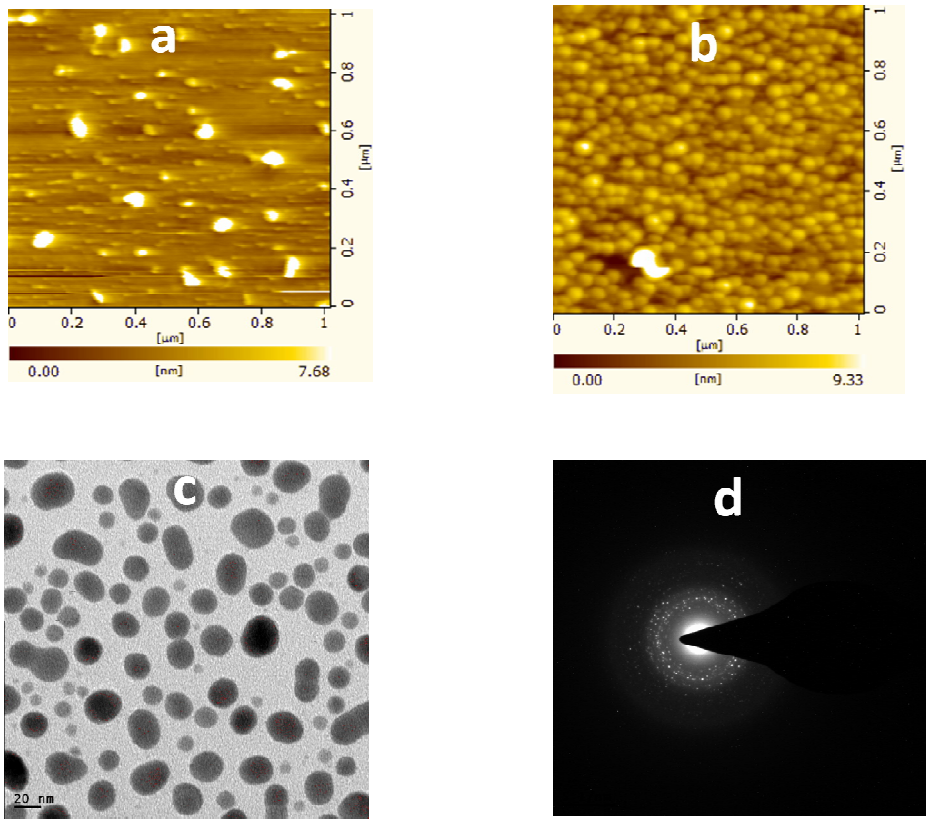

Fig.5.14. AFM images of Ag, ion beam sputter deposited at 150 eV on (a) TiO_2 and (b) ZrO_2 films (c) High resolution TEM image of Ag film on Cu grid and (d) is the corresponding electron diffraction pattern, showing the polycrystalline nature of the film.

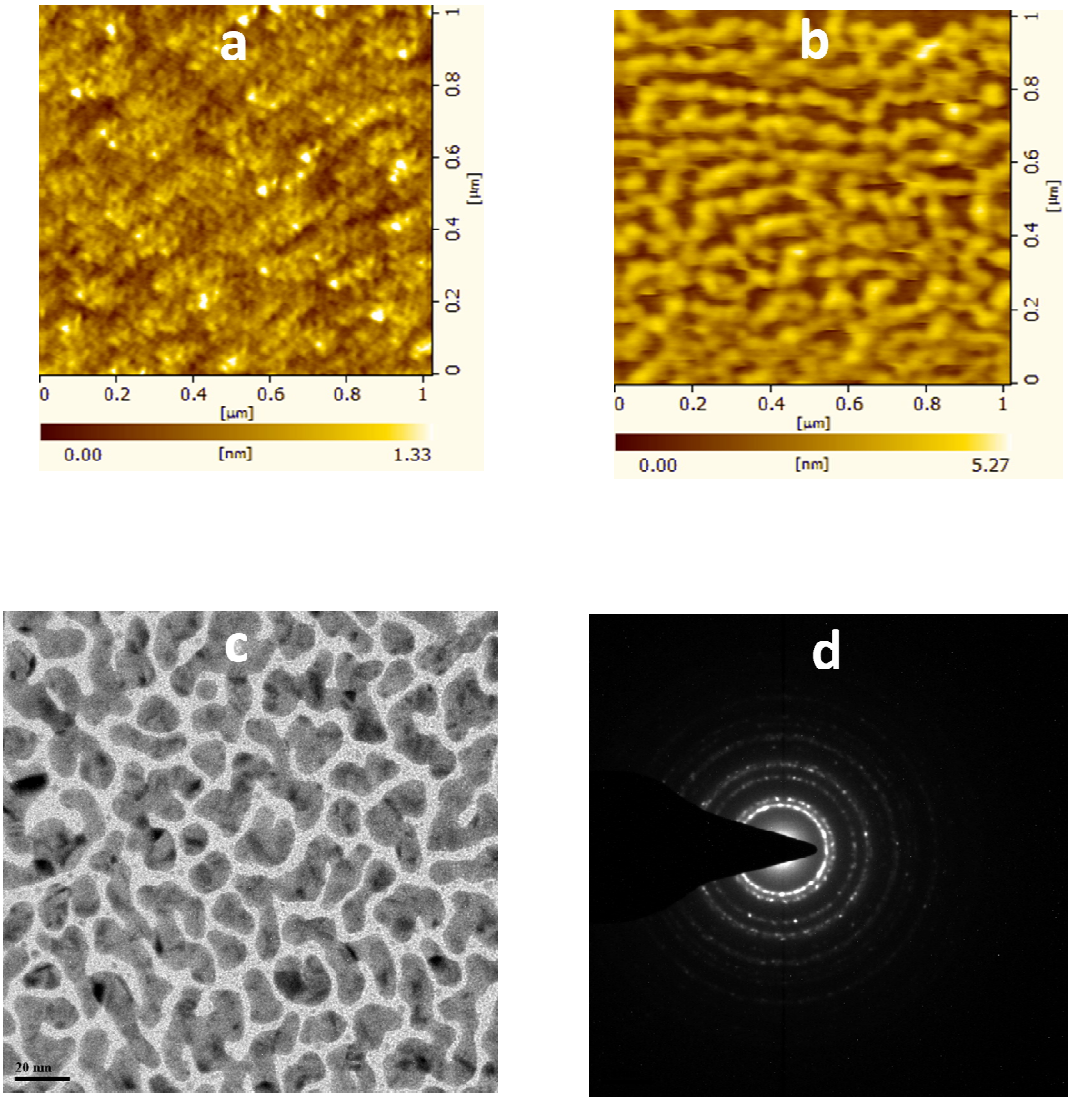

Fig.5.15. AFM images of Au, ion beam sputter deposited at 250 eV on (a) TiO_2 and (b) ZrO_2 films, (c) High resolution TEM image of Au film on Cu grid and (d) is the corresponding electron diffraction pattern, showing the polycrystalline nature of the film.

The microstructural evolution of thin films at low rates of deposition has been the subject of many simulations [65-68]. It has been shown that the condensation process at low rates of deposition and ambient substrate temperature is characterized by the formation of microvoids. The packing density shows a very sharp transition as the substrate temperature increases for low rates of deposition, of the order of 0.1 nm/s, which is similar to the current case.

At this rate of deposition, the energy on impact is not sufficiently large to overcome the activation energy barrier, Q, for surface diffusion. Activation energy, Q, is given as:

$$Q = (5 + \frac{20}{3}\frac{T}{T_m})kT_m \qquad (5.3)$$

where T is the actual temperature and T_m is the melting point of the material. From this equation it can be calculated that at ambient temperature, for silver, Q is of the order of 1 eV. Hence, the incident energy of particles sputtered from the metal target, at low incident ion energies, is < 1eV on impacting the substrate surface. Therefore, these particles freeze on impact without diffusing on the substrate surface. At higher rates of deposition the impacting particles have sufficiently large energy to overcome the diffusion barrier of 1 eV and agglomerate forming dense microstructures.

The effect of thickness of the metal thin films on the optical response of the bilayers was first examined and is shown in figs. 5.16(a) and (b). In this case, Ag of 9 nm thick and Au of 15 nm thick films were deposited on the dielectric layer of TiO_2 and ZrO_2 films. The optical response of Ag (9nm thickness) and Au (15nm thickness) on TiO_2 is shown in fig.5.16(a) while the optical response of the same thickness metal films on ZrO_2 is shown in fig. 5.16(b). In both cases, *i.e.* Ag/dielectric and Au/dielectric, due to the low metal layer thickness (Ag = 9 nm and Au=15 nm), the optical response of the bilayer was dominated by the interference effects of the dielectric layer. A critical thickness of the metal layer has to be reached for unambiguous observation of surface plasmon resonances of the metal deposited on top of the dielectric layer. Therefore, the rest of the study was carried out at higher thickness of the metal films; 18 nm in the case of Ag and 30 nm for Au.

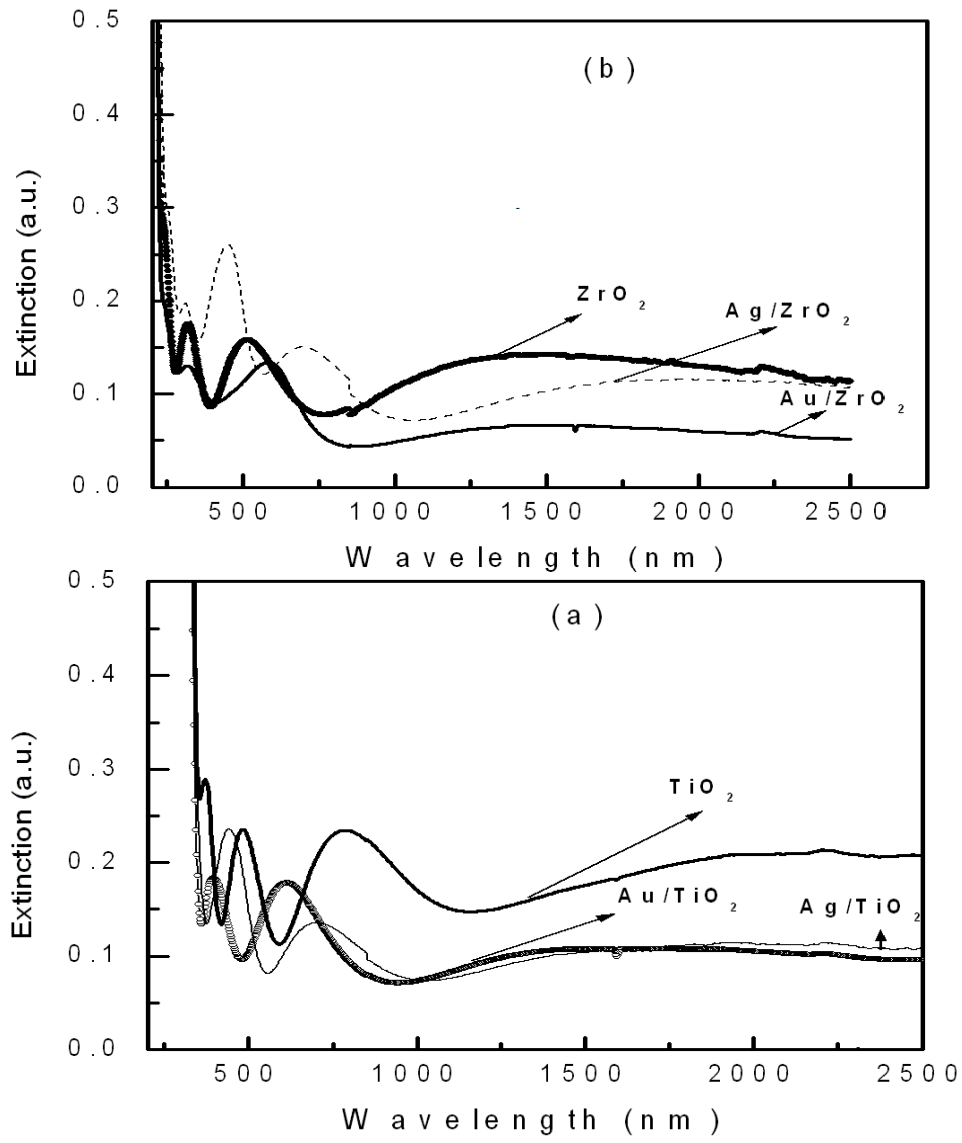

Fig.5.16 (a) The measured extinction spectra of the Ag (9nm)/ TiO_2 and Au (15nm)/TiO_2 bilayers. Also shown is the measured extinction spectrum of the TiO_2 single layer. (b) The measured extinction spectra of the Ag (9nm)/ ZrO_2 and Au (15nm)/ZrO_2 bilayers. Also shown is the measured extinction spectrum of the ZrO_2 single layer.

The measured extinction spectra have been divided into three distinct regions as shown in figs. 5.17 (a) and (b). Region I, which is the window of wavelengths between 200 to 350 nm, contains information about absorption in the proximity of the band gap of the dielectric. Region II extends from 350 to ~800 nm and reveals information about plasmon resonances in the metal films. Region III consists of wavelengths >800nm in the NIR region and contains information about the optical response due to free electrons.

The extinction spectra (in the region from 200 to 2500 nm) of the bilayers consisting of 18 nm thick Ag films deposited on different dielectrics is shown in fig.5.17(a). The corresponding extinction spectra (in the region from 200 to 2500 nm) of the bilayers consisting of 30 nm thick Au films deposited on different dielectrics is shown in fig. 5.17(b).

The optical response of the Ag/dielectric layer in the region I is shown in figs.5.18(a) and (b). It is evident from these figures that there is an increase in optical extinction by almost 7 times, in the region of the band gap of the dielectric, in both cases. There is enhanced light absorption in the region of the band gap due to the presence of the metal layer. Interestingly, the enhancement in absorption is accompanied by a shift in the absorption edge in both cases. Closer examination of this feature reveals that the onset of the (shifted) edge occurs at 310 nm or 3.98 eV. The position of this feature is, however, independent of the dielectric underneath the metal. This suggests that the feature cannot be interpreted as a shift in the absorption edge of the dielectric underlayer. It is known that Ag has a strong interband transition at 3.98 eV [69, 70].

Evidently, this feature can be assigned to the interband transition of Ag which in turn leads to the anomalously large absorption at this wavelength as observed from the spectrum.

The expanded view of plasmon resonance behavior of the Ag films on dielectric layer, corresponding to region II is shown in fig.5.19. It is observed that on both dielectrics, only a single plasmon peak occurs. The wavelengths at which these appear are 424 and 434 nm, for ZrO_2 and TiO_2 respectively. As stated earlier, the refractive index of ZrO_2 and TiO_2 are 1.9 and 2.2 respectively. There is thus a red shift in the plasmon resonance as the dielectric constant of the underlayer increases.

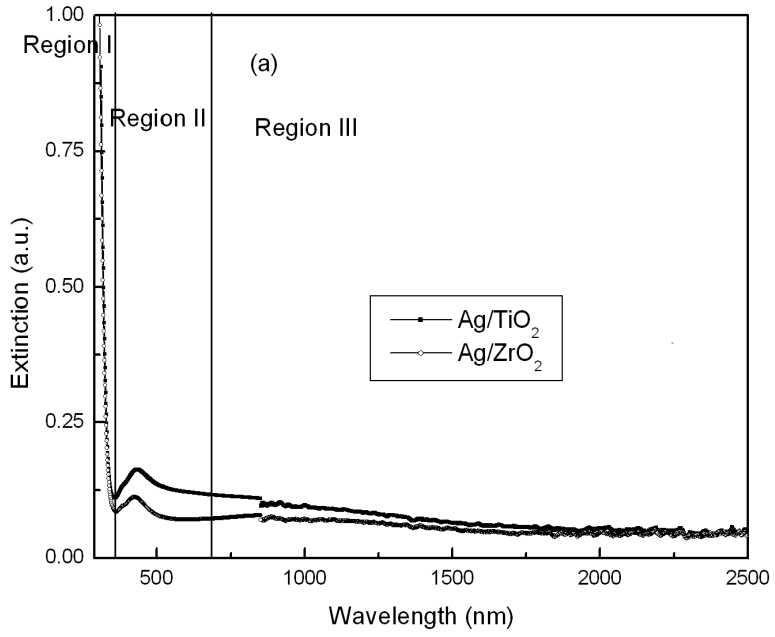

Fig.5.17(a). The measured extinction spectra of the Ag/ dielectric bilayers consisting of 18 nm thick Ag films deposited on TiO_2 and ZrO_2 films.

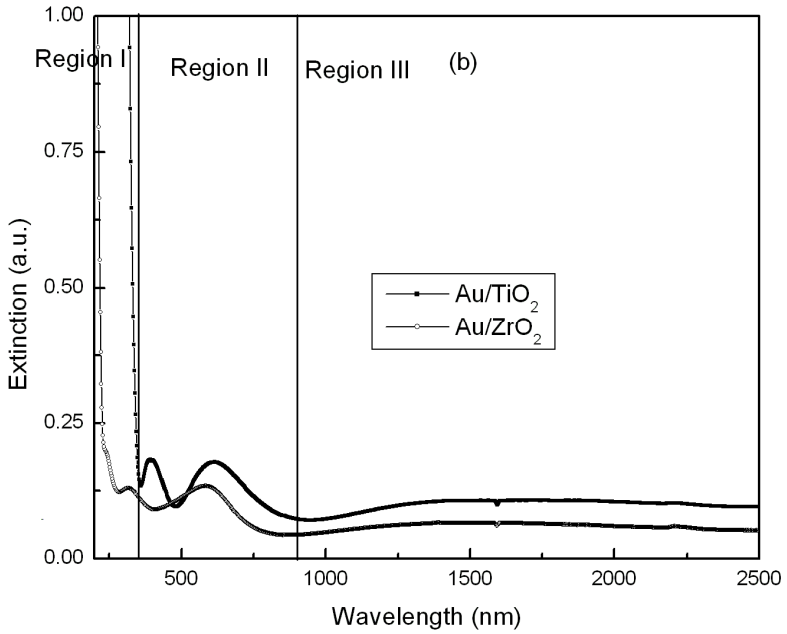

Fig.5.17(b). The measured extinction spectra of the Au/ dielectric bilayers consisting of 30 nm thick Au films deposited on TiO_2 and ZrO_2 films.

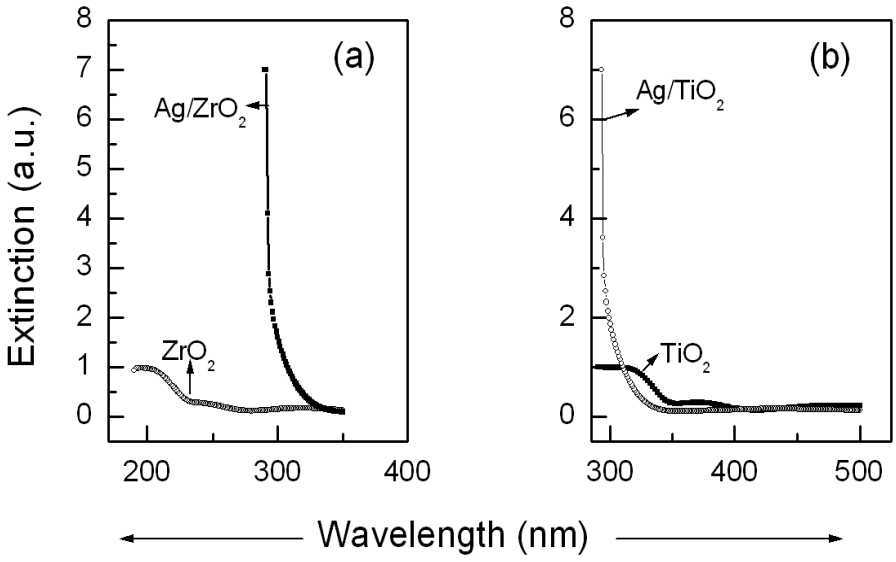

Fig.5.18. The measured extinction spectra in region I for (a) Ag(18nm)/ZrO_2 and (b) Ag(18nm)/TiO_2 bilayers. For comparison the extinction spectra of the single layer ZrO_2 and TiO_2 films in region I are also shown.

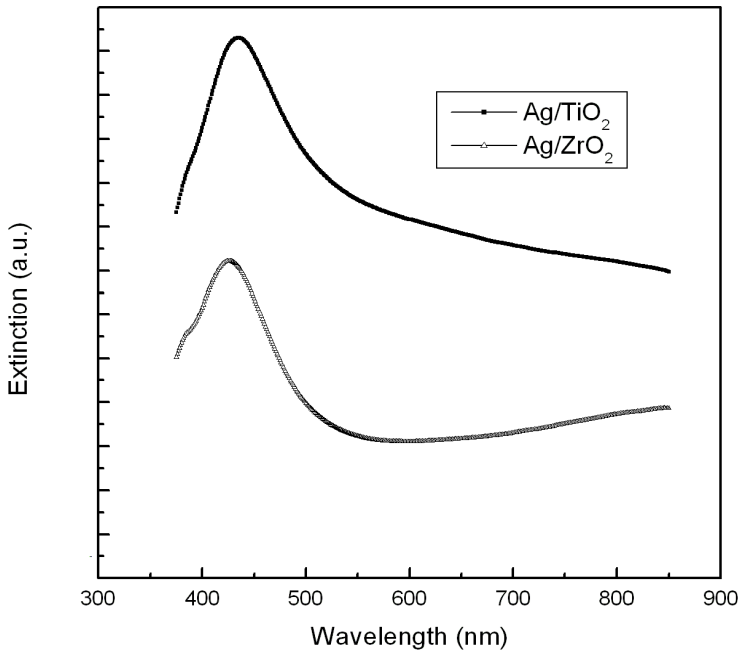

Fig.5.19. The measured extinction spectra in region II for Ag/ZrO_2 and Ag/TiO_2 bilayers.

The region I of the spectrum in the case of Au deposited on ZrO_2 and TiO_2 is shown in figs. 5.20(a) and (b) respectively. The behaviour, in this region is similar to that observed in the case of the Ag/dielectric bilayers.

When the Au layer is deposited on top of the dielectric, a strong absorption edge at a wavelength of 220 nm is observed on both TiO_2 and ZrO_2. As in the case of Ag bilayers it is interpreted as the manifestation of interband transitions in Au [70, 71] and not as a shift in the band gap of the dielectric.

The effect of dielectric underlayers on the plasmon resonance of the Au layers is shown in fig.5.21. Two plasmon resonances are observed for the Au films deposited on to ZrO_2, whereas only a single resonance is observed for the film deposited on TiO_2. For Au films on ZrO_2 these occur at wavelengths of 355 and 630 nm and at 640 nm on TiO_2. The red shift in the main peak around 600 nm can attributed to the increase in the dielectric constant of the underlayer whereas the appearance of the additional peak is due to the variation in microstructure of the Au films on each of these dielectric underlayers.

It can be observed from fig.5.16 (a) and (b) as well as fig.5.17 (a) and (b) that the optical absorption in the IR region (region III) increases with increase in the dielectric constant of the underlayers. In addition, there is a significant change in the IR absorption of the dielectric layers with and without the metal layer on top as shown in fig.5.16 (a) and (b). It is evident that the IR absorption decreases when the metal layer is deposited on top of the dielectric.

The behaviour observed in regions II and III for both sets of bilayers can be examined within the framework of known theories/models. For a spherical metal nanoparticle of diameter $a(<<\lambda)$ embedded in a nonabsorbing surrounding medium of dielectric constant ε_m, the expression for the particle polarizability, α can be written as [2]:

$$\alpha = 4\pi a^3 \frac{\varepsilon - \varepsilon_m}{\varepsilon + 2}_m \qquad (5.4)$$

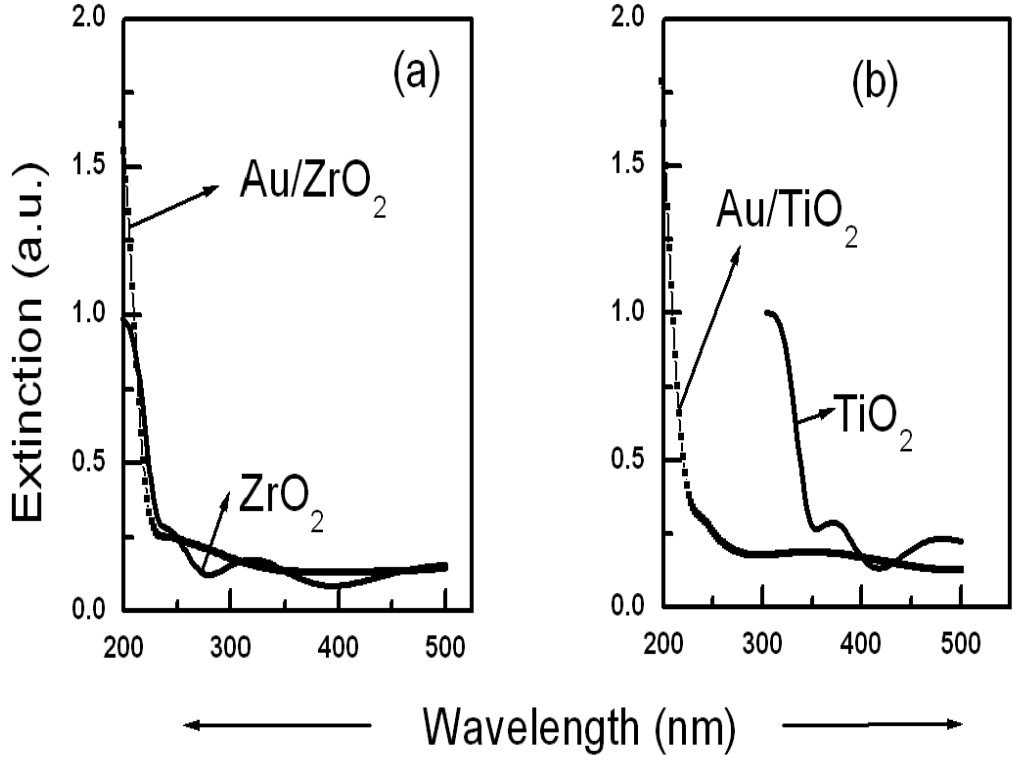

Fig.5.20. The measured extinction spectra in region I for (a) Au(30nm)/ZrO_2 and (b) Au(30nm)/TiO_2 bilayers. For comparison the extinction spectra of the single layer ZrO_2 and TiO_2 films in region I are also shown.

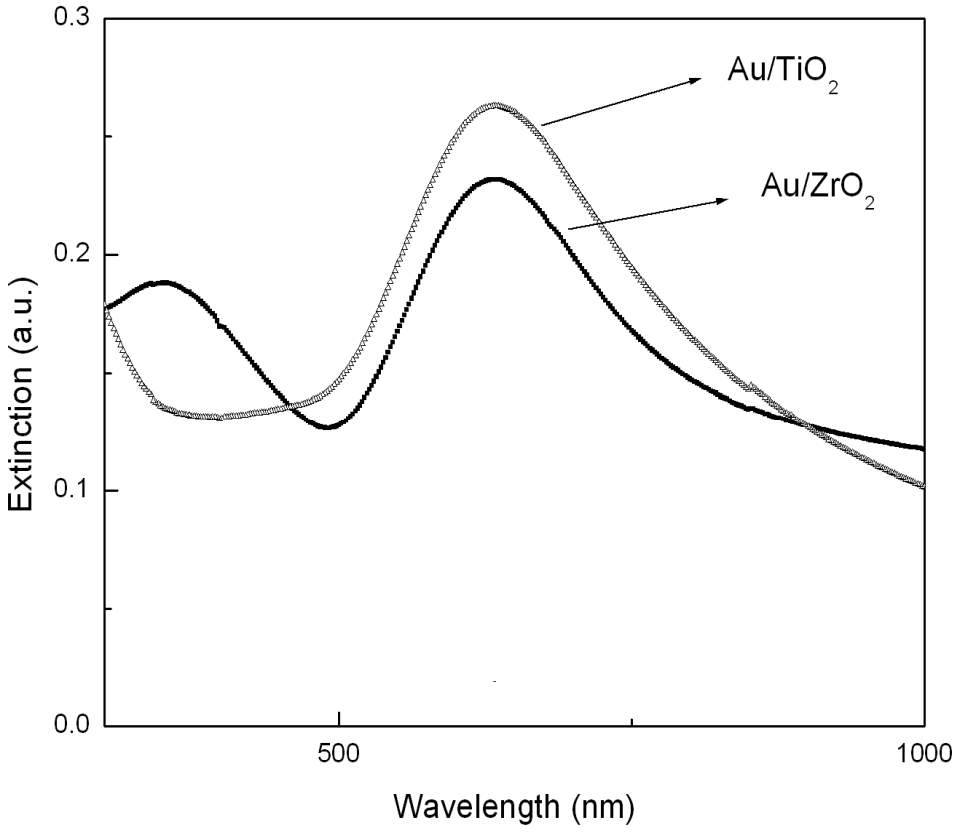

Fig.5.21. The measured extinction spectra in region II for Au/ZrO_2 and Au/TiO_2 bilayers.

with the complex ε=ε(ω) describing the dispersive dielectric response of the metal and a is the particle diameter. From this equation it can be shown that there is a red-shift in the spectral position of the plasmon resonance with increasing dielectric constant of the surrounding host.

This is due to the buildup of polarization charges on the dielectric side of the interface, thus weakening the total restoring force. For ellipsoidal (non-spherical) particles with principal axes *a*, *b*, and *c*, an analogous expression can be found in the quasistatic approximation by introducing geometrical depolarization factors L_i along these axes, leading to.

$$\alpha = 4\pi abc \frac{\varepsilon - \varepsilon_m}{\varepsilon + L_i(\varepsilon - \varepsilon_m)}, \sum L_i = 1 \; for \; i = 1,2,3 \qquad (5.5)$$

For spherical particles, $L_1=L_2=L_3=1/3$. For spheroidal particles, $L_1=L_2$, the plasmon resonance thus splits into a strongly red shifted long-axis mode and a slightly blue shifted short axis mode.

The optical response observed in the current study is consistent with that predicted by the model proposed by Yoshida *et al.* [72].

Hilger *et al.* have studied plasmon resonance behavior of silver nanoparticles on different dielectric surfaces, such as Cr_2O_3, SiO_2 and MgF_2 [36]. They have clearly demonstrated that the effect of contact area of nanoparticles on the plasmon band is to cause a red-shift in the position of the plasmon peak as contact area increases. Similarly, as the dielectric constant of the underlying dielectric surface increases there is a red-shift in the plasmon resonance. Kelly *et al.* [37] have also shown that there is a red-shift in the plasmon resonance peaks of silver as the contact area and refractive index of the host medium increases. It is thus clear that red-shift in the plasmon resonance peaks observed in the current experimental study is consistent with the predictions of theoretical models as well as experimental observations made by other workers.

The Drude model can be used to explain the absorption spectra of the metal films in the near IR region shown in figs 5.15 and 5.16) [40]. The dielectric function at a frequency ω, from this model, is given as

$$\varepsilon(\omega) = \varepsilon_{\infty} - \frac{\omega_p^2}{\omega(\omega + i\omega_{\tau})} \qquad (5.6)$$

Effects from interband transitions on the background polarizability are included in ε_{∞}. The Drude parameters ω_p and ω_{τ} describe the plasma frequency and the relaxation rate of the free charge carriers, respectively. When ω_p is much higher than IR frequencies and $\omega_{\tau} << \omega_p$ then the Drude dielectric function has a strong negative real part in the IR region. This corresponds to a considerably high polarizability. Above the so called plasma edge, the high metallic reflectivity drops down to values that depend on background polarizability and interband transitions. The high reflectivity at lower frequencies is related to the small penetration depth (skin depth) of IR light into the metal. For ω_{τ} in the mid IR (as in the case of defect-rich noble metals) the skin depth is typically 10 to 50 nm for metals (the thickness range of the metal films in the present study). Therefore, metal films of a few nm in thickness are partially transparent in the IR. In the present case the absorption is also affected by the presence of the dielectric layer underneath the metal layer. It is also evident that absorption will be affected by the first term in equation 5.6, which has contributions from the metal as well as the dielectric. The results clearly indicate that the metal/dielectric bilayers have interesting optical behaviour in all three regions of the spectrum studied which can be exploited to many applications.

5.5. Summary

Ag/In bilayer thin films have been deposited on to fused silica substrate by thermal evaporation and its microstructure, structure and optical properties were studied. It is observed that the microstructure evolution follows the structure zone models, exhibiting a largely columnar microstructure with varying degrees of porosity. It is observed that the surface plasmon resonance can be red shifted by employing a combination of thickness

and grain sizes as the control parameters. The splitting was observed in the SPR peak which was explained by a hybridization model.

In the case of Ag/Au (Ag as top layer) and Au/Ag (Au as top layer) bilayer metal thin films deposited by IBSD technique on glass substrate, the morphology of the films are found to be denser and continuous in the case of bilayer films than the single layer. It is observed that the SPR peak shifts towards red and width of the peak also increases with the increase of the top layer of the films. This shift is again explained by the hybridization model in the case of metal/metal bilayer thin films.

The Ag and Au films were IBSD on to the thin films of ZrO_2 and TiO_2 prepared by sol-gel technique. It is observed that the growth of Ag on TiO_2 and ZrO_2 is different than the Au on these dielectrics. It is observed that these bilayers can be used to enhance light absorption in the UV region of the spectrum. The metal/dielectric bilayers exhibit red-shift in surface plasmon resonance peaks with increase in refractive index of the dielectric underlayer. The optical absorption in the near infrared region can also be controlled by varying the refractive index of the dielectric underlayer.

References

1. W. L. Barnes, J. Opt. A: Pure Appl. Opt. **8** (2006) S87-S93.
2. S. A. Maier, H. A. Atwater, J. Appl. Phys., **98** (2005) 011101-1.
3. J. P. Zhao, M. Lu, Z. Y. Chen and J. W. Rabalais, Appl. Phys. Lett., **80** (2002) 3626.
4. M. Salerno, J.R. Krenn, B. Lamprecht, G. Schider, H. Ditlbacher, N. Felidj, A. Leitner, and F.R. Aussenegg, Opto-electronics Review **10** (2002) 217.
5. J. J. Penninkhof, A. Polman, L. A. Sweatlock, S. A. Maier, H. A. Atwater, A. M. Vredenberg and B. J. Kooi, Appl. Phys. Lett., **83** (2003) 4137.
6. G. Xu, M. Tazawa, P. Jin, S. Nakao and K. Yoshimura, Appl. Phys. Lett., **82** (2003) 3811.
7. L. Yin, V. K. Vlasko-Vlasov, A. Rydh, J. Pearson, U. Welp, S.-H. Chang, S. K. Gray, G. C. Schatz, D. B. Brown and C. W. Kimball, Appl. Phys. Lett., **85** (2004) 467.
8. H. Mertens, J. Verhoeven, A. Polman and F. D. Tichelaar, Appl. Phys. Lett., **85** (2004) 1317.
9. T. W. H. Oates and A. Mucklich, Nanotechnology **16** (2005) 2606.
10. F. Le, N. Z. Lwin, J. M. Steele, M. Kall, N. J. Halas and P. Nordlander, Nano. Lett., **5** (2005) 2009.
11. Y. Yang, S. Matsubara, M. Nogami, J. Shi and W. Huang, Nanotechnology **17** (2006) 2821.
12. M. Hirai and A. Kumar, J. Appl. Phys., **100** (2006) 014309-1
13. D. Bharathi Mohan and C. S. Sunandana, J. Appl. Phys., **100** (2006) 064314.
14. S.I. Bozhevolnyi, V.S. Volkov, E. Devaux, J.-Y. Laluet and T.W. Ebbesen, Nature **440** (2006) 508.
15. B. J. Wiley, S. H. Im, Z. Y. Li, J. Mclellan, A. Siekkinen and Y. Xia, J. Phys. Chem. B **110** (2006) 15666.
16. J. Gonzalo, D. Babonneau, C. N. Afonso and J.-P. Barnes, J. Appl. Phys.**96** (2004) 5164.
17. A. Steinbruck, A. Csaki, G. Festag and W. Fritzsche, Plasmonics **1** (2006),79
18. M. Moskovits, I. Srnova-Sloufova, B. Vlckova J. Chem. Phys. **116 (**2002)10435.
19. Y. Huang , Y. Yang, Z. Chen , X. Li, M. Nogami, J. Mater Sci. **43** (2008) 5390.
20. M. K. Nayak and S. K. Ghosh, J. Chem. Phys. **130** (2009) 204702.

21. F. Hubenthal, N. Borg, F. Trager, Appl. Phys. B **93** (2008) 39-45.
22. V. Janicki, J. Sancho-Parramon, F. Peiro, J. Arbiol, Appl. Phys. B **98** (2010) 93-98.
23. V S K Chakravadhanula, M Elbahri, U Schurmann, H Takele, H Greve, V Zaporojtchenko and F Faupel, Nanotechnology **19** (2008) 225302.
24. Z. H. Tang, R. W. Peng, Z. Wang, X.Wu , Y. J. Bao, Q. J. Wang, Z. J. Zhang , W. H. Sun, M.U. Wang, Phys. Rev. B. **76** (2007) 195405.
25. P. Rez, X. Weng, N. J. Long, A. K. Petford-Long, Phys. Rev. B, **42** (1990) 9182.
26. K. H. Su, Q. H. Wei, and X. Zhang, Appl. Phys. Lett. **88** (2006) 063118.
27. D. Duche, P. Torchio, L. Escoubas, F. Monestier, J.-J. Simon, F Flory, G Mathia Solar Energy Materials & Solar Cells, **93** (2009) 1377.
28. L. Armelao, D. Barreca, G. Bottaro, A. Gasparotto, C. Maccato, E Tondello, O. I. Lebedev, S. Turner, G. V. Tendeloo, C. Sada and U. L. Stangar, Chem. Phys. Chem. **10** (2009) 3249.
29. A. Alem and H. Sarpoolaky, Solid State Sciences, **12** (2010) 1469.
30. D. D. Le, T. M. D. Dang, V. T. Chau and M. C. Dang, Adv. Nat. Sci.:Nanosci. Nanotechnol. **1** (2010) 015007.
31. J. M. Jung, M. Wang, E. J. Kim and S. H. Hahn, Vacuum, **82** (2008) 827.
32. R. S. Sonawane and M. K. Dongare, J Mol. Catal A- Chem, **243** (2006) 68.
33. H. M. Gong, S. Xiao, X. R. Su, J. B. Han and Q. Q. Wang, Opt. Exp., **15** (2007)13924.
34. M. Wang and Z. Li, Sensor Actuat. B-Chem, **133** (2008) 607.
35. M. Lomello-Tafin, A. A. Chaou, F. Morfin, V. Caps and J. L. Rousset, Chem. Commun., **3** (2005) 388.
36. A.Hilger, M. Tenfelde and U. Kreibig, Appl. Phys. B **73** (2001)361.
37. L. Kelly, E. Coronado, L. L. Zhao and G. C. Schatz, J. Phys. Chem. B, **107** (2003) 668.
38. A.S. Nair, V. Suryanarayanan, T. Pradeep, J. Thomas, M. Anija and R. Philip, Mater. Sci. Eng. B, **117** (2005)173.
39. Y. B. Zheng, T. J. Huang, A. Y. Desai, S. J. Wang, L. K. Tan, H. Gao and A. C. H. Huan, Appl. Phys. Lett. **90** (2007)183117.
40. D. Dalacu and L. Martinu, J. Opt. Soc. Am. B, **18** (2001)85.
41. Z. Wang, X. Cai, Q. Chen and L. Li, Vacuum **80** (2006) 438.

42. H. Liao, W. Lu, S. Yu, W. Wen and G. K. L. Wong, J. Opt. Soc. Am. B **22** (2005)1923.
43. F. J. Beck, A. Polman and K. R. Catchpole, J. Appl. Phys. **105** (2009)114310.
44. H. A. Atwater and A. Polman, Nat. Mater. **9** (2010) 205.
45. Z. Ouyang, S. Pillai, F. Beck, O. Kunz, S. Varlamov, K. R. Catchpole, P. Campbell and M. A. Green, Appl. Phys. Lett. **96** (2010) 261109.
46. B A Movchan and A V Denchisin, Phys. Met. Metallogr. **28** (1969) 83.
47. J A Thornton, Ann. Rev. Mat. Sci. **7** (1977) 239.
48. R Messier, A P Giri and R A Roy, J. Vac Sci. technol A, **2** (1984) 500.
49. P.B. Barna , M. Adamik, Thin Solid Films, **317**(1998) 27.
50. T. Schuler, T. Krajewski, I. Grobelsek, M.A. Aegerter, Thin Solid Films, **502** (2006) 67.
51. E. Anno and M. Tanimoto, J. Appl. Phys., **98** (2005) 053510.
52. J. Rama and R. Pino, Meliorum Technologies Inc., 620 Park Avenue, Rochester, NY USA 14607.
53. J.R. Sambles, A. P. Hibbins, M. J. Jory and H. Azizbekyan. J. Modern Optics, **47** (2000) 1227.
54. J. C. Lemonnier, G. Jezequel and J. Thomas, J. Phys. C: Solid State Phys., **8** (1975) 2812.
55. R W Cohen, G D Cody, M D Coutts, B Abeles, Phys. Rev B, **8** (1973) 3689.
56. D E Aspnes, E Kinsbron, D D Bacon, Phys. Rev.B, **21** (1980) 3290.
57. P Sheng, Phys. Rev. Lett. **45** (1980) 60.
58. A G Mathewson and H P Myers, J. Phys. C: Solid State Phys., **5**, 1972.
59. K C. See, J B. Spicer, J Brupbacher, D Zhang, and T G. Vargo, J. Phys. Chem. B **109** *(*2005) 2693.
60. E. Prodan, C. Radloff, N. J. Halas, P. Nordlander, Science, **302** (2003) 419.
61. P. K. Jain, and M..A. El-Sayed, Nano Lett., **7** (2007) 2854.
62. E. Prodan and P. Nordlander, J. Chem. Phys., **120** (2004) 5445.
63. R. Brahma and M. G. Krishna, Nucl. Instr. and Meth. In Phys. Res. B **266**, 1493-1497(2008).
64. Hemissi, H. Amardjia-Adnani, Dig. J. Nanomater. Bios. **2** (2007) 299.
65. K. H. Muller, Surface science **184** (1987) 375.
66. K. H. Muller, J. Appl. Phys. **58** (1985) 2573.
67. Jr E. F da Silva, B D Stosic, Semicond.Sci.Tech. **12** (1997)1038.

68. R. Smith, S D Kenny, C F Sanz-Navarro and J. J Belbruno, J. Phys.: Condens. Matter **15** (2003) S3153.
69. N.E.Christensen, Phys. status solidi B **54** (1972) 551.
70. P. B.Johnson and R W Christy, Phys. Rev. B **6** (1972) 4370.
71. M. M. Alvarez, J. T. Khoury, T. G. Schaaff, M. N. Shafigullin, I. Vezmar, and R. L. Whetten, J. Phys. Chem. B **101** (1997) 3706.
72. S. Yoshida, T. Yamaguchi, and A. Kinbara, J. Opt. Soc. Am. **61** (1971) 463.

Chapter VI: Overview of the present work and Future prospects

Chapter VI: Overview of the present work and future prospects

6.1. Summary

The work presented in this thesis is mainly focused on the study of structure, microstructure and optical properties of Ag and Au metal thin films. One of the main objectives of the work was to deposit very thin self assembled nanostructured films by ion beam sputter deposition (IBSD) technique at very low ion energy. The summary is categorized in two sections,(1) microstructure and structure and (2) optical response of single and bilayer metal thin films.

6.1.1. Microstructure and structure

In summary it has been shown that the IBSD technique offers very fine control over growth of the films compared to DC sputtering and thermal evaporation techniques. It is observed that IBSD offers a great degree of control over the size, shape and interparticle spacing in the nanostructures and nanostructured films. Growth is found to be discontinuous at low ion energy and the process of growth mechanism is very well explained by the theory of growth of thin films. Varieties of nanostructures such as non-regular arrays of nanoparticles, nanoneedles and nanoclusters have been realized. In the growth process, two different coalescence regimes are observed depending on the substrate roughness. Normal coalescence, defined as the regime where grain coarsening as a function of increasing deposition duration and temperature is observed on smooth BSG substrates. Abnormal coalescence defined as the regime where the cluster sizes decrease as a function of increasing deposition duration and temperature is observed on rough CCG substrates. It is observed that gold films are less discontinuous than the silver films with lower island density. At room temperature, the Ag nanoparticles are nearly spherical in shape with interparticle separation that is larger than the particle diameter. The Au particles cluster together to form the boot-shaped aggregates. The number density of these aggregates is small and the separation is smaller than their size on average. As substrate temperature increases, the size of particles, in Ag and that of aggregates in Au decreases. It appears that the number density decreases in Ag but remains constant in the case of Au. Both films show polycrystalline nature.

6.1.2. Optical response

The surface plasmon resonance (SPR) peak of single layer Ag and Au films are found to be red shift with the increase of ion energy and the duration of deposition time which causes in increase in thickness and grain size. Thus the shift here is due to the increase in the thickness of film and grain size. In the case of Ag and Au thin films deposited at different temperatures, the surface plasmon resonance peak shifts towards blue with the increase of the deposition temperature which is due to the decrease in the particle size with the increase in deposition temperature. In the case of Au films deposited at 300^0C for different durations, the surface plasmon resonance peak shifts towards red with the increase of the deposition time and this is attributed to the increase in film thickness.

In the case of metal-metal bilayer for Ag/Au (Ag as top layer) and Au/Ag (Au as top layer) thin films, it is observed from AFM images that the films become denser in the case of Ag/Au and Au/Ag bilayer than the single layer of Ag and Au. Their optical response shows that the surface plasmon resonance peak shifts towards red in both the bilayer case and this shift is very well explained by a model called the plasmon hybridization model.

In the case of Ag/In bilayer thin films, microstructure showed a large grain size with the columnar growth in single layer films and in bilayer, microstructure showed aggregation and forming large grains. It is observed in single layer In films that the SPR shifts towards red with splitting with the increase of the In thickness and in the case of bilayer Ag/In thin films, initially the SPR shifts towards blue and splitting with the increase of In thickness and at higher In thickness, SPR shifts towards red vanishing the splitting. The observed behavior of SPR is also very well explained by plasmon hybridization model.

In the case of Ag/TiO_2, ZrO_2 and Au/TiO_2, ZrO_2 bilayer thin films, it is observed from the AFM image that the dielectric layer films are densely packed. Morphology of Bilayer Ag/TiO_2 thin films were found to be discontinuous where as Ag/ZrO_2 thin films was continuous and dense. The opposite is observed in the Au/dielectric bilayer case. This is due to the difference in wettability of Ag and Au to the different dielectric materials. In optical response it is observed that there is enhanced light absorption in UV region in the

bilayer films. Metal/dielectric bilayer exhibits red shift in SPR peaks with increase in refractive index of dielectric underlayer and it is found that the optical absorption in the NIR region can also be controlled by controlling the refractive index of the dielectric layer.

The current work demonstrates the feasibility of ultra-low energy ion beam sputter deposition as a technique for the deposition of discontninuous metal thin films with controllable shape, size and separation of particles leading to tunable optical response in the UV-Visible-NIR region of the electromagnetic spectrum.

6.2. Future prospects

Ion beam sputter deposition offers a very fine control over the growth of thin films as observed from the recent experiments. We have achieved nanostructured metal thin films by depositing at low ion energy. The future prospects include deposition of ordered or patterned nanostructure thin films by controlling various parameters of IBSD system.

Random nanostructure is characterized by a wide distribution in sizes and shapes of metallic clusters and they exhibit a broad plasmon resonance that can cover from visible to infrared spectra. Local field enhancement for this kind of structure exists over this entire spectrum and the magnitude of this enhancement is difficult to predict. Therefore, the near field optical properties and to map the local field enhancement of these nanostructures by scanning nearfield optical microscope (SNOM) would be very interesting.

Another area could be to use these materials in the study of non linear optical properties because Ag and Au embedded in different dielectric shows interesting non linear optical properties. It is known that surface plasmon resonance is very sensitive to its shape, size and the environment in surroundings and iodization of ultra thin metal films causes a controlled depletion of electron density leading to a gradual disappearance of plasmons. This could be interesting to study the optical properties by iodizing these metal films.

Another area that is of extreme importance in nanophotonics is the area of sensors and waveguides. Such applications can also be explored in the future.